Ph.D. Dissertation

Investigation on Self-assembled Ordered Structures in Liquid Crystalline Systems

Raman Research Institute

RRI
Bengaluru
560080,
India

Thesis submitted for the degree of

DOCTOR OF PHILOSOPHY

Jawaharlal Nehru University

JNU
New Delhi
110067,
India

Dipak Patra

Soft Condensed Matter Group

RRI

March 2024

Certificate

This is to certify that the thesis entitled **"Investigation on Self-assembled Ordered Structures in Liquid Crystalline Systems"** submitted by **Dipak Patra** for the award of the degree of Doctor of Philosophy of Jawaharlal Nehru University is his original work. This has not been published or submitted to any other University for any other Degree or Diploma.

Signature of Supervisor
Prof. Arun Roy
Professor
Soft Condensed Matter Group
Raman Research Institute (RRI)
Bengaluru 560080, Karnataka, India

Signature of Director/ Chairperson
Prof. Biman B. Nath
Director (i/c) & Professor
Astronomy & Astrophysics Group
Raman Research Institute (RRI)
Bengaluru 560080, Karnataka, India

Date:
Place:

Declaration

I, **Dipak Patra**, declare that the work reported in this thesis entitled **“Investigation on Self-assembled Ordered Structures in Liquid Crystalline Systems”**, is entirely original. This thesis is composed independently by me at **Raman Research Institute (RRI)** under the supervision of **Prof. Arun Roy** and is the result of my own work unless otherwise stated appropriately in the text. I further declare that the subject matter presented in this thesis has not previously formed the basis for the award of any degree, diploma, membership, associateship, fellowship, or any other similar title of any university or institution. I have also run this thesis through the plagiarism detection software DrillBit.

Signature of Supervisor
Prof. Arun Roy
Professor, RRI

Signature of Candidate
Dipak Patra
Research Fellow, RRI

Soft Condensed Matter Group
Raman Research Institute (RRI)
Bengaluru 560080, Karnataka, India

Date:
Place:

Acknowledgement

First and foremost, I want to express my gratitude to my Ph.D. supervisor, Prof. Arun Roy, for his guidance and critical assessment of the research works. The freedom given by him has helped me to pursue my dream of being an independent researcher.

I am grateful to have Prof. V. A. Raghunathan and Assoc. Prof. Sayantan Majumdar as my advisory committee member, and thank them for giving invaluable comments and suggestions during the annual assessment. I want to thank Assoc. Prof. Gautam Vivek Soni, Prof. Pramod A Pullarkat, Prof. Yashodan Hatwalne, and Prof. Ranjini Bandyopadhyay, for taking the coursework classes and introducing the wonders of soft matter systems.

I want to thank SCM group secretaries Radhakrishna and Chaitanya, members of my supervisor's family, and other SCM members for their help and support. I would like to thank my experimental lab mates, Deepshika and Subhadip da, for sharing the experimental data to verify the theoretical predictions. My thank goes to other departments in RRI, such as Administration, Library (especially Manjunath Kaddipujar), Canteen, Health Clinic, Hostel, Security, IT & computing, for their timely response and support.

I would like to thank online websites such as arXiv, ResearchGate, YouTube, Coursera, edX, Overleaf, etc., for providing the study materials free of cost. I am also thankful to the open-source software providers and code developers such as Python, LaTeX, blender, and GitHub. It would have been impossible to complete this thesis without these free resources.

I am extremely thankful to the International Center for Theoretical Sciences (ICTS -Bangalore) for providing free bus service and allowing me to attend any lecture without prior registration. I often visited the campus in the earlier days of my Ph.D. and enjoyed the food, science lecture, cycling, and sports. Interestingly, the research problem discussed in Chapter Six of the thesis is an outcome of a discussion meeting. I would like to thank the Indian Institute of Science for allowing me to attend seminars.

I would like to thank my university and college professors, Prof. Nikhilesh Kar, Prof. Somendra M. Bhattacharjee, Asst. Prof. Bobby Ezhuthachan, Prof. Parthasarathi Majumdar, and Assoc. Prof. Makhanlal Nanda Goswami for motivating me to pursue a research career. I would like to thank my teachers, Sukdeb Samanta (chemistry teacher), Sudarsan Das, Jibankrishna Patra, Swapan Maity, and Bijay Krishna Pan, for their support and financial help during my school days.

I am incredibly indebted to some of my friends, Subhajit da, Saikat, Bapan, Subhadip da, Sagar da, Ashish, Swarnak, and Vishnu, because of their assistance during medical emergencies. I enjoyed the Sunday cooking and occasional party with Maheswar da, Swarnak, Koushik da, Tanuman, Avik, Anindya da, Pradosh, Rajkumar da, Sovan, Sachidananda, Rishav, Soumen, Sayantan, Baxi, Agniva, and Sushovan. I am highly thankful to them for their support. I thank Vani, Alaka, Ion, Anirban da, Animesh da, Saichand, Irla, Deepsikha, Chandeswar, Arsalan, Rajkumar, Sandeep, Arkabrata, Vaibhav, Abhisekh, Punit, Raghuveer, Abhisekh Sadhu and Sukh Veer for the discussion. Before joining RRI, I never used to play any kind of outdoor games. Having said that, I started to play badminton and football after the first year of my Ph.D. Now, I have gained some skills in these sports. The active involvement in these sports has helped me to focus on research work and boost my self-control to the ups and downs in this life. The sports world could have been unknown to me if I had not met these people: Jagadeesh, Chandan, Subodh, Sharath, Yatheendran, Jayakumar, Arun, Vardhan, Arjun, Nishant, and Naren da. My thank goes to all of them.

I thank my school-college-university friends Samir, Jhantu, Subham, Koushik, Sibaram, Saikat, Pandey, Anup, Satyaki, Somnath, Sasmal, Arijit, Ananda, Inuddin, Sumon, Aritra, Sourav, Sreetama, Arkajyoti, and Priyabrata for their help and support in need.

I am extremely grateful to my family members and relatives: father, mother, grandmother, maternal uncle's house, elder sister, and brother-in-law for their constant support. Without their love and support, I would not be able to complete my thesis.

Synopsis

Liquid crystalline materials are known to exhibit orientational order in their fluid phases due to the anisotropy of the constituent molecules. These ordered fluid phases are the intermediate states between the crystal phase with both translational and orientational order in three dimensions and the completely disordered isotropic liquid phase. Hence, these liquid crystalline phases are also known as mesophases. These mesophases are characterized by a long-range orientational order with partial or no translational order. Hence, these phases have the property of flow like a fluid and anisotropic properties of a crystal. These exotic orders in the mesophases lead to the manifestation of a rich variety of self-assembled structures. The various types of phases and transitions among them can be obtained by the application of external stimuli such as temperature and electric field. The properties of these phases can also be easily tuned by these external impetuses. The effect of external fields on the properties of these phases has been employed in various technological applications such as displays, sensors, lenses, phase modulators, etc. In addition to these technological applications, the liquid crystal system is a fertile area of research for fundamental studies on the nature of order-disorder transitions, symmetry-breaking phenomena, electro-optical effects, elastic instabilities, dynamics and nature of topological defects, etc. Furthermore, the knowledge of liquid crystalline systems can be utilized to understand other systems such as polymers, colloids, biological systems, and granular media wherein the orientational order can be observed.

This thesis deals with the self-assembled ordered structures in liquid crystalline systems exploring the molecular organisation, phase transitions, and instability-induced pattern formation. In this thesis, four different problems are investigated using theoretical and computational tools such as phenomenological theory, Monte Carlo simulations, and other numerical methods. The thesis is divided into seven chapters which are summarized as follows.

Chapter 1

In this chapter, we give a brief introduction to the various liquid crystalline systems and their phases. We also discuss the earlier theoretical studies of these systems which are relevant to the research works carried out in this thesis.

Chapter 2

This chapter deals with the self-assembled structures of symmetric Bent-Core (BC) molecules. The symmetric bent-core molecules are achiral in nature and have C_{2v} point symmetry. These achiral bent-core molecules are known to exhibit spontaneous chiral symmetry breaking in their tilted polar smectic phases. A large number of studies involving experiments, phenomenological theories, mean-field theories, and Monte Carlo and molecular dynamics simulations have been carried out in the past to understand the phase behavior of these systems. In spite of these studies, the underlying mechanism of chiral symmetry breaking is not fully understood. This type of chiral symmetry breaking has also been observed in some colloidal bent-core particles. These observations in both molecular and colloidal systems imply that the geometry or shape of the constituent particles plays an important role in this symmetry-breaking phenomenon. The geometrical effect of shape can be included in the system by incorporating the excluded volume interaction between two bent-core molecules.

However, the analytical calculation of the excluded volume is a formidable task for these BC molecules. It is known that the exact expression for the excluded volume between two straight rod-like molecules can not be found analytically. We have, therefore, numerically computed the excluded volume between two BC molecules in a layer assuming perfect orientational order. In these computations, we have utilized two types of models for BC molecules, namely the hard sphero-cylinder model (HSC) and the bead model. In the HSC model, the BC molecule consists of two rigid sphero-cylindrical arms connected end to end at an angle which is termed as the bending angle. In the bead model, hard spherical beads are joined together to form the BC molecule. We have computed the excluded volume for various values of the bending angle and tilt angle of the molecules with respect to the layer normal. The configuration with minimum excluded volume is an entropically favorable state. We show from these computations that the minimum excluded volume between the molecules in the tilted polar smectic layer corresponds to a chiral layer structure. Thus, the excluded volume effect accounts for the spontaneous chiral symmetry breaking observed in the tilted polar smectic phases. For the HSC model, we find that the tilted polar smectic phase with only C_2 symmetry of the layer is always favorable irrespective of the values of the bending and tilt angles. On the other hand, the bead model of the BC molecules predicts the existence of C_s, C_1, and C_2 symmetric layers depending on the values of the bending and tilt angles. We have constructed a phase diagram in the bending and tilt angles plane showing the stability regions of these different symmetries of layers.

The excluded volume computations give results corresponding to athermal systems. To account for the thermal and electric field-driven phase transition, we have also carried out Monte Carlo (MC) simulations using a coupled XY-Ising model. Therefore, based on the excluded volume results, we have constructed a coupled XY-

Ising model to describe the phase transitions of a system. In this model, we assume that the BC molecules in a layer are tilted with respect to the layer normal with a fixed tilt angle but with variable tilt directions. The tilt direction of the BC molecules in a layer plane can be described by an XY spin. In addition, depending on the orientation of the bending direction of a BC molecule in a layer, there can be a left or right-handed configuration which can be described by an Ising variable. Therefore, the Ising variable represents the chiral configuration of an achiral BC molecule with respect to the layer. We have carried out Monte Carlo simulations on a square lattice with periodic boundary conditions. The model predicts different types of phase sequences depending on the interaction parameter and also accounts for electric field-induced chiral symmetry breaking. The electric field-induced breaking of chiral symmetry in bent-core liquid crystals has been reported experimentally.

Chapter 3

In the orthogonal smectic A (SmA) phase, the long axes of the molecules are, on average, parallel to the layer normal, whereas in the smectic C (SmC) phase, the average orientation of the long axes is tilted with respect to the layer normal. Therefore, a significant decrease in layer spacing is usually observed across the SmA to SmC phase transition on cooling. However, some compounds known as de Vries materials have been found in which the layer spacing does not change significantly across the SmA to SmC transition. Two types of model have been proposed for the smectic A phase known as the de Vries SmA (dSmA) phase to account for the minimal layer contraction across this dSmA to SmC transition. In the first model, known as the non-correlated layer model, all the molecules in a layer are, on average, tilted with respect to the layer normal along a preferred direction. But, the tilt directions in each layer are randomly correlated due to the weak inter-layer interactions giving rise to the uniaxial dSmA phase about the layer normal. In the second model, known as the diffusive cone model, molecules in a layer are, on average, tilted with a fixed tilt angle but with random tilt directions. Therefore, the molecular long axes are uniformly distributed over the surface of a cone, and the average orientation of molecular long axes is parallel to the layer normal. This organization of the molecules gives rise to the uniaxial dSmA phase. In both models, as the molecules are already tilted with respect to the layer normal in the dSmA phase, the layer spacing is significantly lower than the molecular length. However, the tilt directions of the already tilted molecules get correlated across the dSmA to SmC transition with no significant layer contraction.

These de Vries materials generally exhibit the following phase sequence on cooling: isotropic→ dSmA → SmC phases. To the best of our knowledge, there is no report of a compound exhibiting the SmA → dSmA transition. We have recently found that a compound consisting of bent-core hockey-stick-shaped molecules exhibits the isotropic → SmA → dSmA → SmC → crystal phase sequence on cooling. We have developed a phenomenological Landau theory to account for the SmA → dSmA → SmC phase transitions observed in our sample. As both the orthogonal SmA and dSmA phases have the same uniaxial $D_{\infty h}$ point symmetry, a first-order phase transition between them is expected which is observed experimentally. We have computed the layer spacing as a function of temperature which agrees very well with the experimental findings. We have also constructed a theoretical phase diagram depending on the model parameters to indicate the stability regions of these phases.

Chapter 4

It has recently been observed in our group that a liquid crystal compound exhibits banded spherulitic growth of its solid phase from its smectic A phase on cooling.

We have constructed a phase-field model with a conserved order parameter and a non-conserved order parameter to account for this banded spherulitic growth. We show that the growth dynamics of this system can be described by the equations of a time-dependent Ginzberg-Landau (TDGL) model of type C. In this chapter, we present the detailed formalism of this model and investigate various patterns that form during spherulitic growth depending on the model parameters.

The linear stability analysis (LSA) of the model was performed to predict the instability threshold as a function of model parameters. We find that modes with a range of wave vectors become unstable above a threshold control parameter. The wave vector corresponding to the fastest-growing mode is generally the most dominant mode and it gives rise to the periodicity of the instability-induced patterns. We have also carried out numerical studies on the full nonlinear equations of the model to investigate the pattern formations and their growth dynamics. The numerical studies reveal the existence of rich varieties of patterns such as ring banded (target), broken ring, and continuous circular patterns. We have constructed a phase diagram depending on the model parameters to indicate the stability regions of these patterns. It is found that the patterns mostly grow as a circular domain with the rhythmic or non-rhythmic growth of its radius. In the rhythmic growth, the radius of the pattern increases in a step-like fashion with time, giving rise to the non-uniform growth dynamics. Though the growth of radius is nonlinear at each individual step, it shows, on average, a linear growth law with time. On the other hand, for the non-rhythmic growth, the radius of the pattern increases linearly with time in a smooth manner. In both cases, the radius of the pattern generally increases on average linearly with time.

Chapter 5

The spherulitic growth of solids is a ubiquitous phenomenon exhibited by many different types of materials, such as polymers, minerals, bio-materials, metals, and salts. In spherulitic growth, the solid phase after nucleation grows with a spherical growth front with continuous orientational symmetry in contrast to the growth of a crystal having discrete orientational symmetries. In spite of research on it for over a century, the detailed understanding of the mechanism of this abundantly found natural growth phenomenon is still lacking. It is found that this spherulitic growth morphology is often associated with the formation of many radially aligned fibrillar crystallites, which branch non-crystallographically to fill space during the growth. In addition to this continuous spherulitic growth, a kind of spherulite known as banded spherulite has also been observed. A banded spherulite is accompanied by a spherically symmetric growth front and periodic radial variation of birefringence. This variation of birefringence in quasi-two-dimensional geometry produces concentric interference color bands when viewed through crossed polarizers. In most materials, these banded spherulites are found to be formed by radially oriented periodically twisted fibrillar crystallites. The twisting can occur in a system due to multiple causes such as surface stress mismatch, iso-chiral screw dislocation, auto deformation, and topological defects. The organized twisting of the fibrillar crystallites is considered to be a primary mechanism for the formation of the banded spherulites. Here, we have studied the banded spherulitic growth of a liquid crystalline compound (8OCB) during its crystallization from the smectic phase. The detailed experimental studies reveal that the solid state of this material exhibits the coexistence of fibrillar crystallites embedded in an amorphous state. The banded spherulites in this compound are formed with a periodic variation of the composition of untwisted radially aligned fibrillar crystallites and an amorphous solid state, in contrast to the organised twisting of the fibrillar crystallites proposed earlier.

In this chapter, we used the model described in Chapter 4 to account for the spherulitic growth observed in the compound 8OCB. Armed with our experimental results, we have proposed a conserved and a non-conserved order parameters for describing the transition to the banded spherulitic state from the smectic phase of this compound. The conserved order parameter describes the local deviation of the molecular density in the banded spherulite from the average density of the smectic phase. Whereas the non-conserved order parameter describes the local composition of the molecules in the nanocrystalline and amorphous solid states of the banded spherulite. The control parameter in the model is found to be the supercooling of the system from its smectic phase. The linear stability analysis (LSA) of the model was performed to predict the instability threshold as a function of the control parameter. We find that modes with a range of wave vectors become unstable above the threshold. The wave vector of the fastest-growing mode gives the periodicity of the banded spherulite. We have compared the periodicity obtained from the LSA with the experimentally measured band spacing of the banded spherulite for different values of supercooling. The good agreement between the theoretical results and experimental data confirms the general validity of this model. We have performed numerical studies of the full nonlinear equations to investigate the growth dynamics of the banded spherulite. The simulation results on this system show ring-banded pattern formation with rhythmic growth. The computed band spacing obtained from simulations as a function of supercooling also agrees very well with the experimental findings. Interestingly, it is experimentally observed that the band spacing diverges at a particular supercooling on approaching this value from below. This divergence of band spacing has also been reported for some other materials. However, to the best of our knowledge, there is no report explaining this observation. Our model, for the first time, accounts for this observation in both the LSA and simulations.

Chapter 6

Wrinkling instability can occur in various systems such as our brains, dry fruit skins, animal skins, flowers, the crust of the earth, etc. To get better insights into the underlying mechanisms leading to this instability, an uniaxially compressed floating thin sheet atop a substrate is often considered as a good model system. In this type of model systems, the wrinkling wavelength is determined by the properties of the substrate and the thin sheet. For example, the wavelength λ corresponding to a thin sheet on an isotropic fluid substrate can obtained by a scaling relation $\lambda \sim (B/\rho g)^{1/4}$ where B, ρ, and g are bending modulus of the thin sheet, density of the isotropic liquid and the acceleration due to gravity, respectively. In this case, λ depends on a few material parameters which limits the tunability of the wavelength using external stimuli such as electric field, temperature, and other substrate properties. The wrinkling instability can be easily tuned using these external drives by adopting an anisotropic medium as the substrate. We have theoretically studied the wrinkling instability of a thin sheet floating on a nematic medium when the sheet is subjected to an in-plane uniaxial compression. This chapter describes the detailed theoretical model and the results obtained in this study. In the model, we have considered three essential free energies associated with the system, namely the bending energy of the thin sheet and the gravitational and distortion energies of the nematic fluid. Following a similar procedure which has been used in earlier studies dealing with a thin sheet floating on an isotropic fluid substrate, we minimize the total free energy of the system by assuming a sinusoidal undulation of the compressed thin sheet. The wavelength of the periodic undulation of the thin sheet corresponding to the minimum energy gives the equilibrium value of the wave vector of the wrinkling pattern. We have studied the variation of the wave vector of the wrinkling pattern as a function of various model parameters. The periodicity of the pattern is always found to be larger in the case of nematic substrate compared to its isotropic state. This arises due to the excess energy cost associated with the distortion of the nematic substrate. The periodicity of the pattern sensitively depends on the curvature elastic constants and the surface anchoring conditions of the nematic. Interestingly, it is also found that the wrinkling periodicity depends on the amount of compression for the hybrid anchoring condition of the nematic director on the bounding surfaces.

Chapter 7

This chapter contains the summary of the research works described in this thesis and also possible directions for future research.

Publications

- Dipak Patra, and Arun Roy,
  Spontaneous breaking of chiral symmetry in achiral bent-core liquid crystals: Excluded volume effect,
  PHYSICAL REVIEW E 107, 034704 (2023). (**PDF**)
- Subhadip Ghosh, Dipak Patra, and Arun Roy,
  Observation of banded spherulite in a pure compound by rhythmic growth,
  PHYSICAL REVIEW MATERIALS 6, 053401 (2022). (**PDF**)
- Deepshika Malkar, Dipak Patra, and Arun Roy,
  SmA–de Vries SmA–SmC phase sequence exhibited by bent-core hockey stick-shaped molecules. (in preparation)
- Dipak Patra, and Arun Roy,
  Pattern formation and growth dynamics in a phase-field model. (in preparation)
- Dipak Patra, and Arun Roy,
  Wrinkling of a thin sheet on a nematic substrate. (in preparation)

Contents

---

1 Introduction 1

1.1 Liquid crystalline phases 2

1.1.1 Nematic phase 3

1.1.2 Smectic phases 10

1.1.3 Polar smectic phases 12

1.2 Growth of solid Phases 13

1.2.1 Spherulites 13

2 Spontaneous breaking of chiral symmetry in achiral bent-core liquid crystals: Excluded volume effect 19

2.1 Introduction 20

2.2 Model 24

2.3 Results and Discussions 29

2.4 Monte Carlo Simulation 35

2.5 Summary 41

3 A phenomenological theory for the SmA – de Vries SmA – SmC phase transition 47

3.1 Introduction 48

3.1.1 Theoretical Model 51

    - 3.1.2 Results And Discussions 57
  - 3.2 Summary 61

4 Pattern formation and growth dynamics in a phase-field model 65

  - 4.1 Introduction 66
  - 4.2 Theoretical Model 69
  - 4.3 Linear stability analysis 72
  - 4.4 Numerical Studies 80
  - 4.5 Summary 88

5 Formation of banded spherulite by rhythmic growth 95

  - 5.1 Introduction 95
  - 5.2 Model 100
  - 5.3 Results and discussions 103
  - 5.4 Summary 107

6 Wrinkling of a thin sheet on a nematic substrate 113

  - 6.1 Introduction 114
  - 6.2 Free energy of the system 116
    - 6.2.1 Bending energy of the thin sheet 116
    - 6.2.2 Gravitational energy associated with the height modulation . 118
    - 6.2.3 LC energy 119
    - 6.2.4 Total Energy 124
  - 6.3 Energy minimization 124
  - 6.4 Results and Discussions 126
  - 6.5 Summary 130

7 Conclusions and future research directions 135

List of Figures

1.1 Schematic representation of the crystal, isotropic, and intermediate phases of a liquid crystalline system constituting rodlike particles. . . 1

1.2 Schematic representation of different shaped liquid crystalline molecules from left rodlike (8OCB), discotic (Benzene haxa alkanoates), Bent-core, and Hockey stick molecules. 3

1.3 Schematic representation of molecular arrangement in the uniaxial nematic phase. The nematic director $\hat{n}$ and the long axis of a molecule $\hat{a}$ are denoted by the double-headed red and black arrows, respectively. 4

1.4 (a) The variation of the free energy density as a function of the order parameter for different values of a. (b) The variation of the order parameter S as a function of temperature. Where the other constants are $a' = 0.1, b = -0.6$ and $c = 0.65$. 8

1.5 Schematic representation of the three elastic deformation modes of the nematic director field: (a) splay, (b) twist, and (c) bend deformation modes. 9

1.6 Schematic representation of the molecular arrangement in the (a) smectic A and (b) smectic C phases. 10

1.7 Schematic representation of the molecular arrangement in perfectly ordered (a) polar smectic A (SmAP) and (b) tilted polar smectic (SmCP) layers of bent-core molecules. The long axis and the polar direction of a bent-core molecule are denoted by the unit vectors $\hat{l}$ and $\hat{p}$, respectively. 11

1.8 Schematic representation of a spherulite domain. (a) The domain is formed by multiple fibrils emanating from a single nucleation site. (b) The domain starts to grow from a bunch of fibrils and continues to grow due to non-crystallographic branching. At a long time, the domain attains a spherical growth front, giving rise to the "sheaf of wheat" structure. 14

1.9 The polarised optical microscope (POM) images of a spherulite of 8OCB (a) between crossed polarisers and (b) with a λ-plate inserted in the optical path in addition to the crossed polarisers. The direction of the major refractive index in the sample plane is denoted by white double-headed arrows around the seed. (c) The scanning electron microscopic image of a spherulitic region showing the presence of fibrils. (d) The zoomed view of the indicated box in (c). 15

2.1 Schematic representation of the orientation of a BC molecule in a perfectly ordered tilted polar smectic layer where θ, ϕ and ψ are the Euler angles. The layer normal $\hat{k}$ is parallel to the z-axis and the XY plane is the layer plane. The double-headed arrow represents the projection of the long axis on the layer plane. For a perfectly ordered layer, the director $\hat{n}$ and polar order $\vec{P}$ are parallel to $\hat{l}$ and $\hat{p}$ of the molecules respectively. The unit vector $\hat{\xi} = (\hat{k}\cdot\hat{l})(\hat{k}\times\hat{l})/|(\hat{k}\cdot\hat{l})(\hat{k}\times\hat{l})|$ represents the tilt direction of a molecule which is perpendicular to the ($\hat{l}$,$\hat{k}$) plane. 21

2.2 The model structures (a) bead model (b) hard sphero-cylinder (HSC) model of a BC molecule used in the computation of excluded volume. The unit vectors $\hat{l}, \hat{p}$ and $\hat{m}$ are body fixed axes. The unit vectors $\hat{u}$ and $\hat{d}$ represent the orientation of upper and lower arms respectively. 25

2.3 The variation of the excluded volume V_{ex} with the relative azimuthal angle $\delta\psi$ between two molecules for an orthogonal smectic layer. Inset shows the difference in V_{ex} corresponding to $\delta\psi = \pi$ and 0 for different values of β. 28

2.4 The variation of excluded volume V_{ex} as a function of roll angle ψ for the HSC model. 30

2.5 The variation of V_{ex} as a function of roll angle ψ for the bead model. Inset shows the magnified view of the indicated region demonstrating the maximum at $\psi = 180°$ for higher values of θ. 31

2.6 The stability diagram in the θ - β plane representing the regions of stability of the different symmetries of the layers obtained from the excluded volume interactions for bead model of the molecules. 32

2.7 The variation of V_{ex} with tilt angle θ at $\psi = 0$ or π for (a) HSC model and (b) bead model of the molecules. 33

2.8 The favoured tilt angle θ for the bead model of the BC molecules at different values of bending angle β. 34

2.9 Schematic representation of the diffusive cone model describing the orientation of an achiral BC molecule in a de Vries SmA layer. . . . 36

2.10 The representative spin configurations corresponding to the different phases. The blue and red (light gray) arrows denote the orientations of the unit vectors $\hat{\xi}$ and $\hat{p}$ respectively. The open circle and filled square symbols represent $+1$ and -1 values of the Ising spin, respectively. . . 37

2.11 The variation of order parameters with temperature for $A = 0.5$ at zero electric field. Inset shows the corresponding specific heat variation. 38

2.12 The variation of order parameters with electric field for $T/J = 1.8$ and $A = 0.5$. Inset shows the magnified view of the region at low field. . . 39

3.1 Schematic representation of the non-correlated layer model for the de Vries SmA to SmC phase transition. 49

3.2 Schematic representation of the diffusive cone model for the de Vries SmA to SmC phase transition. 50

3.3 The variation of order parameters ζ, u and τ with temperature. The vertical lines represent the phase boundaries. 57

3.4 The variation of layer compression (u) as a function of temperature. . 58

3.5 Numerically obtained phase diagram in $\alpha - A$ parameter's plane for the other parameter set $\beta = 0.32, \gamma = 43, \tilde{B} = 2.0, \lambda_1 = 0.2, \lambda_2 = 0.08, \lambda_3 = 1.5, \lambda_4 = 0.1, \lambda_5 = 0.1$, and $\lambda_6 = 0.1$. The black-coloured continuous line represents a first-order transition line, and the discontinuous (- -) line denotes the second-order phase transition line. Our system follows the path depicted by a black-coloured discontinuous ($\cdots$) line. 60

4.1 The variation of growth rate σ as a function of the wave vector q for different values of α (a) $-0.1 \leq \alpha \leq -0.067$ and (b) $-0.05 \leq \alpha \leq 0.025$. The modes in the wave vector range $0 < q < q_{max}$ have positive values of σ^+ and hence are unstable. The values of the other parameters are $\gamma/A = 0.2236$, $W/A = 0.1$, $\xi_\psi/\xi_\phi = 3.1623$, and $\xi_\phi^2/\lambda_D^2 = 0.5$. 75

4.2 The variation of wavelength and growth rate corresponding to the fastest instability mode (q_c) as a function of α. The values of the other parameters are $\gamma/A = 0.2236$, $W/A = 0.1$, $\xi_\psi/\xi_\phi = 3.1623$, $\xi_\phi^2/\lambda_D^2 = 0.5$. 76

4.3 Three dimensional (3D) plots (a) and (c) of the length scale λ and its growth rate σ^{+}_{max}, respectively, as a function of two model parameters α and ξ_{ϕ}/λ_{D}. Other model parameters are $\gamma/A = 0.7071$, $W/A = 1.0$, and $\xi_{\psi}/\xi_{\phi} = 1.0$. The 2D projections of these 3D plots are (b) and (d), respectively, where the color bars represent the value of λ and σ_{max} in the logarithmic scale. 77

4.4 Three dimensional (3D) plots (a) and (c) of the length scale λ and its growth rate σ^{+}_{max}, respectively, as a function of two model parameters α and ξ_{ψ}/ξ_{ϕ}. Other model parameters are $\gamma/A = 0.7071$, $W/A = 1.0$ and $\xi^{2}_{\phi}/\lambda^{2}_{D} = 5.0$. The 2D projections of these 3D plots are (b) and (d), respectively, where the color bars represent the value of λ and σ_{max} in the logarithmic scale. 78

4.5 Three dimensional (3D) plots (a) and (c) of the length scale λ and its growth rate σ^{+}_{max}, respectively, as a function of two model parameters γ/A and ξ_{ψ}/ξ_{ϕ}. Other model parameters are $\alpha = 0.175$, $W/A = 1.0$ and $\xi^{2}_{\phi}/\lambda^{2}_{D} = 5.0$. The 2D projections of these 3D plots are (b) and (d), respectively, where the color bars represent the value of λ and σ_{max} in the logarithmic scale. 79

4.6 The left and middle panes representing the color-coded variation of the order parameters ϕ and ψ for the ring-banded patterns, whereas the right pane indicating the variation of the free energy density and radius of the ring-banded patterns with time. The model parameters used are (a)$\gamma/A = 0.65, \xi_{\psi}/\xi_{\phi} = 1.20,\ \alpha = 0.175, \beta = 1 + \alpha, \chi = 1.0, W/A = 1.0, \xi^{2}_{\phi}/\lambda^{2}_{D} = 5.0$ and (b)$\gamma/A = 1.0, \xi_{\psi}/\xi_{\phi} = 0.3, \alpha = -0.1, \beta = 0, \chi = 1.0, W/A = 2.0, \xi^{2}_{\phi}/\lambda^{2}_{D} = 20.0$. The time step is chosen as $dt = 0.01$. . 82

4.7 The left and middle panes representing the color-coded variation of the order parameters ϕ and ψ for the broken ring patterns, whereas the right pane indicating the variation of the free energy density and radius of the broken ring patterns with time. The model parameters used are (a) $\gamma/A = 0.55, \xi_\psi/\xi_\phi = 0.75$, and (b)$\gamma/A = 0.5, \xi_\psi/\xi_\phi = 0.45$ where $\alpha = 0.175, \beta = 1 + \alpha, \chi = 1.0, W/A = 1.0$, and $\xi_\phi^2/\lambda_D^2 = 5.0$. The time step is chosen as $dt = 0.01$. 84

4.8 The left and middle panes representing the color-coded variation of the order parameters ϕ and ψ for a continuous pattern, whereas the right pane indicating the variation of the free energy density and radius of the continuous pattern with time. The model parameters used are $\gamma/A = 0.50, \xi_\psi/\xi_\phi = 1.80, \alpha = 0.175, \beta = 1 + \alpha, \chi = 1.0, W/A = 1.0$, and $\xi_\phi^2/\lambda_D^2 = 5.0$. The time step is chosen as $dt = 0.01$. 85

4.9 The stability diagram in the γ/A - ξ_ψ/ξ_ϕ parameter plane representing the regions of the stability of the different patterns such as ring banded, broken ring and continuous patterns for the model parameters $\alpha = 0.175, \beta = 1 + \alpha, \chi = 1.0, W/A = 1.0$ and $\xi_\phi^2/\lambda_D^2 = 5.0$. The color bar denotes the fastest-growing instability length scale λ obtained from LSA. The dotted and dashed lines are schematically drawn to represent the stability boundaries. 86

4.10 The color-coded representation of the order parameters ϕ and ψ for the intermediate patterns. The model parameters used are (a)$\gamma/A = 0.45, \xi_\psi/\xi_\phi = 1.25$,(b) $\gamma/A = 0.5, \xi_\psi/\xi_\phi = 1.15$,(c)$\gamma/A = 0.6, \xi_\psi/\xi_\phi = 1.27$, (d) $\gamma/A = 0.75, \xi_\psi/\xi_\phi = 1.55$, and (e) $\gamma/A = 0.75, \xi_\psi/\xi_\phi = 1.56$ where $\alpha = 0.175, \beta = 1 + \alpha, \chi = 1.0, W/A = 1.0$, and $\xi_\phi^2/\lambda_D^2 = 5.0$. (f) The variation of the free energy density of these intermediate patterns with time. The graphs 1, 2, 3, 4 and 5 correspond to the patterns (a),(b),(c),(d) and (e) respectively. The time step is chosen as $dt = 0.001$. 87

5.1 The polarised optical microscope (POM) images of a continuous spherulite of 8OCB (a) between crossed polarisers and (b) with a λ-plate inserted in the optical path in addition to the crossed polarisers. The direction of the major refractive index in the sample plane is denoted by white double-headed arrows around the seed. The dark arms of the Maltese cross parallel to the polarisers remain invariant in the rotation of the sample between the crossed polarisers. 96

5.2 The polarised optical microscope (POM) images of a banded spherulite of 8OCB (a) between crossed polarisers and (b) with a λ-plate inserted in the optical path in addition to the crossed polarisers. The direction of the major refractive index in the sample plane is denoted by white double-headed arrows around the seed. 97

5.3 Schematic representation of coherent twisting of fibrils in a banded spherulite 97

5.4 (a) The scanning electron microscopic image of a banded spherulitic region showing the presence of alternating fibrous nano-crystallite rich domains and amorphous domains. (b) The fluorescent image of a dye-doped banded spherulitic region. The regions marked “A” and “B” represent the concentric crystallite-rich and crystallite-poor bands, respectively. 99

5.5 Effect of supercooling on banded spherulite. (a) The variation of growth rate σ with the wave vector q for different values of α. The modes in the wave vector range $0 < q < q_{max}$ are unstable. (b) The variation of q_{max} and q_c as a function of α. (c) Comparison between experimental, linear stability analysis and simulation results for the variation of band spacing with supercooling ΔT. The values of the parameters used for the theoretical model are $\gamma/A = 0.242$, $W/A = 0.1$, $\xi_\phi = 0.04$ μm, $\xi_\psi = 3.16\xi_\phi$, $\lambda_D = 1.41\xi_\phi$. 104

5.6 Simulated banded spherulite domain. The color-coded representation of the order parameters (a) ϕ and (b) ψ of a banded spherulite obtained from the numerical solution of the TDGL equations at ΔT = 39.5 K. The model parameters used are $\gamma/A = 0.242$, $W/A = 0.1$, $\zeta_\phi = 0.04$ μm, $\zeta_\psi = 3.16\zeta_\phi$, $\lambda_D = 1.41\zeta_\phi$, time step size $dt = 0.01$ and spatial step size $dx = dy = 1.0$. (c) The graphical profiles of ϕ and ψ along a radial axis of the simulated banded spherulite. 105

5.7 Simulated banded spherulite patterns for different values of supercooling. Numerical solutions of ϕ (upper row) and ψ (lower row) for different values of α (or ΔT). (a, b) $\alpha = 0.250$ (ΔT = 40.8 K) at 149999 time steps, (c, d) $\alpha = 0.300$ (ΔT = 38.1 K) at 199999 time steps, (e, f) $\alpha = 0.450$ (ΔT = 29.9 K) at 399999 time steps on a 1024×1024 square lattice. 106

5.8 Rhythmic variation of banded spherulite radius. Numerically computed variation of radius R of the banded spherulite with time showing its rhythmic growth for $\alpha = 0.15$ (ΔT = 46.3 K). The blue line shows the average linear growth of the spherulite with time. R and t are dimensionless quantities. 107

6.1 Schematic representation of an incompressible thin sheet floating on the nematic substrate. The sheet is subject to a unidirectional compression Δ along the x-axis. The deformation of the thin sheet is confined in the xz plane. 116

6.2 Schematic representation of the nematic director field. 120

6.3 The variation of the energy density ε as a function of the wave vector q for (a) the planar anchoring condition and (b) hybrid anchoring condition where $\tilde{K} = 0.25$ and $\delta = 0.1$. 127

6.4 The variation of the optimal wave vector q_c as a function of the effective elastic constant $\tilde{K}$ for the planar anchoring conditions of the nematic director field. 128

6.5 Representing the results for the hybrid anchoring condition of the nematic director field. (a) The variation of the optimal wave vector q_c as a function of the effective elastic constant $\tilde{K}$ for different values of δ. (b) The variation of q_c as a function of δ for different values of $\tilde{K}$. . . 129

List of Tables

2.1 The observed phase sequences for different values of A. 40

Chapter 1

Introduction

Solid, liquid, and gas are the three commonly known states of materials. In the solid state, constituent particles primarily arrange themselves in a regular lattice structure, whereas they exhibit no long-range positional order in both the liquid and gas states. In addition to these three states, some materials consisting of strongly anisotropic molecules exhibit intermediate states between their ordered crystalline state and disordered isotropic liquid state that are known as liquid crystalline materials or liquid crystals. These intermediate phases, commonly known as liquid crystalline phases or mesophases, have flow properties just like liquids, as well as anisotropic physical properties like crystals. Some of these mesophases are schematically shown in figure 1.1. Due to the tunable electro-optical properties, the liquid crystals are widely used in

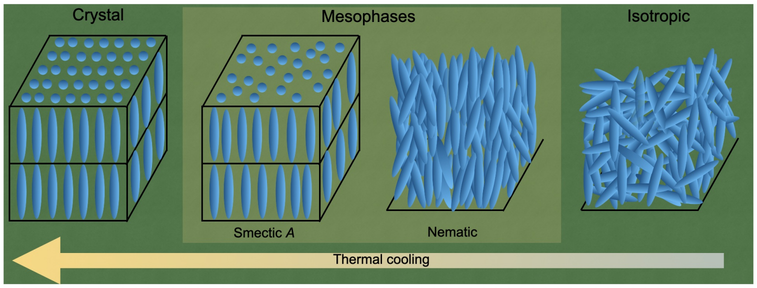

Figure 1.1: Schematic representation of the crystal, isotropic, and intermediate phases of a liquid crystalline system constituting rodlike particles.

technological applications such as displays, sensors, optical modulators, etc. Besides their applications, these soft materials provide ample opportunities for the fundamental understanding of natural phenomena such as dynamics of topological defects, spontaneous symmetry-breaking phenomena, and order-disorder transitions. Furthermore, the knowledge of liquid crystalline systems can be utilized to understand other systems such as polymers, colloids, biological systems, and granular media wherein the orientational order can be observed.

1.1 Liquid crystalline phases

Liquid crystal was first found experimentally by Austrian botanist Friedrich Reinitzer in 1888 [1, 2]. Based on the experimental studies conducted since its discovery, it can be primarily classified into two groups: lyotropic liquid crystal and thermotropic liquid crystal. The lyotropic system is associated with the mixture or solution containing solute and solvent molecules. Living organisms, colloidal suspension, and surfactant solutions are good examples of lyotropic liquid crystalline systems. Liquid crystalline properties in this system are strongly determined by the concentration of solute molecules. On the other hand, the compounds consisting of anisotropic molecules that exhibit the liquid crystalline phases on heating or cooling are known as thermotropic liquid crystals. For both the lyotropic and thermotropic liquid crystals, the anisotropic shape of the constituent molecules/particles strongly determines the existence of mesomorphic phases. So far, various thermotropic liquid crystalline compounds comprised of molecules with different shapes (see figure 1.2) such as rod-like (calamatic), disk-like (discotic) [3], and bent-core banana-shaped [4] have been synthesized. These compounds exhibit a wide variety of mesophases such as nematic, cholesteric, smectic A, smectic C, blue phases, columnar phases, and banana phases (i.e. B_1, B_2, B_4, B_6 and B_7 phases) [5–12]. In the following, we discuss the self-

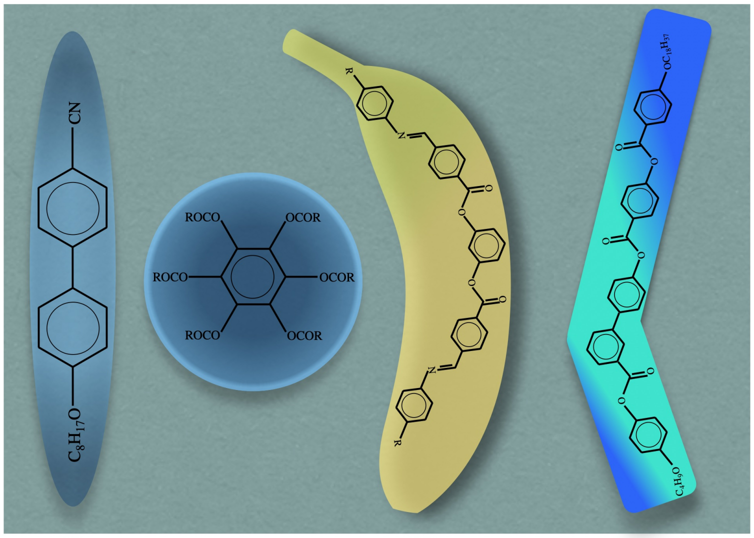

Figure 1.2: Schematic representation of different shaped liquid crystalline molecules from left rodlike (8OCB), discotic (Benzene haxa alkanoates), Bent-core, and Hockey stick molecules.

assembled structural organization of molecules in some of these mesophases and their macroscopic symmetries.

1.1.1 Nematic phase

In the uniaxial nematic phase, anisotropic rodlike molecules align their long axes on average in a preferred direction while there is no long-range positional order of the center of masses of the molecules. Thus, the nematic phase has a long-range orientational order but is essentially a liquid state due to the absence of a truly positional order. The average alignment direction of the molecular long axes is called the director, which is usually denoted by a unit vector $\hat{n}$. The long axes of the molecules align equally likely along $\hat{n}$ and $-\hat{n}$ in the nematic phase, giving rise to the $\hat{n} \leftrightarrow -\hat{n}$ symmetry of the medium. Therefore, the uniaxial nematic phase has the $D_{\infty h}$ point symmetry. The typical molecular arrangement in the nematic phase is shown in figure 1.3.

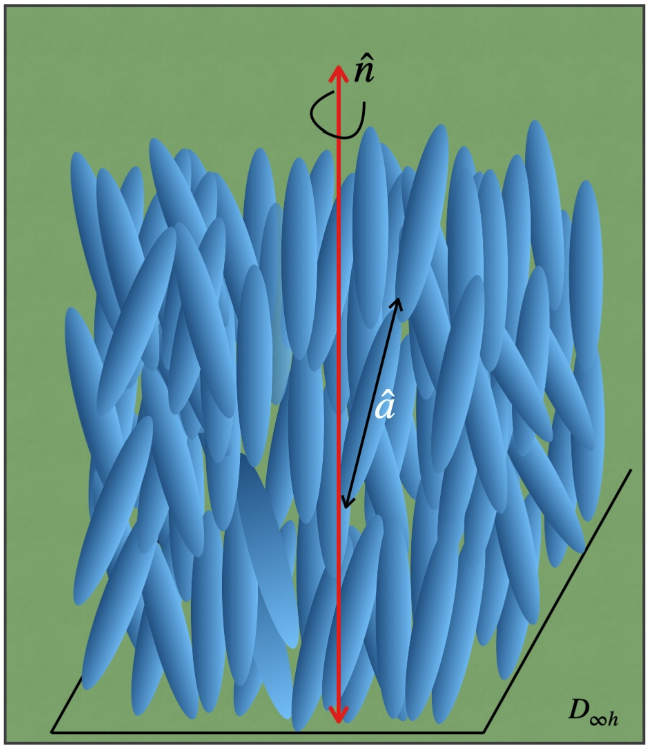

Figure 1.3: Schematic representation of molecular arrangement in the uniaxial nematic phase. The nematic director $\hat{n}$ and the long axis of a molecule $\hat{a}$ are denoted by the double-headed red and black arrows, respectively.

Orientational Order Parameter

A macroscopic physical quantity known as the order parameter is usually defined to describe the transition between two phases. Across the transition from the high symmetry to the low symmetry phase, the order parameter changes from zero to a non-zero value. Thus, the order parameter is defined so that a non-zero value corresponds to the ordered lower symmetry state, and the null value represents the disordered higher symmetry state. The order parameter can be a scalar, vector, tensor, or even a complex quantity, depending on the system. Here, we define the orientational order parameter corresponding to the isotropic to uniaxial nematic phase transition for anisotropic rodlike molecular systems. Both the isotropic and nematic phases are characterized by liquid-like order with no long-range positional order of the molecules. However, the nematic phase is associated with a long-range orientational order of the long axes of the molecules. In both these phases, the positions of the molecular center of mass are randomly distributed over space, ascribing the fluid nature of the phases.

To describe the orientational order in the nematic phase, an order parameter can be defined as follows. For convenience, we assume the molecules have a rigid rodlike shape, and the orientation of the long axis of a rodlike molecule is denoted by a unit vector $\hat{a}$. To specify the average orientation of the long axes of the molecules at a point $\vec{r} = (x, y, z)$, we utilize the thermal average of the relevant tensors that are composed of $\hat{a}$ over a small but macroscopic volume around the point $\vec{r}$. Naturally, the first choice is a tensor with rank one given by $\langle \hat{a} \rangle$ where the angular brackets $\langle\rangle$ denote the ensemble average and it represents a vector order or polar order in the system. This order parameter is analogous to the magnetization in a ferromagnet. However, in the nematic phase, though there is an alignment of the molecular long axes along a preferred direction $\hat{n}$, but no polar order is found. Thus, the director $\hat{n}$ is apolar in nature with $\hat{n} \leftrightarrow -\hat{n}$ symmetry. Therefore, a second-rank tensor Q is considered as the order parameter for the isotropic to uniaxial nematic phase transition, and the element of the tensor is defined as

$$Q_{ij} = \langle a_i a_j - \frac{\delta_{ij}}{3} \rangle$$

where i, j are cartesian indices. According to the definition, the tensor Q should be zero for the isotropic phase that is ensured by the Kronecker delta as $\langle a_i^2 \rangle = 1/3$. In general, the symmetric traceless tensor order parameter Q has five independent elements, and it can be brought to a diagonal form in the principal coordinate frame. For the uniaxial nematic phase, this tensor can be written as

$$Q_{ij} = S(n_i n_j - \frac{\delta_{ij}}{3}) \tag{1.1}$$

where the scalar S measures the degree of alignment of the long axes of the molecules along the nematic director $\hat{n}$ and is defined as

$$S = \frac{1}{2}\langle 3(\hat{a} \cdot \hat{n})^2 - 1 \rangle. \tag{1.2}$$

The order parameter S vanishes in the isotropic phase, and it becomes non-zero in the nematic phase. In principle, the scalar order parameter S lies in a range $-1/2 \leq S \leq 1$. $S = 1$ represents the perfect molecular alignment along the director, whereas $S = -1/2$ corresponds to the confinement of the long axes of the molecules in a plane perpendicular to the director. In general, the positive values of order S are associated with the prolate-shaped or rodlike molecules.

Landau-de Gennes theory

A simple phenomenological Landau-type theory can be constructed by utilizing the orientational order parameter Q_{ij} to describe the isotropic-Nematic transition [5–7]. This theory was first developed by de Gennes [5]. Generally, to construct a Landau-type theory accounting for a phase transition, the free energy density of a system is expanded in terms of its order parameter, where the order parameter is assumed to be small, and hence, the terms involving the higher power of the order parameter are often neglected. The terms in the free energy density must be symmetry-invariant with respect to the high symmetry phase. Based on these arguments, the free energy density of the nematic phase can be expressed as

$$f = f_0 + \frac{A}{2} Tr(Q^2) + \frac{B}{3} Tr(Q^3) + \frac{C_1}{4}(TrQ^2)^2 + \frac{C_2}{4} TrQ^4 \tag{1.3}$$

where f_0 is the free energy density of the isotropic phase, and the coefficients A, B, C_1, and C_2 are the coefficients of the respective terms involving the trace of the powers of the order parameter tensor Q. These constants, in general, depend on the temperature and properties of the materials. In this free energy density expansion, the terms consistent with the symmetries of the isotropic phase are the rotational-invariant quantities and are retained up to the fourth power. Using the expression 1.1 of the tensor Q_{ij}, the free energy density can be written as

$$f = f_0 + \frac{a}{2}S^2 + \frac{b}{3}S^3 + \frac{c}{4}S^4 \tag{1.4}$$

where $a = 2A/3, b = 2B/9$, and $c = (4C_1 + 2C_2)/9$. The condition $c > 0$ is needed for the stability of the phases. The possibility of the different phases can be determined by minimizing the free energy density with respect to S. The extrema of the free energy density satisfy

$$\frac{df}{dS} \equiv aS + bS^2 + cS^3 = 0 \tag{1.5}$$

and the roots of this equation are

$$S = 0, \frac{-b + \sqrt{b^2 - 4ac}}{2c}, \frac{-b - \sqrt{b^2 - 4ac}}{2c}. \tag{1.6}$$

The root corresponding to the minimum value of the free energy represents the equilibrium value of the order parameter. This equilibrium value varies with temperature across the phase transition. In Landau theory, it is generally assumed that the coefficient a is the only temperature-dependent quantity, and it is also assumed to follow a linear relation $a(T) = a'(T - T_0)$ where a' is a constant and T_0 is the supercooling limit of the isotropic phase.

Figure 1.4 (a) shows the variation of the free energy density as a function of the order parameter S at different temperatures. The free energy density at high temperatures (i.e., $a >> 0$) has only a minimum at $S = 0$ corresponding to the isotropic phase. The nematic phase with $S \neq 0$ becomes stable at lower temperatures. The isotropic-nematic transition temperature T_{NI} can be determined by equating the free energy of the nematic phase to that of the isotropic phase, i.e., $f(S = S_{NI}, T = T_{NI}) = f(S = 0, T = T_{NI})$ where S_{NI} is the value of the order parameter for the nematic phase at $T = T_{NI}$. Therefore, one can write

$$\frac{aS_{NI}^2}{2} + \frac{b}{3}S_{NI}^3 + \frac{c}{4}S_{NI}^4 = 0 \tag{1.7}$$

and S_{NI} also satisfies equation 1.5. Using equations 1.5 and 1.7, we obtain $S_{NI} = -\frac{2b}{3c} = -\frac{3a}{b}$. Therefore, we have $a(T_{NI}) = \frac{2b^2}{9c}$. The expression of the transition temperature becomes

$$T_{NI} = T_0 + \frac{2b^2}{9a'c} \tag{1.8}$$

The variation of the equilibrium value of the order parameter S as a function of temperature is shown in figure 1.4 (b). In the isotropic phase, S is equal to zero and undergoes a first-order transition to the nematic phase, showing a jump discontinuity.

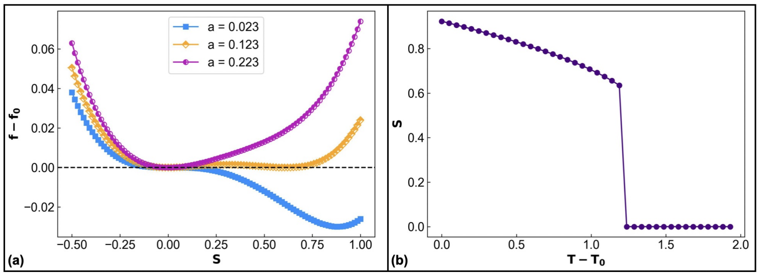

Figure 1.4: (a) The variation of the free energy density as a function of the order parameter for different values of a. (b) The variation of the order parameter S as a function of temperature. Where the other constants are $a' = 0.1, b = -0.6$ and $c = 0.65$.

Nematic Elastic energy

In the previous section, we discuss the phenomenological theory for isotropic to nematic transition, assuming the homogeneity or uniformity of the order parameter throughout the sample. In the real system, the order parameter can vary over the space depending on various parameters, such as applied field and surface anchoring conditions. The spatial variation of the order parameter gives rise to a higher energy state of the system from its homogeneous ground state. The energy cost due to the spatial variation of the order parameter can be included in the free energy density through the terms composed of the gradients of the order parameter. For the construction of this elastic energy cost, it is generally assumed that the order parameter varies slowly over space. Therefore, the symmetry invariant terms involving the lower order gradients of the order parameter are often considered in the elastic energy expansion. Neglecting the higher-order terms, the nematic elastic energy is given by

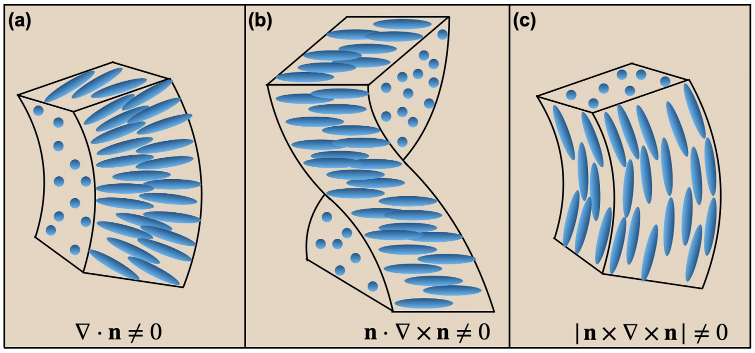
(a)
(b)
(c)
$\nabla\cdot\mathbf{n}\neq 0$
$\mathbf{n}\cdot\nabla\times\mathbf{n}\neq 0$
$|\mathbf{n}\times\nabla\times\mathbf{n}|\neq 0$

Figure 1.5: Schematic representation of the three elastic deformation modes of the nematic director field: (a) splay, (b) twist, and (c) bend deformation modes.

$$f_e = \frac{L_1}{2}\frac{\partial Q_{ij}}{\partial x_k}\frac{\partial Q_{ij}}{\partial x_k} + \frac{L_2}{2}\frac{\partial Q_{ij}}{\partial x_i}\frac{\partial Q_{jk}}{\partial x_k} + \frac{L_3}{2}\frac{\partial Q_{jk}}{\partial x_i}\frac{\partial Q_{ik}}{\partial x_j} \tag{1.9}$$

where L_1, L_2 and L_3 are positive elastic constants [7]. Sometimes, the scalar order parameter S is assumed to be fixed over space. In this case, the spatial variation occurs through the changes in orientation of the director field $\hat{n}(\vec{r})$. By assuming the slow variation in the director field, the elastic free energy density of the system can be expressed as

$$f_e = \frac{K_1}{2}(\nabla\cdot\mathbf{n})^2 + \frac{K_2}{2}(\mathbf{n}\cdot\nabla\times\mathbf{n})^2 + \frac{K_3}{2}(\mathbf{n}\times\nabla\times\mathbf{n})^2 \tag{1.10}$$

where K_1, K_2 and K_3 are the elastic constants corresponding to the three modes of the director field deformations, namely splay, twist, and bend elastic deformations, respectively [5, 7]. This elastic free energy density is commonly known as the Oseen-Frank elastic energy. The Frank elastic constants K_1, K_2 and K_3 are proportional to the square of the scalar order parameter S and are also related to the elastic constants L_1, L_2 and L_3 [7, 13]. Figure 1.5 schematically represents these three modes of the director field deformations.

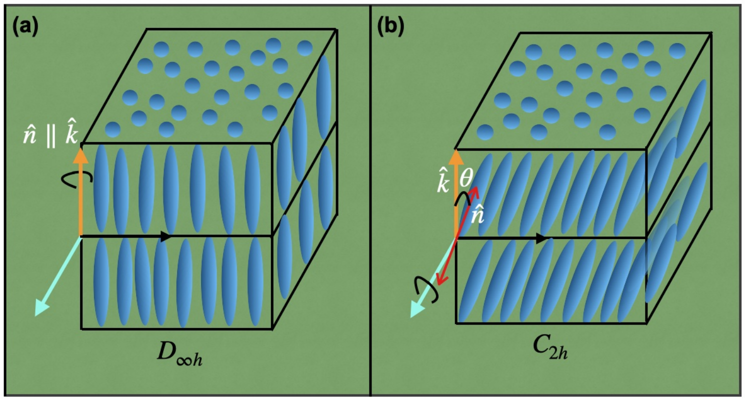

Figure 1.6: Schematic representation of the molecular arrangement in the (a) smectic A and (b) smectic C phases.

1.1.2 Smectic phases

In the smectic phases, the molecules exhibit lamellar order or layered structure in addition to the long-range orientational order. The layered structure gives rise to a one-dimensional positional order of the center of mass of the molecules along the layer normal. However, in the plane of the layer, there is no long-range positional order of the molecules. Thus, the smectic phases usually have fluid lamellar structures. Various kinds of smectic phases, such as smectic A, de Vries smectic A, smectic C phases, etc, have been observed [5, 14, 15]. The typical molecular arrangement in the smectic phases is shown in figure 1.6.

In the Smectic A phase, the average orientation of the long axes of the molecules, i.e., the director $\hat{n}$, align along the layer normal, and the layer spacing d is similar to the molecular length l. The Smectic A phase is also characterized by the $D_{\infty h}$ point symmetry. In the smectic C phase, the director tilts away from the layer normal with a temperature-dependent tilt angle and the tilt direction of the director is uniform from layer to layer. The tilted organization of the molecules gives rise to the layer spacing $d = l \cos\theta$, where l is the molecular length and θ is the tilt angle. Thus, the smectic C phase has the C_{2h} point symmetry.

For some compounds, the Smectic A phase undergoes a transition to the Smectic C phase on cooling, and the layer spacing decreases with decreasing temperature across this $A - C$ transition. The layer spacing often changes by about 10% across this transition. For some materials, the layer spacing in the Smectic A phase is found to be significantly smaller than the molecular length. Moreover, when this smectic A phase undergoes a transition to the smectic C phase, no significant change in the layer spacing is observed [14, 15]. These materials are called de Vries materials, and the corresponding smectic A phase is known as de Vries Smectic A phase. In the de Vries Smectic A phase, molecular long axes are tilted about the layer normal with a certain angle, but the molecular tilt directions are random. The de Vries Smectic A phase is also a uniaxial phase with a $D_{\infty h}$ point symmetry.

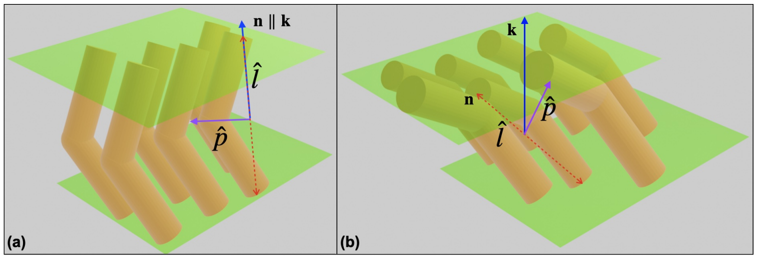

Figure 1.7: Schematic representation of the molecular arrangement in perfectly ordered (a) polar smectic A (SmAP) and (b) tilted polar smectic (SmCP) layers of bent-core molecules. The long axis and the polar direction of a bent-core molecule are denoted by the unit vectors $\hat{l}$ and $\hat{p}$, respectively.

1.1.3 Polar smectic phases

All the phases mentioned above are nonpolar in nature. The mesophases with polar order can easily couple linearly with the external field and can impact technological applications. Therefore, the search for new mesophases with the long-range polar order is an active field of research. In this context, some materials, especially bent-core systems, are known to exhibit long-range polar order in some of their mesophases [16, 17]. For instance, in the polar smectic A (SmAP) layer, the average orientation $\hat{n}$ of the molecular long axes is along the layer normal, and the bending/polar axes of the bent-core molecules are also aligned along a preferred direction, giving rise to the polar order in the plane of the layer. Figure 1.7 (a) schematically shows the orientation of the bent-core molecules in a SmAP layer. It should be noted that the smectic A phase consisting of SmAP layers can exhibit either ferroelectric or antiferroelectric properties depending on the direction of the inter-layer polar orders [16]. It has also been found that the bent-core liquid crystal displays polar order in some of their smectic C phases. In the tilted polar smectic C (SmCP) layer, as shown in figure 1.7 (b), the director $\hat{n}$ is tilted with respect to the layer normal, and the bending axes of the bent-core molecules are aligned along a preferred direction, giving rise to the polar order in the layer. Interestingly, the SmCP layer consisting of achiral bent-core molecules can exhibit spontaneous breaking of chiral symmetry [18]. Depending on the orientation of the polar order and chirality in successive layers, a rich variety of self-assembled structures are possible [17]. It is experimentally found that the bent-core liquid crystal mostly displays the smectic C phase known as B_2 phase where the direction of the polar order is perpendicular to both the layer normal and the director $\hat{n}$ giving rise to the layer chirality.

1.2 Growth of solid Phases

Liquid crystal solidifies when it is cooled below its freezing point. In general, solidification processes are often described by two growth mechanisms such as diffusion- and kinetic-limited growths. In the first mechanism, the diffusion of latent heat or impurity away from the interface primarily controls the solidification rate. This type of diffusion-limited process can cause the instability of a flat interface, leading to dendritic growth morphology. This instability is accounted for by the well-known Mullin-Sekerka theory [19]. The dendritic morphology essentially grows as a homogeneous crystal phase with a very complex boundary. In the second mechanism, diffusion is no longer important, but the molecular attachment kinetics at the interface control the solidification rate. This may lead to a variety of phenomena, including non-crystallographic branching, defect generation, and polycrystalline solids. The activation of these two growth processes depends on the solidification conditions, such as under-cooling. Depending on these solidification conditions, liquid crystals can exhibit various types of macroscopic morphologies, including needle crystals, faceted crystals, dendrites, and spherulites [20–23]. The spherulitic growth has also been seen in a wide variety of materials, including minerals, salts, biological materials, polymers, and alloys [24]. However, despite a large number of studies over a century since its discovery, a general theory accounting for spherulitic growth is still lacking. Also, the understanding of spherulitic structures is necessary to design new materials as it affects the mechanical properties of a solid, such as brittleness. In the following, we briefly discuss the spherulitic structures.

1.2.1 Spherulites

In the spherulitic growth, the solid phase after nucleation grows with a spherical growth front with continuous orientational symmetry in contrast to the growth of a

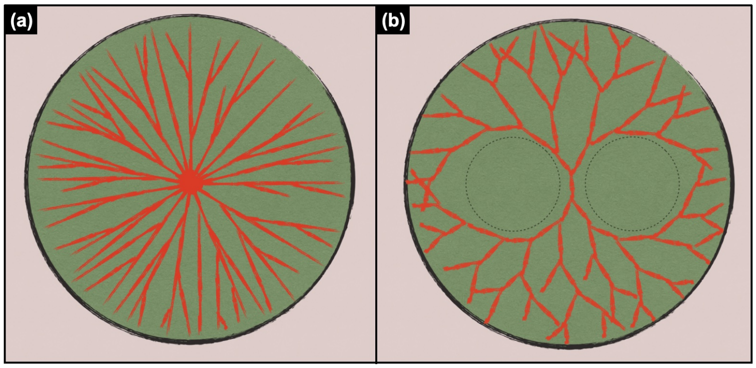

Figure 1.8: Schematic representation of a spherulite domain. (a) The domain is formed by multiple fibrils emanating from a single nucleation site. (b) The domain starts to grow from a bunch of fibrils and continues to grow due to non-crystallographic branching. At a long time, the domain attains a spherical growth front, giving rise to the “sheaf of wheat” structure.

crystal having discrete orientational symmetries. The spherulitic growth morphology is often associated with the formation of many radially aligned fibrillar crystallites that branch noncrystallographically to fill space during the growth [25]. This distinct characteristic of spherulites separates them from the other polycrystalline aggregates. Spherulitic structures are often distinguished into two categories based on their initial development [26, 27]. In the first one, the spherulitic domain nucleates from a single site by emanating multiple fibrillar crystals, as shown in figure 1.8 (a). The fibrillar crystals branch noncrystallographically to fill the space, and the structure grows radially. In the other case shown in figure 1.8 (b), the nucleation of a spherulitic domain begins as a single fibrillar crystal from which new fibrils are produced through non-crystallographic branching. The fibrils start to align radially as the structure grows, which leads to a spherical envelope. This process produces two “eyes” (uncrystallized zones) on both sides of the nucleation site as represented by the dotted circle in figure 1.8 (b). This structure is often known as a “sheaf of wheat” morphology due to its apparent similarity to a tied sheaf of wheat. The typical microscopic textures of the spherulites are shown in figure 1.9. The polarised optical microscope image of a spherulitic domain of 8OCB liquid crystal on crystallization from its smectic A phase is shown in figure 1.9 (a) and figure 1.9 (b) shows the same image when a λ plate is inserted in the light path of the microscope. The scanning electron microscopic image of the spherulitic domain of 8OCB liquid crystal is shown in figure 1.9 (c) and (d).

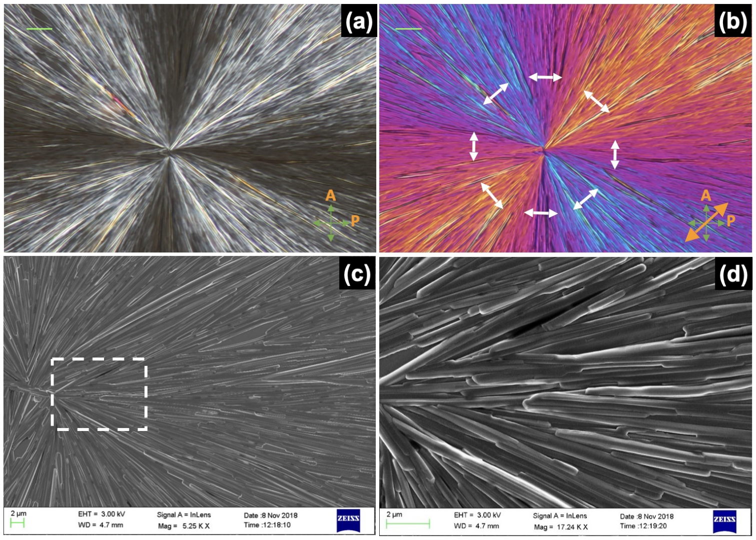
(a)
A
P
(b)
A
P
(c)
2 µm
EHT = 3.00 kV
WD = 4.7 mm
Signal A = InLens
Mag = 5.25 K X
Date :8 Nov 2018
Time :12:18:10
ZEISS
(d)
2 µm
EHT = 3.00 kV
WD = 4.7 mm
Signal A = InLens
Mag = 17.24 K X
Date :8 Nov 2018
Time :12:19:20
ZEISS

Figure 1.9: The polarised optical microscope (POM) images of a spherulite of 8OCB (a) between crossed polarisers and (b) with a λ-plate inserted in the optical path in addition to the crossed polarisers. The direction of the major refractive index in the sample plane is denoted by white double-headed arrows around the seed. (c) The scanning electron microscopic image of a spherulitic region showing the presence of fibrils. (d) The zoomed view of the indicated box in (c).

Bibliography

[1] F. Reinitzer, Monatshefte für Chemie und verwandte Teile anderer Wissenschaften **9**, 421 (1888), URL `https://doi.org/10.1007/BF01516710`.

[2] F. Reinitzer, Liquid Crystals **5**, 7 (1989), `https://doi.org/10.1080/02678298908026349`, URL `https://doi.org/10.1080/02678298908026349`.

[3] S. Chandrasekhar, B. K. Sadashiva, and K. A. Suresh, Pramana **9**, 471 (1977), URL `https://doi.org/10.1007/BF02846252`.

[4] D. Malkar and A. Roy, Liquid Crystals **49**, 1147 (2022), `https://doi.org/10.`

1080/02678292.2022.2076941, URL `https://doi.org/10.1080/02678292.2022.2076941`.

[5] P. G. de Gennes and J. Prost, *The Physics of Liquid Crystals* (Clarendon Press, Oxford, 1995).

[6] M. J. Stephen and J. P. Straley, Rev. Mod. Phys. **46**, 617 (1974), URL `https://link.aps.org/doi/10.1103/RevModPhys.46.617`.

[7] D. Andrienko, Journal of Molecular Liquids **267**, 520 (2018), ISSN 0167-7322, special Issue Dedicated to the Memory of Professor Y. Reznikov, URL `https://www.sciencedirect.com/science/article/pii/S016773221735314X`.

[8] H. K. Bisoyi and Q. Li, Chemical Reviews **122**, 4887 (2022), pMID: 34941251, `https://doi.org/10.1021/acs.chemrev.1c00761`, URL `https://doi.org/10.1021/acs.chemrev.1c00761`.

[9] H. Takezoe and Y. Takanishi, Japanese Journal of Applied Physics **45**, 597 (2006), URL `https://doi.org/10.1143%2Fjjap.45.597`.

[10] R. A. Reddy and C. Tschierske, J. Mater. Chem. **16**, 907 (2006), URL `http://dx.doi.org/10.1039/B504400F`.

[11] A. Eremin and A. Jákli, Soft Matter **9**, 615 (2013), URL `http://dx.doi.org/10.1039/C2SM26780B`.

[12] A. Jákli, O. D. Lavrentovich, and J. V. Selinger, Rev. Mod. Phys. **90**, 045004 (2018), URL `https://link.aps.org/doi/10.1103/RevModPhys.90.045004`.

[13] H. Mori, J. Eugene C. Gartland, J. R. Kelly, and P. J. Bos, Japanese Journal of Applied Physics **38**, 135 (1999), URL `https://dx.doi.org/10.1143/JJAP.38.135`.

[14] A. D. Vries, Molecular Crystals and Liquid Crystals **41**, 27 (1977), `https://doi.org/10.1080/01406567708071949`, URL `https://doi.org/10.1080/01406567708071949`.

[15] A. de Vries, The Journal of Chemical Physics **71**, 25 (2008), ISSN 0021-9606, `https://pubs.aip.org/aip/jcp/article-pdf/71/1/25/15355965/25_1_online.pdf`, URL `https://doi.org/10.1063/1.438123`.

[16] T. Niori, T. Sekine, J. Watanabe, T. Furukawa, and H. Takezoe, J. Mater. Chem. **6**, 1231 (1996), URL `http://dx.doi.org/10.1039/JM9960601231`.

[17] D. R. Link, G. Natale, R. Shao, J. E. Maclennan, N. A. Clark, E. Körblova, and D. M. Walba, Science **278**, 1924 (1997), ISSN 0036-8075, `https://science.sciencemag.org/content/278/5345/1924.full.pdf`, URL `https://science.sciencemag.org/content/278/5345/1924`.

[18] D. Patra and A. Roy, Phys. Rev. E **107**, 034704 (2023), URL `https://link.aps.org/doi/10.1103/PhysRevE.107.034704`.

[19] W. W. Mullins and R. F. Sekerka, Journal of Applied Physics **35**, 444 (1964), ISSN 0021-8979, `https://pubs.aip.org/aip/jap/article-pdf/35/2/444/18330862/444_1_online.pdf`, URL `https://doi.org/10.1063/1.1713333`.

[20] J. L. Hutter and J. Bechhoefer, Phys. Rev. Lett. **79**, 4022 (1997), URL `https://link.aps.org/doi/10.1103/PhysRevLett.79.4022`.

[21] J. L. Hutter and J. Bechhoefer, Physica A: Statistical Mechanics and its Applications **239**, 103 (1997), ISSN 0378-4371, URL `https://www.sciencedirect.com/science/article/pii/S0378437197000241`.

[22] J. L. Hutter and J. Bechhoefer, Phys. Rev. E **59**, 4342 (1999), URL `https://link.aps.org/doi/10.1103/PhysRevE.59.4342`.

[23] S. Ghosh and A. Roy, RSC Adv. **11**, 4958 (2021), URL `http://dx.doi.org/10.1039/D0RA08543J`.

[24] A. G. Shtukenberg, Y. O. Punin, E. Gunn, and B. Kahr, Chemical Reviews **112**, 1805 (2012), pMID: 22103741, `https://doi.org/10.1021/cr200297f`, URL `https://doi.org/10.1021/cr200297f`.

[25] H. D. Keith and J. Padden, F. J., Journal of Applied Physics **34**, 2409 (2004), ISSN 0021-8979, `https://pubs.aip.org/aip/jap/article-pdf/34/8/2409/7933680/2409_1_online.pdf`, URL `https://doi.org/10.1063/1.1702757`.

[26] L. Gránásy, T. Pusztai, G. Tegze, J. A. Warren, and J. F. Douglas, Phys. Rev. E **72**, 011605 (2005), URL `https://link.aps.org/doi/10.1103/PhysRevE.72.011605`.

[27] B. Crist and J. M. Schultz, Progress in Polymer Science **56**, 1 (2016), ISSN 0079-6700, URL `https://www.sciencedirect.com/science/article/pii/S0079670015001288`.

Chapter 2

Spontaneous breaking of chiral symmetry in achiral bent-core liquid crystals: Excluded volume effect

---

Bent-Core banana-shaped molecules exhibit tilted polar smectic phases with macroscopically chiral layer order even though the constituent molecules are achiral in nature. Here, we show that the excluded volume interactions between the bent-core molecules account for this spontaneous breaking of chiral symmetry in the layer. We have numerically computed excluded volume between two rigid bent-core molecules in a layer using two types of model structures of them and explored the different possible symmetries of the layer that are favored by the excluded volume effect. For both model structures of the molecule, the C_2 symmetric layer structure is favored for most values of tilt and bending angle. However, the C_s and C_1 point symmetries of the layer are also possible for one of the model structures of the molecules. We have also developed a coupled XY-Ising model and performed Monte Carlo simulations to explain the statistical origin of spontaneous chiral symmetry breaking in this system. The coupled XY-Ising model accounts for the experimentally observed phase transitions as a function of temperature and electric field.

2.1 Introduction

Chirality is associated with many natural phenomena occurring in microscopic as well as in macroscopic systems. According to Lord Kelvin, an object is *chiral* when it is not superimposable with its mirror image. Chirality is manifested in various liquid crystalline phases such as cholesteric phase, blue phases, chiral smectic phases, twist-bend nematic phases, etc. [1, 2]. In general, a macroscopic phase shows chirality when its constituent molecules are chiral. But, achiral molecules can sometimes exhibit macroscopic chiral phases leading to spontaneous breaking of chiral symmetry. The bent-core (BC) banana-shaped molecules are now known to exhibit such chiral symmetry breaking in some of their liquid crystalline phases [3–5]. The underlying microscopic molecular mechanism responsible for this chiral symmetry breaking is still not well understood.

The BC molecule consists of two rigid rodlike arms joined end to end at an angle of about 120 degrees between them. In addition, flexible aliphatic chains are usually attached at both the free ends of the molecule. The line joining the ends of the molecule is defined as the long axis. Because of the bent shape of the molecule, it has a transverse shape polarity giving rise to the C_{2v} point symmetry and the BC banana-shaped molecules are *achiral* in nature. In their tilted polar smectic phases, the BC molecules arrange themselves in fluid layers and their long axes on average tilted with respect to the layer normal in a given layer as shown in figure 2.1. The average orientation direction of the long axis $\hat{l}$ of the molecules in a layer is denoted by the apolar unit vector $\hat{n}$ known as the director. In addition, the transverse bending

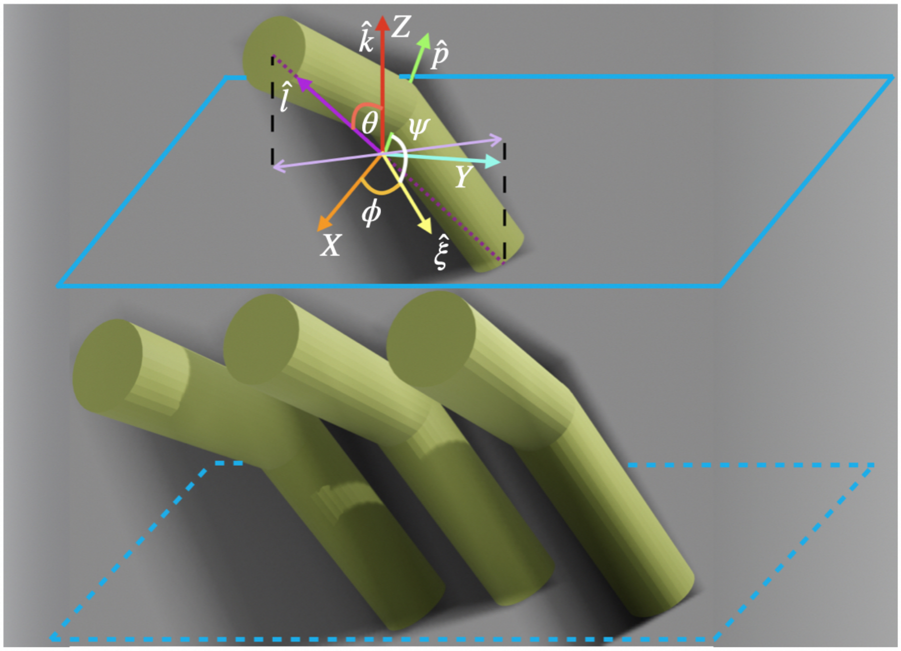

Figure 2.1: Schematic representation of the orientation of a BC molecule in a perfectly ordered tilted polar smectic layer where θ, ϕ and ψ are the Euler angles. The layer normal $\hat{k}$ is parallel to the z-axis and the XY plane is the layer plane. The double-headed arrow represents the projection of the long axis on the layer plane. For a perfectly ordered layer, the director $\hat{n}$ and polar order $\vec{P}$ are parallel to $\hat{l}$ and $\hat{p}$ of the molecules respectively. The unit vector $\hat{\xi} = (\hat{k}\cdot\hat{l})(\hat{k}\times\hat{l})/|(\hat{k}\cdot\hat{l})(\hat{k}\times\hat{l})|$ represents the tilt direction of a molecule which is perpendicular to the ($\hat{l}$,$\hat{k}$) plane.

direction $\hat{p}$ of the molecules also align on average giving the polar order $\vec{P}$ in the the layer. The chirality of a layer arises depending on the mutual orientations of three directions namely the layer normal($\hat{k}$), the director ($\hat{n}$) and the polar order ($\vec{P}$). The chirality of a layer can be defined in terms of the sign of the vector triple product $(\hat{k}\cdot\hat{n})[(\hat{k}\times\hat{n})\cdot\vec{P}]$ consistent with the apolar nature of both the director and the layer normal. The chirality of a layer can then be quantified by $cos\psi = \hat{P}\cdot(\hat{k}\times\hat{n})/sin\theta$, where θ and ψ are the tilt angle and roll angle of the molecules in the layer respectively. The roll angle ψ defines the rotation of the tilted BC molecule about its long axis. When the roll angle ψ is equal to 0 or π, the polar axis $\hat{P}$, projection of $\hat{n}$ on the layer plane and layer normal are mutually orthogonal describing a right or left-handed coordinate system respectively. There is only a two-fold rotation axis parallel to the polar axis $\hat{P}$ with no mirror plane symmetry giving rise to the chiral C_2 point symmetry of a layer. When ψ is equal to $\pi/2$ or $3\pi/2$, the unit vectors $\hat{P}$, $\hat{n}$ and $\hat{k}$ all lie in the same plane which itself becomes a mirror plane symmetry of the layer. So, the layer has an achiral C_s point symmetry. For intermediate values of ψ, the layer has the lowest C_1 point symmetry giving rise to the most general chiral tilted polar smectic (SmCPG) order in a layer.

The most commonly observed tilted polar smectic (SmCP) phase of these BC molecules is the B_2 phase [3, 6–10]. In the B_2 phase, the roll angle ψ is equal to 0 or π and the layer is chiral with C_2 symmetry. The stacking of these chiral SmCP layers with synclinic or anticlinic tilt order and ferro or antiferro polar order between successive layers has been observed in the B_2 phase. Depending on the relative orientations of tilt and polar directions in successive layers, there are four possible configurations of B_2 phase with same free energy and all of them generally found to coexist in this phase. Recently, some colloidal systems have also been found to exhibit these kind of phases [11].

The possibility of most general smectic (SmCG) phase with C_i point symmetric of the layers was first predicted by de Gennes in the first edition of his classic book [1]. Brand *et al.* theoretically discussed properties and applications of the general SmCPG phase [12]. The experimental evidence of the existence of this general SmCPG phase has also been reported [13–18]. Assuming a simple triangular shape of the BC molecules, Bailey *et al.* calculated the excluded volume between the molecules and predicted undulated layer structure with local C_1 symmetry [19]. The smectic phase denoted as SmTP phase with C_s point symmetry of the layers has been reported experimentally [20, 21], where T denotes the ‘Tipping’ angle analogous to the ‘Leaning’ angle of the BC molecules in the layer.

To better understand the complex phase behaviour of BC molecules, a large number of studies using phenomenological theory, molecular theory, molecular dynamics and Monte-Carlo simulations have been performed [11, 22–28]. But few of these studies addressed or resolved the microscopic origin of chiral symmetry breaking in the layer. Roy *et al.* have shown using a phenomenological theory that BC molecules can exhibit layer structure with C_2, C_1 and C_s point symmetries depending upon phenomenological constants and discussed the stability of polar smectic A (SmAP) phase using uniaxial nematic interaction between the rodlike arms of the BC molecules [22]. But they did not consider the molecular interactions which could lead to tilted polar smectic phases. Xu *et al.* addressed the excluded volume effect as the possible reason for the origin of chiral behaviour in the bent-core molecular systems using Monte-Carlo simulation [24]. In their simulation, a BC molecule was made of seven spherical beads and the soft repulsive Weeks-Chandler-Andersen (WCA) interaction potential between two spherical beads of different molecules was used. They did not observe any tilted polar smectic phase but found chiral crystal phases. So, the role of excluded volume effect in the chiral symmetry breaking of a tilted polar smectic layer was not clear. Lansac *et al.* considered the BC molecule consisting of two connected sphero-cylinders and performed MC simulation taking hard body interaction between two BC molecules. But, they did not find any tilted smectic phase. Emelyanenko *et al.* have shown the stability of SmCP layer by considering steric, dispersion and dipole-dipole interactions between two molecules made of interconnected rigid rods [28]. They did not find C_1 symmetric SmCPG chiral layer. Yang *et al.* have shown the stability of SmCP phase using Brownian dynamics simulation. The molecular model and interaction potential employed in their simulation are similar to Xu *et al.* [24]. So, it is clear that the molecular origin of the spontaneous breaking of chiral symmetry has not been resolved.

We consider here the role of hard body interaction or excluded volume effects on the chiral symmetry breaking in a layer of the tilted polar smectic phase of BC molecules. We directly compute the excluded volume between two BC molecules in a tilted smectic layer and our approach is different from previous molecular dynamics and Monte Carlo simulation studies. It is well known that the excluded volume effect plays an important role in phase ordering and properties of soft matter systems such as van der Waals correction to Ideal gas law, Onsager's theory of nematic to isotropic transition [29]. Two types of models for the BC molecules are considered in our numerical calculation of excluded volume between two molecules in a layer. We show that the excluded volume effect favours the chiral symmetry breaking in the SmCP layer of BC molecules. We have also constructed a coupled XY-Ising model to describe the statistical origin of chiral symmetry breaking. Monte-Carlo simulation studies using our XY-Ising model were performed to find the possible phases with temperature as well as under applied electric field.

2.2 Model

For the computation of the excluded volume, we have considered two types of structural models for the BC molecules. In one model, hard spherical beads are joined together to form the BC molecule as shown in figure 2.2(a). The molecular parameters in this model are bending angle β, radius of the spherical beads R and the total number of beads N. In the other model, the BC molecule consists of two spherocylindrical arms of radius R and length $(N-1)R$ joined end to end with an angle β between their long axes as shown in figure 2.2(b).

The analytical calculation of excluded volume even for simple rodlike molecules is a formidable task. Onsager first derived an approximate analytical expression for the excluded volume between hard sphero-cylindrical rods in the limit of large length to diameter ratio of the rods. Based on these results, he accounted for the isotropic to nematic transition for this hard rod system at sufficiently high concentrations [29]. We have used numerical tools to compute the excluded volume of bent-core molecules

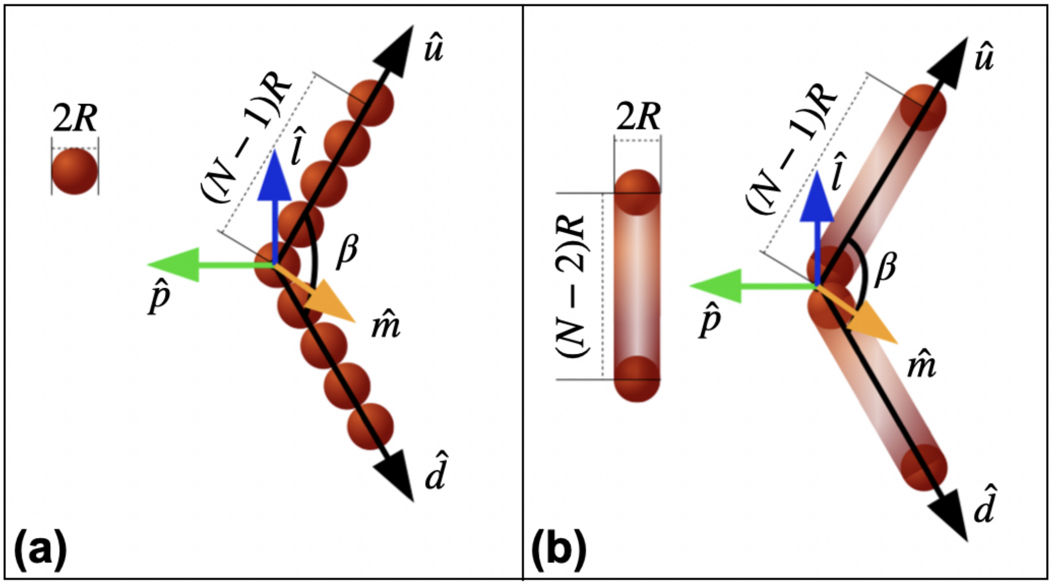

Figure 2.2: The model structures (a) bead model (b) hard sphero-cylinder (HSC) model of a BC molecule used in the computation of excluded volume. The unit vectors $\hat{l}, \hat{p}$ and $\hat{m}$ are body fixed axes. The unit vectors $\hat{u}$ and $\hat{d}$ represent the orientation of upper and lower arms respectively.

in a layer of their tilted polar smectic phase. To reduce the complexity of the problem, we assume that all molecules in a layer have their centers in the plane of the layer and also they have the same orientation. A molecular frame $(\hat{l}, \hat{p}, \hat{m})$ as shown in figure 2.2 can be used to specify the orientation of a BC molecule in a layer. Then the orientation of a BC molecule with respect to the layer frame coordinate system is represented by the Euler angles (tilt angle θ, azimuthal angle ϕ, roll angle ψ) [30] as shown in figure 2.1.

We compute the excluded volume between the molecules by finding the closest approach of a molecule around a fixed molecule in a layer. Consider two BC molecules with the bead type structure which are initially juxtaposed with each other in a layer with a given orientation. Now keeping one of the molecules fixed, the other molecule is moved on the layer plane in a particular direction with an azimuthal angle α without changing its orientation. At each position of the second molecule, the distance between each bead of one molecule is calculated with respect to the beads of the other molecule. The second molecule is moved in that direction until the minimum of these interbead distances exceeds $2R$. This position $\vec{r}_\alpha$ gives the vectorial distance of the closest approach of the second molecule with respect to the first molecule in that direction α. At this position, the coordinates of all the beads of the second molecule are stored for this particular value of α. Then by repeating the above procedure by varying α from 0 to 2π, a 3D excluded volume region around the fixed molecule can be constructed. This excluded volume region consists of two parts divided by the midplane of the layer.

The infinitesimal excluded area between the direction α and $\alpha + \delta\alpha$ is given by $\delta\vec{A}_{ex} = \frac{1}{2}\vec{r}_\alpha \times \vec{r}_{\alpha+\delta\alpha}$. The area vector direction is parallel to the layer normal or z-axis. Then the infinitesimal excluded volume of the upper half part between α and $\alpha + \delta\alpha$ is $\frac{N-1}{2}R(\hat{u} \cdot \vec{r}_\alpha \times \vec{r}_{\alpha+\delta\alpha})$ where the unit vector $\hat{u}$ denotes the orientation of the upper arms of the BC molecules in the layer. Similarly, the infinitesimal excluded volume of the lower half part is given by $\frac{N-1}{2}R(-\hat{d} \cdot \vec{r}_\alpha \times \vec{r}_{\alpha+\delta\alpha})$, where the unit vector $\hat{d}$ denotes the orientation of the lower arms of the BC molecules in the layer. So, the total infinitesimal excluded volume between the direction α and $\alpha + \delta\alpha$ is $\delta V_{ex} = \frac{N-1}{2}R(\hat{u} - \hat{d}) \cdot (\vec{r}_\alpha \times \vec{r}_{\alpha+\delta\alpha})$. The total excluded volume V_{ex} is obtained by integrating δV_{ex} over the angle α from 0 to 2π.

We numerically compute the excluded volume by discretizing α between 0 to 2π into M small intervals. Then summing over these discrete values of α, the total excluded volume can be written as

$$V_{ex} = 2(N-1)RA_{ex}\sin\frac{\beta}{2}\cos\theta,$$

where the magnitude of the total excluded area is given by

$$A_{ex} = \frac{1}{2}\sum_{i=1}^{M} |\vec{r}_i \times \vec{r}_{i+1}|$$

and $\vec{r}_i$ is the closest approach of the second molecule in the α_i-th direction. A dimensionless form of the excluded volume can be obtained by dividing the computed excluded volume by the volume $4\pi R^3/3$. Henceforth, this dimensionless excluded volume is denoted as V_{ex} in the rest of the chapter. The results presented in this thesis have been computed using $N = 9$. For other values of N, the excluded volume just scales with N without changing the conclusions.

Similarly, the excluded volume between two BC molecules with sphero-cylindrical arms can be calculated. The algorithms as discussed in the articles [31, 32] for finding the shortest distance between two straight rods are utilised to find the closest approach between two molecules. The consistency of our algorithm was checked by computing the excluded volume for $\beta = \pi$ which can be calculated analytically.

We have also computed the excluded volume for non-tilted molecules in the layer with $\theta = 0$. In this case, the azimuthal angle ϕ can be chosen arbitrarily as $\phi = 0$. We calculate the excluded volume between two molecules for different relative orientations of their polar directions $\hat{p}$. From the symmetry of the problem, the excluded volume depends only on the difference in the azimuthal angles $\delta\psi$ between the polar directions. Without any loss of generality, we fixed $\psi = 0$ for the first molecule and computed the excluded volume for different values of ψ of the second molecule between 0 to 2π using the algorithm discussed above.

The excluded volume between the molecules makes a purely entropic contribution to the free energy. The free energy density is proportional to the excluded volume as can be shown analytically for a dilute hard sphere system. So, the molecular configuration associated with the minimum V_{ex} is favoured energetically.

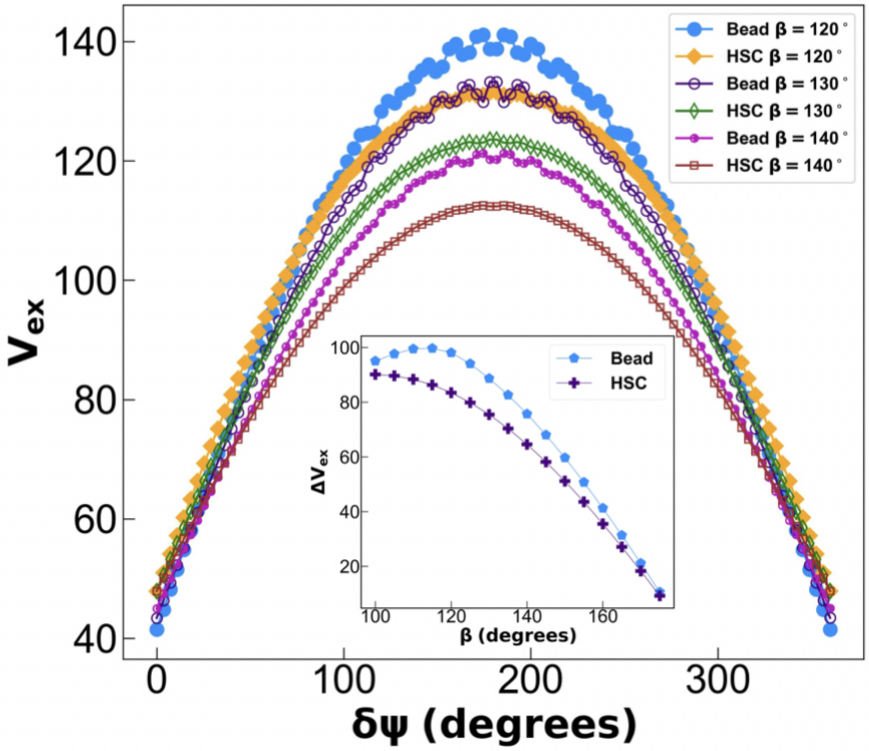

Figure 2.3: The variation of the excluded volume V_{ex} with the relative azimuthal angle $\delta\psi$ between two molecules for an orthogonal smectic layer. Inset shows the difference in V_{ex} corresponding to $\delta\psi = \pi$ and 0 for different values of β.

2.3 Results and Discussions

In the SmA and SmAP phase, the long axes of the BC molecules are on average parallel to the layer normal. In the SmA phase, the layers do not possess any polarisation whereas in the SmAP phase, the layers have an in-plane polar order. The excluded volume of two such non-tilted BC molecules in a smectic layer is computed for various relative orientations $\delta\psi$ between their bending directions as shown in figure 2.3. Excluded volume is minimum for $\delta\psi = 0^\circ$ or 360° and shows a symmetric maximum at 180° as expected from the packing considerations. The excluded volume interaction therefore tends to align the bending directions of the BC banana-shaped molecules in the non-tilted smectic layers giving rise to the polar SmAP order. This result is similar to that found assuming dispersion interaction between the BC molecules [28]. The inset of figure 2.3 depicts the variation of the excluded volume difference between the parallel and antiparallel configuration of the bending direction of the molecules as a function of the bending angle β. This excluded volume difference ΔV_{ex} can be associated with the free energy barrier between the parallel and antiparallel configuration of the bending direction of the molecules. Hence, it contributes to the stability of the SmA or SmAP phases. For nearly rodlike molecules with $\beta \sim 180^\circ$, the barrier height is quite low stabilising the SmA phase as expected. These results agree with the observation of SmAP and SmA phases for lower and higher bending angles respectively in the MC simulation of HSC model of the BC molecules [26]. The ΔV_{ex} is always higher for the bead model favouring the SmAP phase compared to the HSC model of the BC molecules.

In the tilted polar smectic phase, the long axes of the BC molecules in a layer are tilted with respect to the layer normal. The excluded volume between the molecules in a layer depends on the tilt angle θ, roll angle ψ and bending angle β of the molecules. The excluded volume as a function of ψ varies with a periodicity of π and

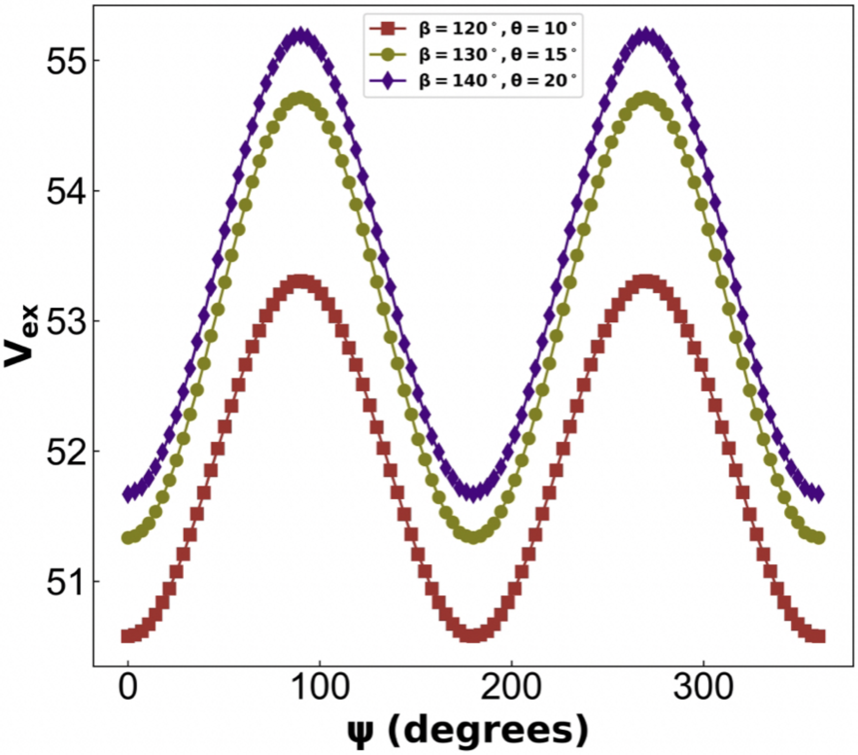

Figure 2.4: The variation of excluded volume V_{ex} as a function of roll angle ψ for the HSC model.

is symmetric about $\pi/2$ as expected from the symmetry of the system. Figure 2.4 shows the variation of excluded volume with ψ for different fixed values of θ and β assuming the HSC model structure of the BC molecules. The excluded volume is minimum at $\psi = 0$ and π indicating that it favours chiral symmetry breaking with the C_2 point symmetry of the layer. The profile of the excluded volume as a function of ψ remains qualitatively same for different values of θ and β. However, for bead model of the BC molecule, the variation of excluded volume with ψ strongly depends on θ and β of the molecules as shown in figure 2.5. The profile of excluded volume with ψ can be classified into four types based on the position of extrema at different values of ψ. In the first type, the excluded volume remains almost constant for different values of ψ as shown in plot-I. Hence, the layers with C_1, C_2 and C_s symmetries have the same excluded volume and are equally probable. This behaviour occurs for high and low values of β and θ of the BC molecules respectively. In the second

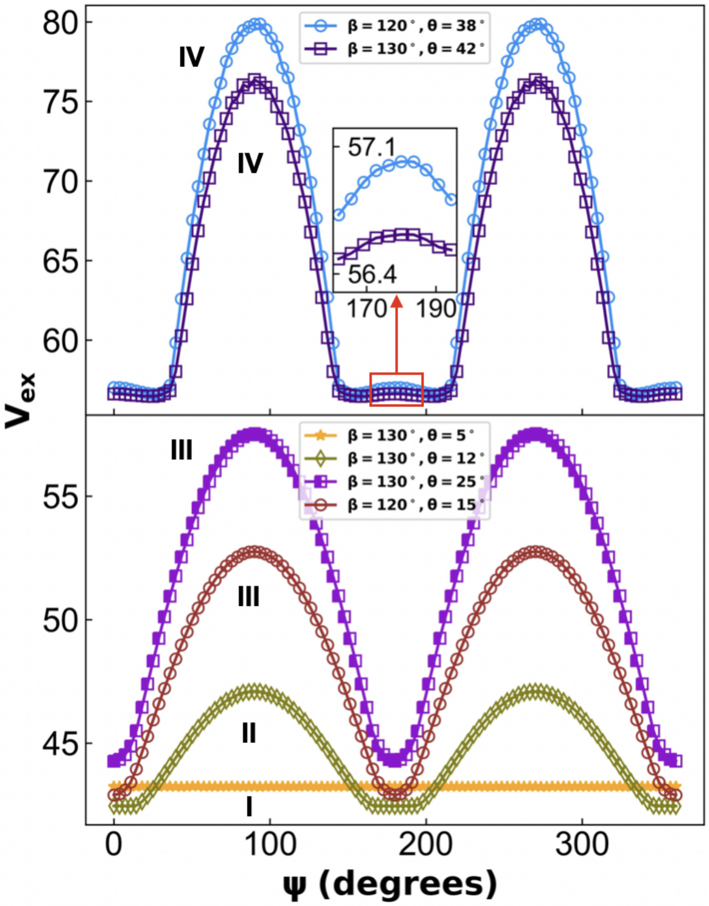

Figure 2.5: The variation of V_{ex} as a function of roll angle ψ for the bead model. Inset shows the magnified view of the indicated region demonstrating the maximum at $\psi = 180°$ for higher values of θ.

case (plot-II), the excluded volume has degenerate minima for a range of values of ψ about zero in addition to the maximum at $\psi = 90°$. The degenerate minima of the excluded volume favour both C_1 and C_2 symmetric layer structures with chiral symmetry breaking. This behaviour was found only for $\beta > 120°$ and moderate values of θ. In the third case (plot-III), the excluded volume is minimum only at $\psi = 0$ favouring the C_2 symmetric SmCP layer structure with spontaneous breaking of chiral symmetry. For the fourth type, the excluded volume has a minimum only at an intermediate value of ψ between 0 and $\pi/2$ as shown in plot-IV. It should be noted that the excluded volume is maximum at $\psi = 0$ and π in this case as shown in the inset of figure 2.5. Hence, the most general SmCPG layer structure with C_1 point

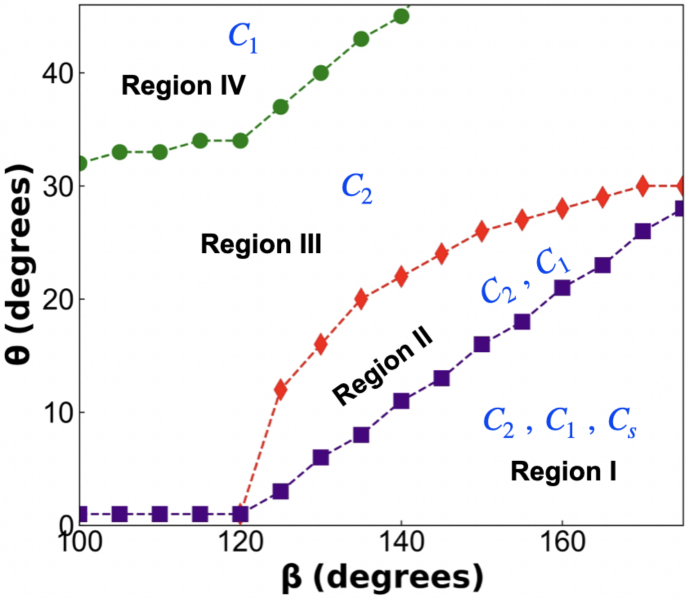

Figure 2.6: The stability diagram in the θ - β plane representing the regions of stability of the different symmetries of the layers obtained from the excluded volume interactions for bead model of the molecules.

symmetry is favoured. This case was found for large θ and values of β near 120° of the molecules. Based on these excluded volume analyses, a stability diagram in the the $\theta - \beta$ parameter plane for the different possible symmetries of the layer is constructed as shown in figure 2.6. The figure displays four separate regions corresponding to different possible symmetries of the layer. In region I, the C_1, C_2 and C_s symmetries of the layers are possible due to excluded volume interaction. In region II, C_1 and C_2 symmetries are favoured. In region III and region IV, only the C_2 and C_1 symmetries of the layer are found respectively. The layers can have C_s symmetry only in the region I with high values of bending angle and low values of tilt angle. Whereas, the layers with C_1 symmetry are possible in regions I, II and IV. However, the C_2 symmetric layer structure can be found for most values of β and θ studied in our model as shown in figure 2.6.

Therefore the excluded volume interaction for both HSC and bead models of the BC molecules predicts C_2 symmetric layer structure with chiral symmetry breaking as found in the B_2 phase experimentally. Depending on the tilt and bending angle, the bead model also predicts the possibility of the existence of the C_1 and C_s symmetric layer structures. As the excluded volume has equal minima both at $\psi = 0$ and π, the right and left handed structures are equally probable. This equality arises due to the achiral nature of the BC molecules.

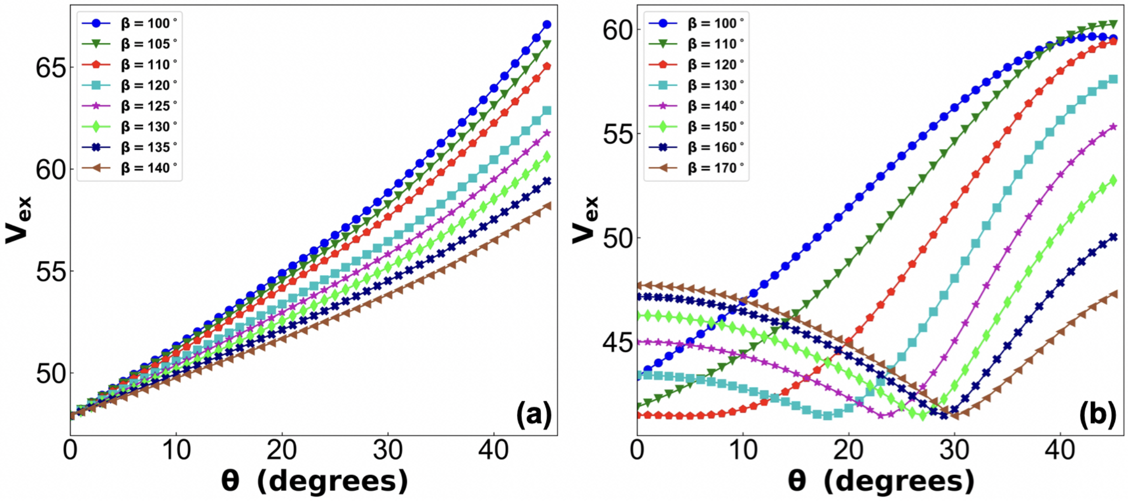

Figure 2.7: The variation of V_{ex} with tilt angle θ at $\psi = 0$ or π for (a) HSC model and (b) bead model of the molecules.

The variation of excluded volume with tilt angle θ for both HSC and bead model of the BC molecules is presented in figure 2.7 for a fixed value of $\psi = 0°$ and for different values of β. The excluded volume increases monotonically with θ for all values of β for the HSC model, as shown in figure 2.7(a). Hence, the excluded volume for SmAP layer corresponding to $\theta = 0°$ is always lower than that for the tilted polar smectic layer with $\theta \neq 0°$. Therefore, the SmAP phase is favoured compared to the SmCP phase for the HSC model of the BC molecules. This result is consistent with the observation of not finding any tilted smectic phase in the earlier Monte Carlo simulation study using the HSC model of the BC molecules [26]. The bead model displays different behaviour compared to the HSC model, as shown in figure 2.7(b). For the bead model, the minimum of V_{ex} with respect to θ strongly depends on the bending angle of the molecules. The excluded volume V_{ex} is minimum at $\theta = 0°$ for $\beta \leq 120°$ and the minimum shifts to non-zero value of θ for the higher bending angle.

So, the SmAP layer is always stable compared to the SmCP layer order for bending angle $\beta \leq 120°$. Whereas the excluded volume interaction favours the spontaneous tilt of the molecules in the layer for β greater than 120° giving rise to the chiral C_2 symmetry. This can perhaps explain the observation of tilted chiral crystal phases in the simulation results of BC molecules with $\beta = 140°$ in the article [24]. Our result also agrees well with the molecular dynamics simulation studies of BC molecules with $\beta > 130°$ [11].

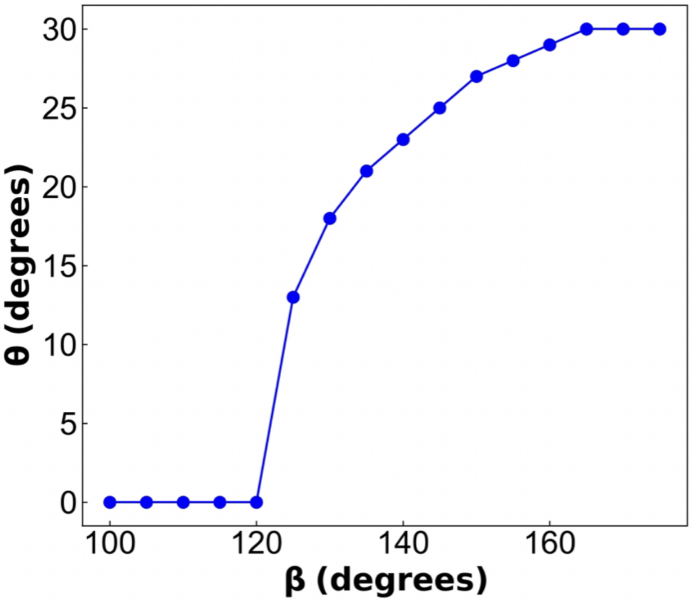

Figure 2.8: The favoured tilt angle θ for the bead model of the BC molecules at different values of bending angle β.

Figure 2.8 depicts the variation of the favoured tilt angle as a function of the bending angle obtained from the excluded volume interaction. This tilt angle increases from zero beyond $\beta = 120°$ and saturates to a value of 30° for nearly rodlike molecules with $\beta \sim 180°$. This tilting of the molecules in the layer arises due to the close packing arrangements of the beads in the rodlike molecules. Similar tilt angles were also found in earlier simulation studies of BC molecules using the bead model with the Lennard-Jones interaction potential between the molecules [27]. The favoured tilt angle is obtained on minimization of the excluded volume between two molecules in a layer, and it can be called the effective optimal molecular tilt for each pair of molecules [33]. However, the average tilt of molecules in a layer in their smectic phase can be obtained by statistical averaging with this excluded volume interaction.

2.4 Monte Carlo Simulation

Excluded volume effects discussed above clearly favour the chiral tilted polar smectic phase with C_2 point symmetry of the layers for both the bead and HSC model of the BC molecules. However, excluded volume effects describe the properties of an athermal system. We have, therefore, constructed a coupled XY-Ising model to describe the cooperative development of chiral order in a layer as a function of temperature and electric field. Similar types of XY-Ising models have been employed over the past to describe superconducting Josephson-junction arrays in a transverse magnetic field [34, 35]. These models have also been used to describe the ordered and disordered hexagonal columnar phases of discotic liquid crystals [36, 37]. To the best of our knowledge, there is no report of the coupled XY-Ising model describing the phase transition in bent-core liquid crystals.

In this model, we assume that the BC molecules in a layer are tilted with respect to the layer normal with a fixed tilt angle but with variable tilt directions. Hence, the tilt direction of each molecule can be specified by a unit vector $\hat{\xi}$ as shown in figure 2.1. The tilt direction $\hat{\xi}$ lies on the layer plane and can be considered as an XY spin. Armed with our excluded volume results, we assume that the roll angle ψ of a molecule can randomly take a value of either 0 or π. Thus, the bending direction $\hat{p}$ of a BC molecule can be parallel or anti-parallel to the tilt direction $\hat{\xi}$ giving $\hat{p} = \sigma\hat{\xi}$ where σ is an Ising spin variable taking value ± 1(see figure 2.9). Therefore, the Ising variable σ represents the chirality in the orientation of a BC molecule with respect to the layer.

We consider the orientational interaction potential between the molecules in a layer as $U_{ij} = -Jk_B(1 + A\sigma_i\sigma_j)(\hat{\xi}_i \cdot \hat{\xi}_j)$, where i, j denote the molecular indices and k_B is the Boltzmann constant. The first term favours a synclinic interaction between the molecules for the parameter $J > 0$, which has the dimension of temperature. We assume that this term gives the more dominant interaction between the molecules. The second term with the dimensionless coefficient A takes into account the synclinic homochiral or anticlinic recimic orientations between the molecules. From the geometry of the BC molecules, this term is expected to be lesser than the first term i.e. $A < 1$. The potential due to an externally applied electric field is assumed as $U_i(\vec{E}) = -Jk_B\sigma_i\hat{\xi}_i \cdot \vec{E}$ where $\vec{E}$ represents the effective electric field. Hence, the Hamiltonian of the system is defined as $H = \sum\limits_{<i,j>} U_{ij} + \sum\limits_{i} U_i$ where $<>$ denotes the sum over the nearest neighbour pairs of molecules.

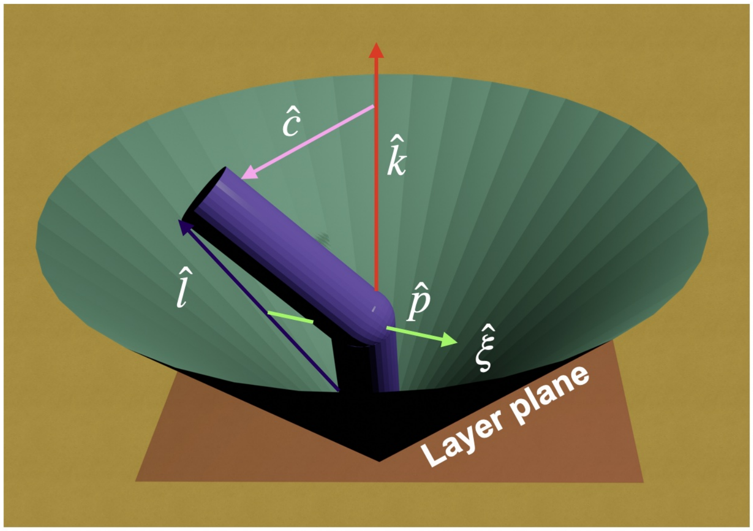

Figure 2.9: Schematic representation of the diffusive cone model describing the orientation of an achiral BC molecule in a de Vries SmA layer.

We carried out Monte Carlo (MC) simulations on a square lattice of dimension 40 × 40 with periodic boundary conditions. The XY and Ising variables are updated by the standard Metropolis algorithm. One of the following three update schemes is chosen randomly: (i) selection of a new random direction for the XY variable $\hat{\xi}$

without flipping the Ising spin σ, (ii) flipping of σ with unaffected $\hat{\xi}$, and (iii) selection of a new random direction for $\hat{\xi}$ and flipping of σ. Similar update schemes were also used in MC simulation for the kinetics study of the coupled XY-Ising model [38]. For simulation at each temperature or electric field, 10^6 MC cycles were run for equilibration and additional 10^6 MC steps were performed to compute the statistical quantities. The tilt, polar and chiral order parameters are defined as

$$\begin{aligned} \xi &= \frac{1}{L^2}\left\langle \left| \sum_i^{L\times L} \hat{\xi}_i \right| \right\rangle, \\ P &= \frac{1}{L^2}\left\langle \left| \sum_i^{L\times L} \hat{p}_i \right| \right\rangle, \text{ and } \sigma = \frac{1}{L^2}\left\langle \left| \sum_i^{L\times L} \sigma_i \right| \right\rangle \end{aligned}$$

respectively, where $\langle\ \rangle$ denotes the ensemble average and the sum runs over the total number of lattice points. The expression $C = \frac{\langle H^2\rangle - \langle H\rangle^2}{L^2 k_B^2 T^2}$ was used for the calculation of the dimensionless specific heat per molecule where T is the absolute temperature. To study the equilibrium phases as a function of temperature, the simulation was started at a high temperature with an initial isotropic configuration. The initial temperature was chosen such that the system remains in its equilibrium isotropic state. In this isotropic configuration, each molecule is tilted in the layer but their tilt and polar

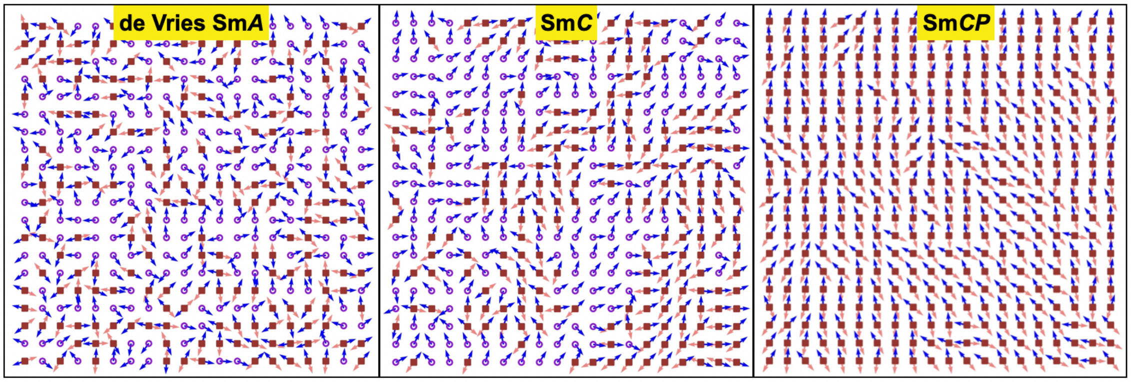

Figure 2.10: The representative spin configurations corresponding to the different phases. The blue and red (light gray) arrows denote the orientations of the unit vectors $\hat{\xi}$ and $\hat{p}$ respectively. The open circle and filled square symbols represent $+1$ and -1 values of the Ising spin, respectively.

directions are randomly oriented as shown in the leftmost configuration in figure 2.10. This configuration represents an achiral uniaxial smectic layer with no polar order. Therefore, the long axes of the molecules are distributed on the surface of a cone giving rise to the de Vries SmA layer structure with the proposed diffused cone model [39] (see figure 2.9). The system was equilibrated at each temperature and the stable phase sequence was determined with decreasing temperature. The final equilibrated state of the system at a given temperature was chosen as the initial configuration for the MC simulation at the next lower temperature. The same procedure was adopted for studying the equilibrium phase sequence with increasing electric field.

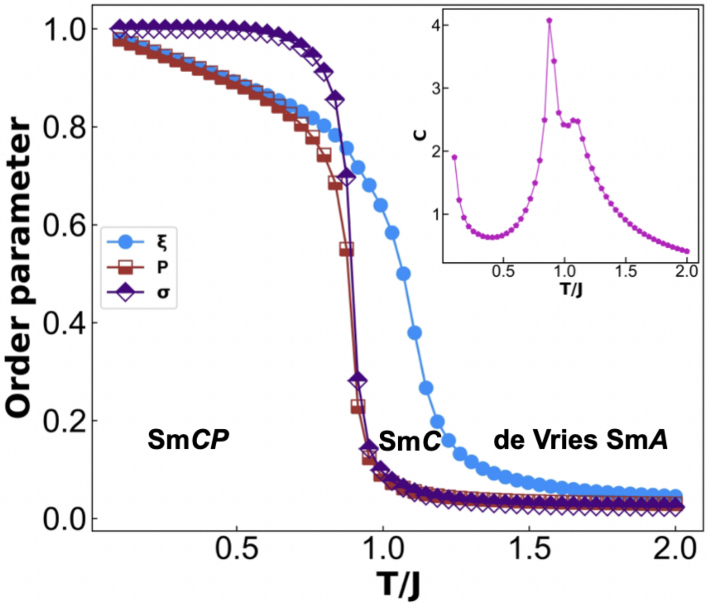

Figure 2.11: The variation of order parameters with temperature for $A = 0.5$ at zero electric field. Inset shows the corresponding specific heat variation.

The equilibrium values of the order parameters as a function of temperature are shown in figure 2.11 for the model parameter $A = 0.5$. The tilt order parameter ξ of the system increases significantly from zero with decreasing temperature below about $T/J \sim 1.25$ while the other order parameters P and σ remain zero till about $T/J \sim 1.0$. Therefore, the system in this temperature range exhibits the non-polar SmC structure. A typical configuration of the spins in the SmC structure is shown in figure 2.10. A small peak in the specific heat corresponds to this transition is also shown in the inset of figure 2.11. However, the ordering of the XY spins is expected to be quasi-long range in two dimensions according to Mermin-Wagner theorem [40] and the transition is of Kosterlitz-Thouless type [41]. Finite-size scaling analysis is required to accurately determine the transition temperature. On further cooling below about $T/J \sim 1.0$, the order parameters P and σ also become nonzero giving rise to a chiral tilted polar SmCP structure. A representative spin configuration in the SmCP structure is shown in figure 2.10. The larger peak in the specific heat, as shown in the inset of figure 2.11 indicates this transition. Similar transitions are also speculated in the earlier studies on superconducting systems [34, 35]. The chiral order parameter σ reaches the saturation value rapidly compared to the other order parameters across this transition. This is perhaps due to two possible states for the

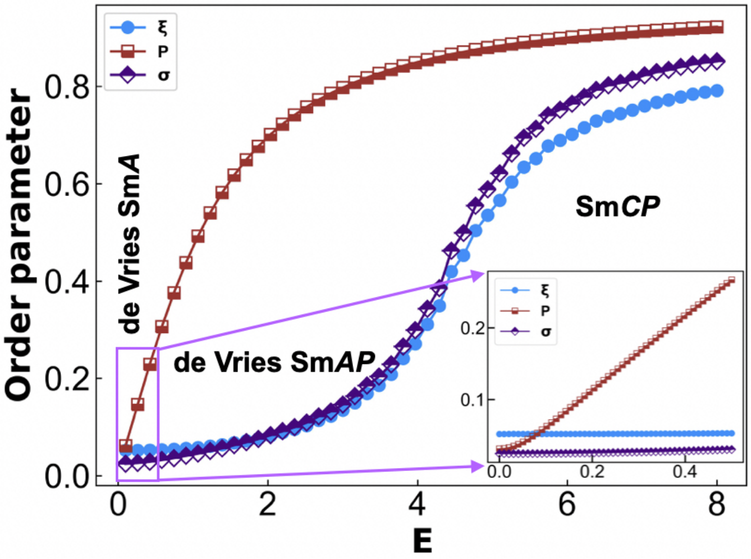

Figure 2.12: The variation of order parameters with electric field for $T/J = 1.8$ and $A = 0.5$. Inset shows the magnified view of the region at low field.

Ising spin compared to the continuum of states for the XY spin. The number of states of a spin variable increases the disorderedness in the system and it is reflected in the variation of order parameters with temperature. This type of phase sequence has been observed experimentally in bent-core liquid crystals [42].

Figure 2.12 displays the variation of order parameters with the electric field at a fixed temperature $T/J = 1.8$ corresponding to the de Vries SmA state. All the order parameters are zero at the low field region, as expected in the de Vries SmA layer structure. Above a certain threshold field, the polar order P in the layer increases monotonically with the electric field, whereas the other order parameters ξ and σ remain close to zero. Hence, the layer goes into the de Vries SmAP phase. In this phase, the bending direction $\hat{p}$ of the molecules align on average along the field but the tilt direction $\hat{\xi}$ is equally likely oriented parallel or antiparallel to $\hat{p}$. Thus, the long axes of the tilted molecules have a bimodal distribution around the diffused cone, giving rise to an achiral biaxial polar layer structure. Above a higher threshold field, all the order parameters become non-zero and the chiral SmCP layer structure is stabilized. Therefore, the layer exhibits spontaneous breaking of chiral symmetry. The electric field-induced breaking of chiral symmetry in bent-core liquid crystals has been reported [43].

Table 2.1: The observed phase sequences for different values of A.

A	Phase sequences during cooling
0.0	de Vries SmA $(\{\xi, P, \sigma\} = 0) \rightarrow$ SmC $(\{P, \sigma\} = 0, \xi \neq 0)$
0.5	de Vries SmA $(\{\xi, P, \sigma\} = 0) \rightarrow$ SmC $(\{P, \sigma\} = 0, \xi \neq 0) \rightarrow$ SmCP $(\{\xi, P, \sigma\} \neq 0)$
1.0	de Vries SmA $(\{\xi, P, \sigma\} = 0) \rightarrow$ SmCP $(\{\xi, P, \sigma\} \neq 0)$

The possible sequences of phases for different values of the model parameter A are given in table 2.1. For $A = 0$, there is no chiral or polar interaction between the molecules and only de Vries SmA and achiral SmC structures can be stabilized. For intermediate values of A, the de Vries SmA, SmC, and chiral SmCP structures are stable as discussed above. The tilt and polar interactions being comparable for $A = 1$, the de Vries SmA directly going to the chiral SmCP structure is favoured.

2.5 Summary

We have computed the excluded volume between bent-core molecules in a layer of their smectic phases. Two molecular models, namely the sphero-cylinder and bead model of the bent-core molecules were used in the computation of the excluded volume. The excluded volume results for both models of the BC molecules predict chiral symmetry breaking in their tilted smectic phase. This is the first report on the numerical studies of excluded volume between BC banana-shaped molecules in a layer of their smectic phase, which accounts for the experimentally observed chiral symmetry breaking. Depending on the tilt and bending angle of the molecules, the bead model predicts the possibility of C_2, C_s and C_1 point symmetries of the layers. We have also developed a coupled XY-Ising model based on the excluded volume results to investigate the layer structure using Monte Carlo simulations as a function of temperature and electric field. The model predicts different types of phase sequences depending on the interaction parameter and also accounts for electric field-induced chiral symmetry breaking.

Bibliography

[1] P. G. de Gennes and J. Prost, *The Physics of Liquid Crystals* (Clarendon Press, Oxford, 1995).

[2] V. Borshch, Y. K. Kim, J. Xiang, M. Gao, A. Jákli, V. P. Panov, J. K. Vij, C. T. Imrie, M. G. Tamba, G. H. Mehl, et al., Nature Communications **4**, 2635 (2013), URL `https://doi.org/10.1038/ncomms3635`.

[3] H. Takezoe and Y. Takanishi, Japanese Journal of Applied Physics **45**, 597 (2006), URL `https://doi.org/10.1143%2Fjjap.45.597`.

[4] R. A. Reddy and C. Tschierske, J. Mater. Chem. **16**, 907 (2006), URL `http://dx.doi.org/10.1039/B504400F`.

[5] A. Eremin and A. Jákli, Soft Matter **9**, 615 (2013), URL `http://dx.doi.org/10.1039/C2SM26780B`.

[6] T. Niori, T. Sekine, J. Watanabe, T. Furukawa, and H. Takezoe, J. Mater. Chem. **6**, 1231 (1996), URL `http://dx.doi.org/10.1039/JM9960601231`.

[7] D. R. Link, G. Natale, R. Shao, J. E. Maclennan, N. A. Clark, E. Körblova, and D. M. Walba, Science **278**, 1924 (1997), ISSN 0036-8075, `https://science.sciencemag.org/content/278/5345/1924.full.pdf`, URL `https://science.sciencemag.org/content/278/5345/1924`.

[8] G. Heppke and D. Moro, Science **279**, 1872 (1998), ISSN 0036-8075, `https://science.sciencemag.org/content/279/5358/1872`, URL `https://science.sciencemag.org/content/279/5358/1872`.

[9] D. M. Walba, E. Körblova, R. Shao, J. E. Maclennan, D. R. Link, M. A. Glaser, and N. A. Clark, Science **288**, 2181 (2000), ISSN 0036-8075, `https://science.sciencemag.org/content/288/5474/2181.full.pdf`, URL `https://science.sciencemag.org/content/288/5474/2181`.

[10] S. Rauch, P. Bault, H. Sawade, G. Heppke, G. G. Nair, and A. Jákli, Phys. Rev. E **66**, 021706 (2002), URL `https://link.aps.org/doi/10.1103/PhysRevE.66.021706`.

[11] Y. Yang, H. Pei, G. Chen, K. T. Webb, L. J. Martinez-Miranda, I. K. Lloyd, Z. Lu, K. Liu, and Z. Nie, Science Advances **4**, eaas8829 (2018), `https://www.science.org/doi/pdf/10.1126/sciadv.aas8829`, URL `https://www.science.org/doi/abs/10.1126/sciadv.aas8829`.

[12] H. R. Brand, P. E. Cladis, and H. Pleiner, The European Physical Journal B - Condensed Matter and Complex Systems **6**, 347 (1998), URL `https://doi.org/10.1007/s100510050560`.

[13] A. Jákli, D. Krüerke, H. Sawade, and G. Heppke, Phys. Rev. Lett. **86**, 5715 (2001), URL `https://link.aps.org/doi/10.1103/PhysRevLett.86.5715`.

[14] N. Chattham, E. Korblova, R. Shao, D. M. Walba, J. E. Maclennan, and N. A. Clark, Liquid Crystals **36**, 1309 (2009), `https://doi.org/10.1080/02678290903306458`, URL `https://doi.org/10.1080/02678290903306458`.

[15] N. Chattham, E. Korblova, R. Shao, D. M. Walba, J. E. Maclennan, and N. A. Clark, Phys. Rev. Lett. **104**, 067801 (2010), URL `https://link.aps.org/doi/10.1103/PhysRevLett.104.067801`.

[16] J. P. Bedel, J. C. Rouillon, J. P. Marcerou, H. T. Nguyen, and M. F. Achard, Phys. Rev. E **69**, 061702 (2004), URL `https://link.aps.org/doi/10.1103/PhysRevE.69.061702`.

[17] E. Gorecka, D. Pociecha, N. Vaupotič, M. Čepič, K. Gomola, and J. Mieczkowski, J. Mater. Chem. **18**, 3044 (2008), URL `http://dx.doi.org/10.1039/B803567A`.

[18] A. Eremin, S. Diele, G. Pelzl, H. Nádasi, and W. Weissflog, Phys. Rev. E **67**, 021702 (2003), URL `https://link.aps.org/doi/10.1103/PhysRevE.67.021702`.

[19] C. Bailey and A. Jákli, Phys. Rev. Lett. **99**, 207801 (2007), URL `https://link.aps.org/doi/10.1103/PhysRevLett.99.207801`.

[20] C. Zhang, N. Diorio, S. Radhika, B. Sadashiva, S. N. Sprunt, and A. Jákli, Liquid

Crystals **39**, 1149 (2012), `https://doi.org/10.1080/02678292.2012.704410`, URL `https://doi.org/10.1080/02678292.2012.704410`.

[21] N. Chattham, M.-G. Tamba, R. Stannarius, E. Westphal, H. Gallardo, M. Prehm, C. Tschierske, H. Takezoe, and A. Eremin, Phys. Rev. E **91**, 030502 (2015), URL `https://link.aps.org/doi/10.1103/PhysRevE.91.030502`.

[22] A. Roy, N. V. Madhusudana, P. Tolédano, and A. M. Figueiredo Neto, Phys. Rev. Lett. **82**, 1466 (1999), URL `https://link.aps.org/doi/10.1103/PhysRevLett.82.1466`.

[23] P. J. Camp, M. P. Allen, and A. J. Masters, The Journal of Chemical Physics **111**, 9871 (1999), `https://doi.org/10.1063/1.480324`, URL `https://doi.org/10.1063/1.480324`.

[24] J. Xu, R. L. B. Selinger, J. V. Selinger, and R. Shashidhar, The Journal of Chemical Physics **115**, 4333 (2001), `https://doi.org/10.1063/1.1389857`, URL `https://doi.org/10.1063/1.1389857`.

[25] R. Memmer, Liquid Crystals **29**, 483 (2002), `https://doi.org/10.1080/02678290110104586`, URL `https://doi.org/10.1080/02678290110104586`.

[26] Y. Lansac, P. K. Maiti, N. A. Clark, and M. A. Glaser, Phys. Rev. E **67**, 011703 (2003), URL `https://link.aps.org/doi/10.1103/PhysRevE.67.011703`.

[27] A. Dewar and P. J. Camp, Phys. Rev. E **70**, 011704 (2004), URL `https://link.aps.org/doi/10.1103/PhysRevE.70.011704`.

[28] A. V. Emelyanenko and M. A. Osipov, Phys. Rev. E **70**, 021704 (2004), URL `https://link.aps.org/doi/10.1103/PhysRevE.70.021704`.

[29] L. Onsager, Annals of the New York Academy of Sciences **51**, 627 (1949), `https://nyaspubs.onlinelibrary.wiley.com/doi/pdf/10.1111/`

j.1749-6632.1949.tb27296.x, URL https://nyaspubs.onlinelibrary.wiley.com/doi/abs/10.1111/j.1749-6632.1949.tb27296.x.

[30] H. Goldstein, C. Poole, and J. Safko, *Classical Mechanics* (Addison-Wesley, Boston, 2001).

[31] C. Vega and S. Lago, Comput. Chem. **18**, 55 (1994), ISSN 0097-8485, URL https://www.sciencedirect.com/science/article/pii/0097848594800235.

[32] V. J. Lumelsky, Information Processing Letters **21**, 55 (1985), ISSN 0020-0190, URL https://www.sciencedirect.com/science/article/pii/0020019085900328.

[33] A. V. Emelyanenko and A. R. Khokhlov, The Journal of Chemical Physics **142** (2015), ISSN 0021-9606, 204905, https://pubs.aip.org/aip/jcp/article-pdf/doi/10.1063/1.4921684/15496366/204905_1_online.pdf, URL https://doi.org/10.1063/1.4921684.

[34] E. Granato, J. M. Kosterlitz, J. Lee, and M. P. Nightingale, Phys. Rev. Lett. **66**, 1090 (1991), URL https://link.aps.org/doi/10.1103/PhysRevLett.66.1090.

[35] J. Lee, E. Granato, and J. M. Kosterlitz, Phys. Rev. B **44**, 4819 (1991), URL https://link.aps.org/doi/10.1103/PhysRevB.44.4819.

[36] M. Hébert and A. Caillé, Phys. Rev. E **51**, R1651 (1995), URL https://link.aps.org/doi/10.1103/PhysRevE.51.R1651.

[37] M. Hébert and M. L. Plumer, Phys. Rev. E **54**, 550 (1996), URL https://link.aps.org/doi/10.1103/PhysRevE.54.550.

[38] J.-R. Lee, S. J. Lee, B. Kim, and I. Chang, Phys. Rev. E **54**, 3257 (1996), URL `https://link.aps.org/doi/10.1103/PhysRevE.54.3257`.

[39] A. de Vries, The Journal of Chemical Physics **71**, 25 (2008), ISSN 0021-9606, `https://pubs.aip.org/aip/jcp/article-pdf/71/1/25/15355965/25_1_online.pdf`, URL `https://doi.org/10.1063/1.438123`.

[40] N. D. Mermin and H. Wagner, Phys. Rev. Lett. **17**, 1133 (1966), URL `https://link.aps.org/doi/10.1103/PhysRevLett.17.1133`.

[41] J. M. Kosterlitz, Journal of Physics C: Solid State Physics **7**, 1046 (1974), URL `https://dx.doi.org/10.1088/0022-3719/7/6/005`.

[42] A. Eremin, H. Nádasi, G. Pelzl, S. Diele, H. Kresse, W. Weissflog, and S. Grande, Phys. Chem. Chem. Phys. **6**, 1290 (2004), URL `http://dx.doi.org/10.1039/B312586F`.

[43] A. A. S. Green, M. R. Tuchband, R. Shao, Y. Shen, R. Visvanathan, A. E. Duncan, A. Lehmann, C. Tschierske, E. D. Carlson, E. Guzman, et al., Phys. Rev. Lett. **122**, 107801 (2019), URL `https://link.aps.org/doi/10.1103/PhysRevLett.122.107801`.

Chapter 3

A phenomenological theory for the SmA – de Vries SmA – SmC phase transition

---

Recently, in our lab, a compound consisting of bent-core hockey stick-shaped molecules has been found to exhibit the following phase sequence: smectic A–de Vries smectic A– smectic C. The smectic A phase undergoes a weakly first-order phase transition to the de Vries smectic A (dSmA) phase on cooling, which in turn undergoes a second-order transition to the SmC phase on further cooling. The observation of such SmA to dSmA phase transition has not been reported earlier. Here, we present a theoretical model to account for the observed phase sequence in our sample. We compute a phase diagram showing the stability regions of these phases depending on the model parameters. Theoretical results agree reasonably well with experimental findings, implying the general validity of our model.

3.1 Introduction

Liquid crystals are known to exhibit emergent physical properties with various types of complex self-assembled structures of their constituent molecules. Despite a large number of observed phases, exploring the new phases and their properties is an active field of research. In the smectic A (SmA) phase, the rod-like molecules arrange themselves in stacks of liquid-like layers where the long axes of the molecules are, on average, parallel to the layer normal, giving the layer spacing same as the molecular length. The average orientation of the molecular long axes is defined as the director $\hat{n}$. In the smectic C (SmC) phase, the director $\hat{n}$ tilts uniformly with respect to the layer normal. The transition from the SmA to SmC has been observed on cooling for some compounds consisting of rod-like molecules. The tilt of the director $\hat{n}$ in the SmC phase reduces the layer spacing as $d_C = d_A cos\theta$ where d_C and d_A are the layer spacing in the SmC and SmA phases, respectively, and θ is the tilt angle. The layer spacing usually decreases significantly with decreasing temperature across this transition due to the temperature variation of the tilt angle. For planar-aligned systems, the large shrinkage in the layer spacing leads to the creation of so-called chevron defects [1], which enhance the contrast problem in the display that restricts the commercialization of such smectic liquid crystals.

However, it has been observed that there is no significant change in the layer spacing over the full temperature range of SmA and SmC phases for some compounds. For the first time, this was reported by Diele *et al.* [2]. Subsequently, in 1977, de Vries reported that the layer spacing does not change significantly across the A-C transition for a compound TBBA [3]. To account for these observations, he proposed that the long axes of the molecules are already tilted with respect to the layer normal in the SmA phase itself, but the tilt directions of the molecules are randomly oriented in the layer plane, giving rise to the uniaxial configuration about the layer normal. This

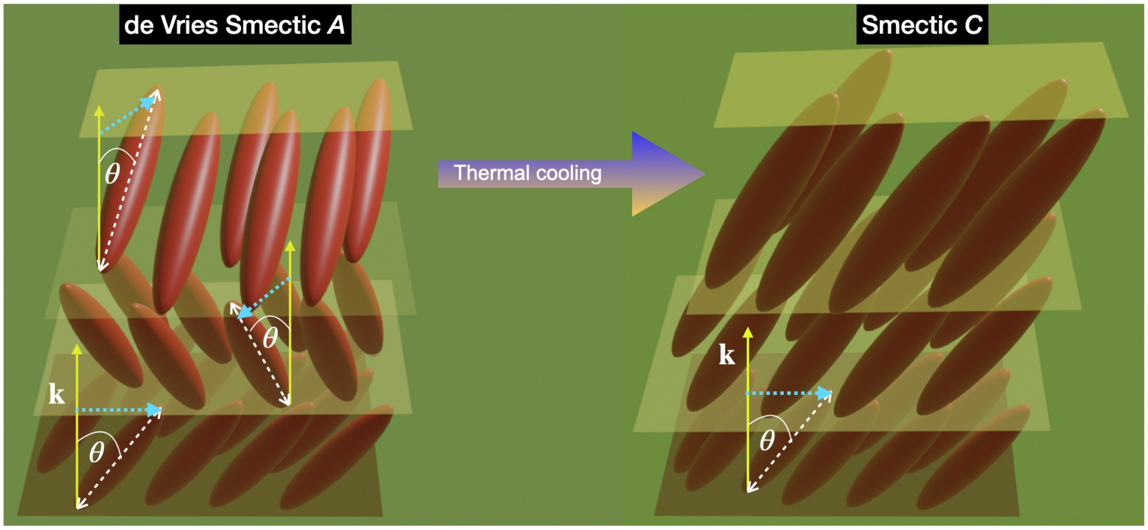

Figure 3.1: Schematic representation of the non-correlated layer model for the de Vries SmA to SmC phase transition.

proposed molecular organization in the smectic A phase can be easily visualized by two types of models: (i) non-correlated layer [3] and (ii) diffusive cone model [4]. The schematic representation of these two types of models are shown in figure 3.1 and 3.2, respectively. The SmA phase with such types of molecular organization is now known as the de Vries smectic A (dSmA) phase. In the first model, the molecules in each layer are, on average, tilted uniformly along a preferred direction, but the tilt direction varies randomly from layer to layer due to the weak interlayer interactions, giving the uniaxial symmetry about the layer normal. In the second model, the molecules in each layer have a preferred tilt angle, but the direction of molecular tilt (i.e., the orientation of the projection of the long axis on the layer plane) varies randomly. These random tilt directions give the uniaxial symmetry to the layer. Thus, the long axes of the molecules in this diffusive cone model are preferentially distributed uniformly on the surface of a cone. Across the transition from the dSmA to SmC phase upon cooling, all the pre-tilted molecules in the layers select a preferred tilt direction without any change in the layer spacing. The compounds that show more or less the same layer spacing across the A-C transition are commonly known as de

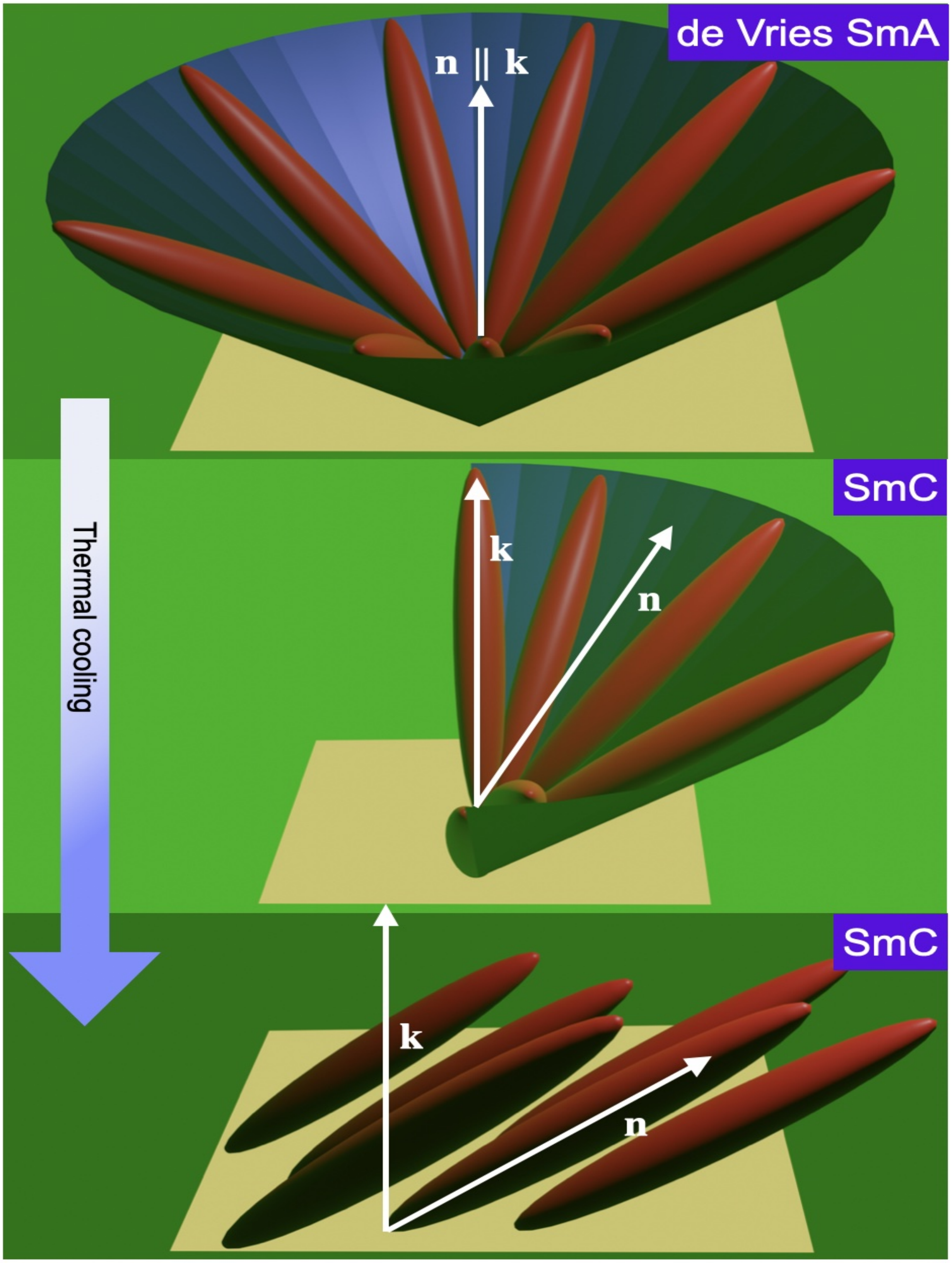
de Vries SmA
n || k
Thermal cooling
SmC
k
n
SmC
k
n

Figure 3.2: Schematic representation of the diffusive cone model for the de Vries SmA to SmC phase transition.

Vries materials.

A large number of experimental studies have been conducted to understand the properties of these materials, including both calamatic and symmetric bent-core liquid crystals [5–10]. Most of the de Vries materials studied so far exhibit the de Vries SmA phase at higher temperatures, which often undergoes a transition to the SmC phase on lowering the temperature [11–16]. A large number of theoretical studies involving molecular mean-field theory [17–19], simulation [20] and phenomenological theory [21] have been performed to account for the transition from the dSmA to SmC phase. However, there is no report of a liquid crystal exhibiting SmA phase, dSmA phase and SmC phase on cooling it from its isotropic phase. For the first time, we find a de Vries-type liquid crystal consisting of bent-core hockey stick-shaped (BCHS) molecules that exhibit the SmA phase, dSmA phase, and SmC phase sequence on cooling. The theoretical models cited above are not suitable for the description of phase transitions observed in our system. Therefore, we have constructed a phenomenological theory to describe these phases and the transitions among them. To the best of our knowledge, this is the first report of a phenomenological theory accounting for these phase transitions.

3.1.1 Theoretical Model

We now develop a theoretical model to account for the observed transitions between the SmA, de Vries SmA, and SmC phases of the sample. In our model, we start from the high-temperature SmA as the high-symmetry phase and define two order parameters to describe the observed phase transitions on decreasing temperature. Assuming without loss of generality, the layer normal in the SmA phase is along the z-axis, the orientational order of the long axes of the molecules in the smectic layers can be defined by a traceless, symmetric second-rank tensor $Q_{ij} = \langle l_i l_j - \delta_{ij}/3 \rangle$ where the unit vector $\hat{l} = (\sin\theta\cos\phi, \sin\theta\sin\phi, \cos\theta)$ denotes the orientation of a molecular long axis, and the angular bracket is for the ensemble averaging. The angles (θ, ϕ) denote the polar and azimuthal angle made by $\hat{l}$ with respect to the layer normal and an arbitrarily chosen x-axis in the plane of the smectic layer, respectively. In this coordinate frame, the most general orientational order parameter can be written as

$$Q_{ij} = \begin{bmatrix} -S/2 + \eta\cos 2\sigma & \eta\sin 2\sigma & \tau\cos\sigma \\ \eta\sin 2\sigma & -S/2 - \eta\cos 2\sigma & \tau\sin\sigma \\ \tau\cos\sigma & \tau\sin\sigma & S \end{bmatrix} \tag{3.1}$$

Where S, η and τ are the three scaler order parameters corresponding to uniaxial, biaxial and tilt order of the molecules in the layer, respectively, and σ is the azimuthal angle of the director on the layer plane. These order parameters are defined by the relations $S = \langle\cos^2\theta - 1/3\rangle$, $\eta\cos 2\sigma = \langle\sin^2\theta\cos 2\phi\rangle/2$, $\eta\sin 2\sigma = \langle\sin^2\theta\sin 2\phi\rangle/2$, $\tau\cos\sigma = \langle\sin 2\theta\cos\phi\rangle/2$ and $\tau\sin\sigma = \langle\sin 2\theta\sin\phi\rangle/2$. In the SmA phase, only the uniaxial order parameter is non-zero at $S = S_0$, and the biaxial order parameter η and tilt order parameters τ are zero. Hence, the orientational tensor order parameter Q_{ij} in the SmA phase becomes

$$Q^0_{ij} = \begin{bmatrix} -S_0/2 & 0 & 0 \\ 0 & -S_0/2 & 0 \\ 0 & 0 & S_0 \end{bmatrix} \tag{3.2}$$

We consider the deviation $\delta Q_{ij} = Q_{ij} - Q^0_{ij}$ of the orientational order from the SmA phase as the first order parameter in our theory. The order parameter δQ_{ij} is zero in the SmA phase and becomes non-zero in the lower temperature de Vries SmA and SmC phases.

In addition, the layer spacing decreases across the transition from the SmA phase to the de Vries SmA phase on cooling the sample. The compression along the layer normal is given by $u = (d_A - d)/d_A$, where d and d_A are the layer spacing in the de

Vries SmA and SmA phase respectively. To take into account this layer compression, we define the uniaxial strain tensor

$$U_{ij} = \begin{bmatrix} -u/2 & 0 & 0 \\ 0 & -u/2 & 0 \\ 0 & 0 & u \end{bmatrix} \tag{3.3}$$

as the second-order parameter in our theoretical model. The non-zero trace of the strain tensor U_{ij} corresponds to volume compression, which gives rise to change the density of a material. Since the change of density across the transitions between the observed smectic phases is usually very small, U_{ij} is assumed to be traceless in our model. The high-temperature SmA phase is characterized by the vanishing of all order parameters ($\zeta = u = \tau = \eta = 0$), where $\zeta = S - S_0$ is the change in the uniaxial order parameter S from the SmA value S_0. In the de Vries SmA phase, $\zeta \neq 0$, $u \neq 0$, and $\tau = \eta = 0$. In the SmC phase, all the four order parameters are non-zero.

We now expand the free energy density of the system in terms of these order parameters consistent with the symmetry $D_{\infty h}$ of the SmA phase. The lowest order invariants corresponding to these order parameters are $I_1 = \zeta$, $I_2 = u$, $I_3 = \tau^2$, $I_4 = \eta^2$, and their combinations are also symmetry invariant terms. Therefore, the homogeneous part of the free energy density of the system can be expanded using these invariants. The terms linear in ζ or u can not occur due to the stability of the SmA phase. The homogeneous part of the free energy density up to fourth power terms in these order parameters can then be written as

$$f_h(\zeta, u, \tau, \eta) = f(\zeta) + f(u) + f(\tau) + f(\eta) + f_c \tag{3.4}$$

where

$$\begin{aligned} f(\zeta) &= \frac{\chi}{2}\zeta^2 && (3.5)\\ f(u) &= \frac{\alpha}{2}u^2 - \frac{\beta}{3}u^3 + \frac{\gamma}{4}u^4 && (3.6)\\ f(\tau) &= \frac{A}{2}\tau^2 + \frac{B}{4}\tau^4 && (3.7)\\ f(\eta) &= \frac{C}{2}\eta^2 && (3.8)\\ f_c &= \lambda_1 u\zeta - \lambda_2 u\tau^2 + \lambda_3 u^2\tau^2 + \lambda_4 \zeta\tau^2 \\ & \quad -\lambda_5\zeta^2\tau^2 + \lambda_6 u\zeta\tau^2 - \mu_1\eta\tau^2. && (3.9) \end{aligned}$$

The first four terms on the RHS of equation 3.4 represent the free energy contribution due to the individual order parameters alone and the last term takes into account the free energy arising from the coupling between them. As the uniaxial orientational order parameter ζ is not critical across the transitions in our system; we consider only the quadratic term with the coefficient $\chi > 0$ and neglect the higher order terms of it. The expression in equation 3.6 is the free energy density up to quartic order in the uniaxial compression u. The positive and negative values of u correspond to contraction and expansion in the layer thickness, respectively and they constitute different states of the system. Therefore, the odd power terms in u are allowed in the free energy expansion. The free energy $f(u)$ can therefore accounts for a first-order transition from a phase($u = 0$) to a phase ($u \neq 0$) when the coefficient $\beta \neq 0$. The free energy associated with the tilt order is given by equation 3.7, which contains only even powers of τ as τ and $-\tau$ correspond to energetically equivalent states of the system. The biaxiality order parameter η is also assumed to be a non-critical order parameter in our model, and we retain only the lowest order quadratic term with the coefficient $C > 0$ in equation 3.8.

We now consider the terms in the free energy expansion arising from the coupling between the order parameters. As there are four basic invariants in our theory, there can be various terms up to quartic order coupling these order parameters and the associated phenomenological coefficients. For simplicity, we have considered only the most dominant lowest-order terms, which can account for the sequence of phases observed for our sample. The first term of the RHS of equation 3.9 is the lowest order coupling term between u and ζ, and we neglect the higher order terms. As the layer compression tends to decrease ζ, the coefficient λ_1 is assumed to be positive in our model. The second and third terms in equation 3.9 take into account the lowest order coupling between u and τ. The fourth and fifth terms in equation 3.9 take into account coupling between ζ and τ. The sixth term in equation 3.9 couples the three order parameters ζ, u and τ. We assume $\lambda_6 > 0$ as both compression and tilt reduce the uniaxial order ζ in the layers. The last term in equation 3.9 takes into account the coupling between the biaxial order parameter η and tilt order parameter τ. The coefficient μ_1 is assumed to be positive, which favors small biaxial order in the smectic C phase. As η is a non-critical order parameter and its value is assumed to be small, we discard all the other coupling terms involving higher powers of η in our model.

As usual in Landau theory, the coefficients α and A are assumed to be temperature dependent parameters with $\alpha = a(T - T_1)$ and $A = \alpha + a(T_1 - T_2)$ where a is a positive constant. The coefficients α and A change sign at the temperatures T_1 and T_2, respectively, where T_1 is assumed to be greater than T_2 in our model. All the other parameters of our model are assumed to be temperature-independent positive constants. The free energy density in equation 3.4 of the system can be made dimensionless by dividing it by the parameter χ, which has the same dimension as the free energy density. The dimensionless free energy density can be written as

$$\begin{aligned} f_h = \frac{1}{2}\zeta^2 + \frac{\alpha}{2}u^2 - \frac{\beta}{3}u^3 + \frac{\gamma}{4}u^4 + \frac{A}{2}\tau^2 + \frac{B}{4}\tau^4 + \frac{C}{2}\eta^2 + \lambda_1 u\zeta \\ - \lambda_2 u\tau^2 + \lambda_3 u^2\tau^2 + \lambda_4\zeta\tau^2 - \lambda_5\zeta^2\tau^2 + \lambda_6 u\zeta\tau^2 - \mu_1\eta\tau^2. \end{aligned} \tag{3.10}$$

Here, for convenience, we retain the same notation for the rescaled coefficients of the free energy density after dividing by χ. Minimization of the free energy with respect to η gives

$$\eta = \frac{\mu_1}{C}\tau^2, \tag{3.11}$$

which predicts induced biaxiality in the system due to the non-zero tilt order of the molecules. The order parameter η can be eliminated by substituting it from equation 3.11 in the free energy density in equation 3.10. The free energy density in terms of ζ, u and τ is given by

$$\begin{aligned} f_h = \frac{1}{2}\zeta^2 + \frac{\alpha}{2}u^2 - \frac{\beta}{3}u^3 + \frac{\gamma}{4}u^4 + \frac{A}{2}\tau^2 + \frac{\tilde{B}}{4}\tau^4 + \lambda_1 u\zeta \\ - \lambda_2 u\tau^2 + \lambda_3 u^2\tau^2 + \lambda_4\zeta\tau^2 - \lambda_5\zeta^2\tau^2 + \lambda_6 u\zeta\tau^2, \end{aligned} \tag{3.12}$$

where $\tilde{B} = B - 2\mu_1^2/C$. The elimination of the order parameter η effectively reduces the coefficient B without changing the other coefficients in the free energy density. Again, minimizing the free energy density in equation 3.12 with respect to the uniaxial order parameter ζ, we obtain

$$\zeta = -\frac{\lambda_1 u + \lambda_4\tau^2 + \lambda_6 u\tau^2}{1 - 2\lambda_5\tau^2}. \tag{3.13}$$

By plugging this expression for ζ into the free energy density in equation 3.12, one can express it in terms of only two order parameters, u and τ. The equilibrium values of u and τ can be determined by minimizing this reduced free energy density. It is found to be hard to minimize this reduced free energy density analytically due to the presence of highly non-linear terms. Hence, we use Python SciPy optimize module with Powell method as the numerical tool to minimize this free energy density.

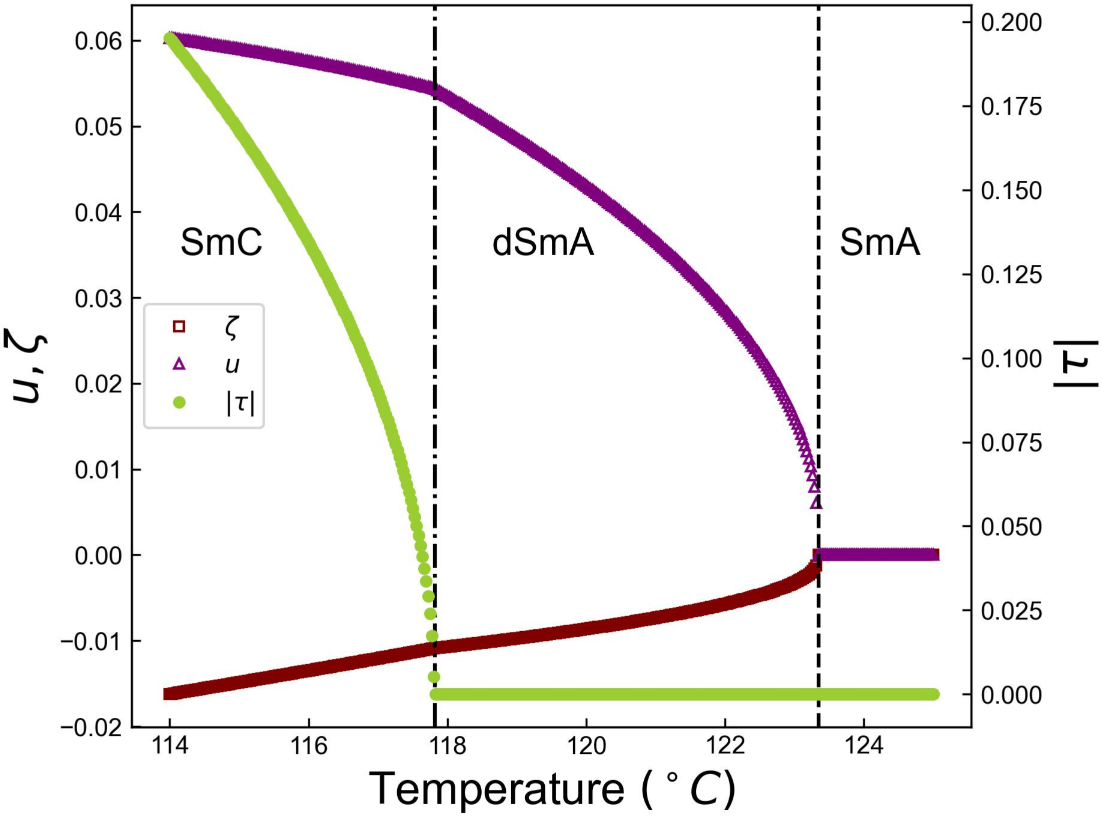

Figure 3.3: The variation of order parameters ζ, u and τ with temperature. The vertical lines represent the phase boundaries.

3.1.2 Results And Discussions

We numerically minimize the free energy density with a suitable choice of parameter values and determine the equilibrium phases at different temperatures. We also compare our theoretical results with our experimental observations. It is found that our theoretical results show good agreement with the experiments for the following choice of model parameters: $\beta = 0.32, \gamma = 43, \tilde{B} = 2.0, \lambda_1 = 0.2, \lambda_2 = 0.08, \lambda_3 = 1.5, \lambda_4 = 0.1, \lambda_5 = 0.1, \lambda_6 = 0.1, a = 0.02/°C, T_1 = 121.3°C$ and $T_2 = 117.7°C$.

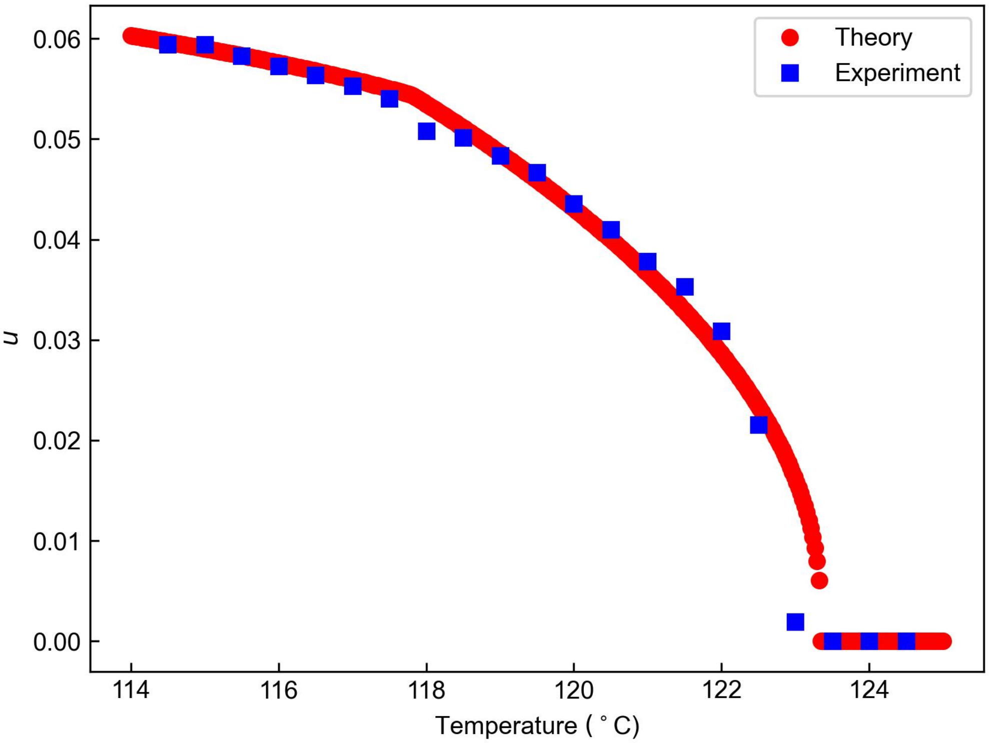

Figure 3.4: The variation of layer compression (u) as a function of temperature.

Figure. 3.3 represents the variation of three order parameters as a function of temperature. At higher temperatures in the SmA phase, all the three order parameters (ζ, u and τ) are zero. On cooling from the SmA phase, the system undergoes a first-order transition at about $123.3°C$ to the dSmA phase where the two order parameters ζ and u become non-zero, but the tilt order parameter τ remains zero. It should be noted that in the dSmA phase, ζ is negative and decreases with decreasing temperature as expected due to the conical distribution of molecular long axes about the layer normal. On the other hand, the layer compression order parameter u exhibits a small jump at the transition point and increases with decreasing temperature. The jump in u indicates a weakly first-order transition, which is confirmed by differential scanning calorimeter studies of our sample. It should be noted that the non-zero value of the parameter β predicts a first-order transition, and the ratio of β/γ determines its strength. In our model, the low value of $\beta/\gamma \sim 0.0074$ predicts a weakly first-order transition. On further cooling, the system undergoes a second-order transition from the dSmA phase to the SmC phase at the temperature $117.8°C$. In the SmC phase, all three order parameters become non-zero, and they vary continuously across the transition characteristic of a second-order transition. The order parameters τ and u in this phase increase with decreasing temperature, though the order parameter u varies slightly. In contrast, the uniaxial order parameter ζ decreases with decreasing temperature.

We compare the order parameter u with the layer compression obtained from experimentally measured layer thickness as a function of temperature using X-ray diffraction analysis. Figure. 3.4 shows the comparison between theoretical and experimental variations of u as a function of temperature, which agrees reasonably well for the above choice of model parameters. Therefore, the good agreement validates the theory accounting for the experimentally observed $SmA \rightarrow dSmA \rightarrow SmC$ phase transition.

Figure 3.5 depicts a numerically obtained phase diagram of the theoretical model. Depending on the parameter values α and A, the theory predicts the existence of the SmA, dSmA, and SmC phases. For large positive values of α and A, only the SmA phase is stable, whereas the dSmA phase is stable for large negative values of α. The SmA and dSmA phases are separated by a first-order transition denoted by a solid line. The symmetry of these phases being the same, a first-order transition is expected. The transitions between SmA to SmC and dSmA to SmC are second order in nature in our model and denoted by the dashed line in figure 3.5. These transitions are found to be second-order in nature for most of the experimental studies. Our theoretical model predicts a multicritical point where the first-order line meets and terminates on the second-order line. Both the parameters A and α are assumed to vary linearly with temperature in our model. Our experimental system is expected

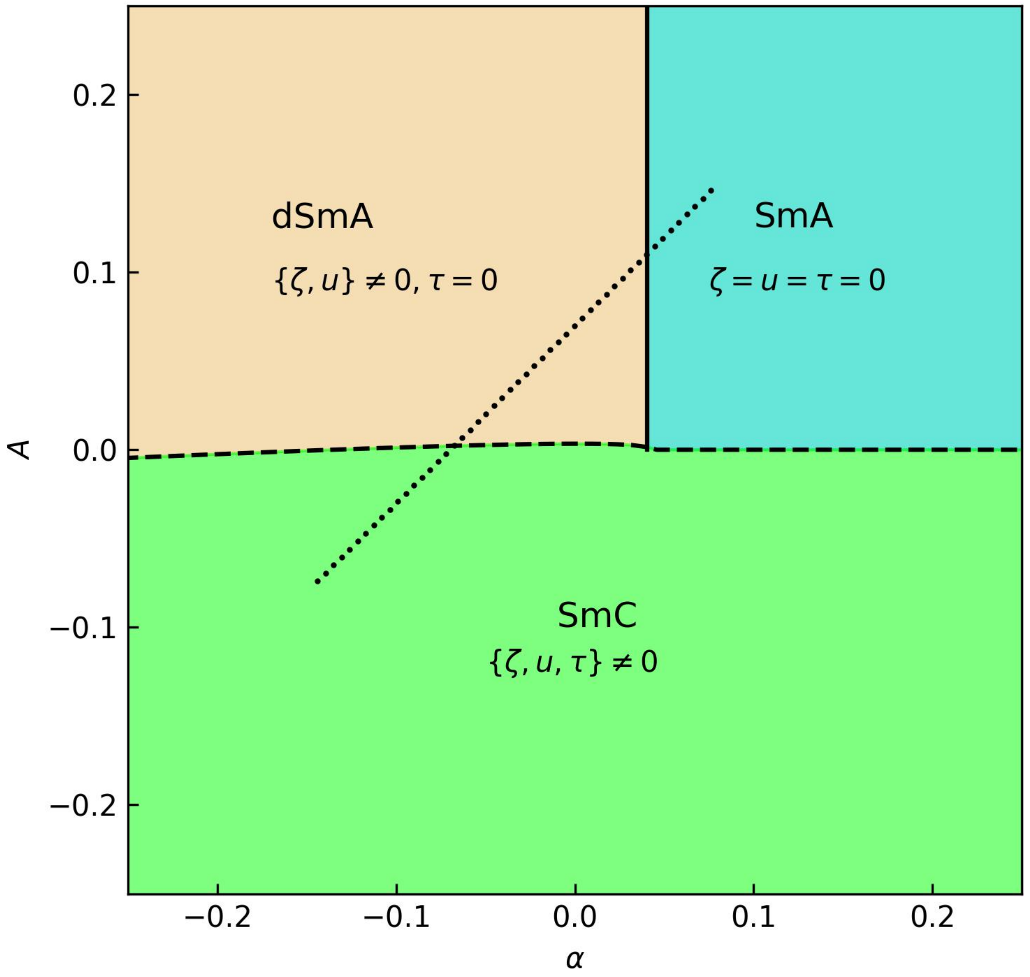

Figure 3.5: Numerically obtained phase diagram in $\alpha - A$ parameter's plane for the other parameter set $\beta = 0.32, \gamma = 43, \tilde{B} = 2.0, \lambda_1 = 0.2, \lambda_2 = 0.08, \lambda_3 = 1.5, \lambda_4 = 0.1, \lambda_5 = 0.1$, and $\lambda_6 = 0.1$. The black-coloured continuous line represents a first-order transition line, and the discontinuous (- -) line denotes the second-order phase transition line. Our system follows the path depicted by a black-coloured discontinuous $(\cdots)$ line.

to follow a typical path in the $\alpha - A$ parameter plane denoted by the dotted line. Therefore, our theoretical model predicts SmA $\rightarrow$ dSmA $\rightarrow$ SmC phase transitions along this line on decreasing temperature as observed experimentally.

3.2 Summary

In summary, we have constructed a theoretical model to account for the SmA–de Vries SmA–SmC phase sequence observed in our sample. We define a layer compression order parameter in addition to the orientational and tilt order parameters of the molecules. The theoretical model describes the weakly first-order phase transition from the SmA phase to the de Vries SmA phase and a second-order phase transition from the de Vries SmA phase to the SmC phase, as observed in our experimental studies. The temperature variation of the layer compression order parameter obtained from the theoretical model is compared with the experimental results. Our theoretical results agree reasonably well with experimental findings, giving the general validity of our model. We also compute a phase diagram showing the stability regions of these phases in a model parameter plane.

Bibliography

[1] T. P. Rieker, N. A. Clark, G. S. Smith, D. S. Parmar, E. B. Sirota, and C. R. Safinya, Phys. Rev. Lett. **59**, 2658 (1987), URL `https://link.aps.org/doi/10.1103/PhysRevLett.59.2658`.

[2] P. B. S. Diele and H. Sackmann, Molecular Crystals and Liquid Crystals **16**, 105 (1972), `https://doi.org/10.1080/15421407208083583`, URL `https://doi.org/10.1080/15421407208083583`.

[3] A. D. Vries, Molecular Crystals and Liquid Crystals **41**, 27 (1977), `https:`

`//doi.org/10.1080/01406567708071949`, URL `https://doi.org/10.1080/01406567708071949`.

[4] A. de Vries, The Journal of Chemical Physics **71**, 25 (2008), ISSN 0021-9606, `https://pubs.aip.org/aip/jcp/article-pdf/71/1/25/15355965/25_1_online.pdf`, URL `https://doi.org/10.1063/1.438123`.

[5] N. Hayashi, T. Kato, A. Fukuda, J. K. Vij, Y. P. Panarin, J. Naciri, R. Shashidhar, S. Kawada, and S. Kondoh, Phys. Rev. E **71**, 041705 (2005), URL `https://link.aps.org/doi/10.1103/PhysRevE.71.041705`.

[6] J. C. Roberts, N. Kapernaum, Q. Song, D. Nonnenmacher, K. Ayub, F. Giesselmann, and R. P. Lemieux, Journal of the American Chemical Society **132**, 364 (2010), pMID: 19994885, `https://doi.org/10.1021/ja9087727`, URL `https://doi.org/10.1021/ja9087727`.

[7] H. Yoon, D. M. Agra-Kooijman, K. Ayub, R. P. Lemieux, and S. Kumar, Phys. Rev. Lett. **106**, 087801 (2011), URL `https://link.aps.org/doi/10.1103/PhysRevLett.106.087801`.

[8] S. P. Sreenilayam, D. Rodriguez-Lojo, V. P. Panov, V. Swaminathan, J. K. Vij, Y. P. Panarin, E. Gorecka, A. Panov, and P. J. Stevenson, Phys. Rev. E **96**, 042701 (2017), URL `https://link.aps.org/doi/10.1103/PhysRevE.96.042701`.

[9] A. A. S. Green, M. R. Tuchband, R. Shao, Y. Shen, R. Visvanathan, A. E. Duncan, A. Lehmann, C. Tschierske, E. D. Carlson, E. Guzman, et al., Phys. Rev. Lett. **122**, 107801 (2019), URL `https://link.aps.org/doi/10.1103/PhysRevLett.122.107801`.

[10] S. Kaur, A. Barthakur, G. Mohiuddin, S. P. Gupta, S. Dhara, and S. K. Pal, Chem. Sci. **13**, 2249 (2022), URL `http://dx.doi.org/10.1039/D1SC06629C`.

[11] M. S. Spector, P. A. Heiney, J. Naciri, B. T. Weslowski, D. B. Holt, and R. Shashidhar, Phys. Rev. E **61**, 1579 (2000), URL `https://link.aps.org/doi/10.1103/PhysRevE.61.1579`.

[12] J. P. F. Lagerwall, F. Giesselmann, and M. D. Radcliffe, Phys. Rev. E **66**, 031703 (2002), URL `https://link.aps.org/doi/10.1103/PhysRevE.66.031703`.

[13] M. Krueger and F. Giesselmann, Phys. Rev. E **71**, 041704 (2005), URL `https://link.aps.org/doi/10.1103/PhysRevE.71.041704`.

[14] S. K. Prasad, D. S. S. Rao, S. Sridevi, C. V. Lobo, B. R. Ratna, J. Naciri, and R. Shashidhar, Phys. Rev. Lett. **102**, 147802 (2009), URL `https://link.aps.org/doi/10.1103/PhysRevLett.102.147802`.

[15] Y. Shen, L. Wang, R. Shao, T. Gong, C. Zhu, H. Yang, J. E. Maclennan, D. M. Walba, and N. A. Clark, Phys. Rev. E **88**, 062504 (2013), URL `https://link.aps.org/doi/10.1103/PhysRevE.88.062504`.

[16] J. P. F. Lagerwall and F. Giesselmann, ChemPhysChem **7**, 20 (2006), `https://chemistry-europe.onlinelibrary.wiley.com/doi/pdf/10.1002/cphc.200500472`, URL `https://chemistry-europe.onlinelibrary.wiley.com/doi/abs/10.1002/cphc.200500472`.

[17] M. V. Gorkunov, M. A. Osipov, J. P. F. Lagerwall, and F. Giesselmann, Phys. Rev. E **76**, 051706 (2007), URL `https://link.aps.org/doi/10.1103/PhysRevE.76.051706`.

[18] M. V. Gorkunov, F. Giesselmann, J. P. F. Lagerwall, T. J. Sluckin, and M. A. Osipov, Phys. Rev. E **75**, 060701 (2007), URL `https://link.aps.org/doi/10.1103/PhysRevE.75.060701`.

[19] Z. V. Kost-Smith, P. D. Beale, N. A. Clark, and M. A. Glaser, Phys. Rev. E **87**, 050502 (2013), URL `https://link.aps.org/doi/10.1103/PhysRevE.87.050502`.

[20] F. Jenz, M. A. Osipov, S. Jagiella, and F. Giesselmann, The Journal of Chemical Physics **145**, 134901 (2016), ISSN 0021-9606, `https://pubs.aip.org/aip/jcp/article-pdf/doi/10.1063/1.4963660/15520251/134901_1_online.pdf`, URL `https://doi.org/10.1063/1.4963660`.

[21] K. Saunders, D. Hernandez, S. Pearson, and J. Toner, Phys. Rev. Lett. **98**, 197801 (2007), URL `https://link.aps.org/doi/10.1103/PhysRevLett.98.197801`.

Chapter 4

Pattern formation and growth dynamics in a phase-field model

The phase-field model has received much attention due to its simplified implication in describing the vast majority of natural phenomena. Here, we present a phase-field model based on time-dependent Ginzburg-Landau equations containing a conserved and a non-conserved order parameters. Linear stability analysis of the model shows that a range of wave vectors become unstable depending on the values of model parameters. Generally, the wave vector corresponding to the fastest-growing mode mostly dominants over the other modes, and it determines the characteristic length scale of the instability-induced patterns. We have studied the variation of the wavelength obtained from the fastest instability mode as a function of the model parameters. In addition, we have carried out numerical studies on the model to investigate the pattern formation and their growth dynamics. The numerical studies exhibit a rich variety of patterns, such as ring banded (target), broken ring, and continuous patterns. A state diagram has also been constructed depending on the model parameters to indicate the stability regions of these patterns. The patterns mostly grow with a circular growth front exhibiting either rhythmic or non-rhythmic growth dynamics in their radius. However, the radius of the pattern increases, on average, linearly with time.

4.1 Introduction

Patterns are everywhere in nature, from microscopic to cosmic scales [1–3]. They have been the subject of curiosity throughout human history. Nonequilibrium systems produce rich and fascinating varieties of spatial or spatiotemporal patterns [4]. Despite their abundant existence, the understanding of the diversity of patterns and their microscopic origin is still incomplete. The pattern formation in systems can arise due to various mechanisms. For instance, the chemical reaction and diffusion of reactants control the pattern formation in the reactive chemical solutions [5], whereas the spinodal decomposition can develop the self-aggregated structures in the immiscible liquid mixture during phase transition. In addition to the spatial structure of the patterns, the growth dynamics often play a significant role in the understanding of the pattern formation. In particular, visually indistinguishable patterns can form due to different kinds of growth dynamics. The applications and rich varieties of the phenomena make the study of pattern formation as an active field of research.

A large number of studies using the phase-field model [6–8] have been reported to describe the structure formation in various systems. These types of models account for a vast majority of phenomena such as solidification of a melt, phase separation of a binary mixture, dendritic growth in pure materials [9], eutectic and dendritic growth in alloys, viscous fingering, crack propagation, and vesicle dynamics [10]. During crystallization, a rich variety of systems such as polymer [11, 12], mineral, liquid crystal [13], and biological material exhibit the polycrystalline aggregate structures with a spherical growth front called spherulite [1, 14]. The essential structural features of the spherulites are the fibrous habit of crystallization and non-crystallographic branching

[15]. Some spherulites, known as banded spherulites, show concentric band structures during their formation. These bands are associated with the radial modulation of the birefringence in the spherulites. The growth dynamics of the spherulites have also been studied using the phase-field model [6, 16, 17].

A phase-field model generally involves one or multiple continuous conserved or non-conserved field variables known as order parameters. These order parameters are defined by coarse-grained averaging of some quantities over the microscopic configurations of the constituent particles. Thus, the model does not explicitly deal with the properties of the individual particle. The order parameters are usually associated with the macroscopic properties of the system, such as density, compositions, orientational order, etc and each phase of the system is characterized by the order parameter. In general, the order parameters of a system are a function of position $\mathbf{r}$ and time t. For instance, in two coexisting phases, the bulk values of an order parameter $\eta(\mathbf{r}, t)$ vary from $\eta = 0$ in the first phase to $\eta = 1$ in the second phase. The value of η as a function of $\mathbf{r}$ changes smoothly between the two phases to obey a continuity condition and produces a diffusive interface of finite thickness. The position of the interface can be determined by the intermediate value $\eta = 0.5$. Thus, the phase field model naturally takes into account the interface between two phases in contrast to other models assuming sharp interfaces [7]. The dynamics of the model order parameters are governed by a relaxation mechanism minimizing the system's free energy, which is a functional of the order parameters.

A variety of phase-field models have been adopted in the literature to describe various phenomena. Among these models, the time-dependent Ginzburg-Landau (TDGL) models are mostly used to describe the pattern formation across the phase transition [18]. The TDGL model associated with non-conserved order parameters is called model A or the Allen-Cahn model. The TDGL model with conserved order parameters is known as model B, such as the Cahn-Hilliard model for phase segregation in binary mixture [19]. The combination of model A and model B is known as TDGL model C which has been applied in various phenomena such as liquid-liquid phase transition [20–22], crystal growth in metal alloys [23], eutectic crystal growth [24], liquid-liquid phase separation and crystallization of a polymer blend [25], and structure of nanoparticle doped liquid crystalline system [26]. A model of type C was found to exhibit rhythmic growth of banded spherulite in polymer blends [27]. Recently, the banded spherulitic growth has been observed in a pure liquid crystalline compound during its solidification from its melts. We have developed a TDGL model C to account for this spherulitic growth [28]. In this chapter, we explore this model in its parameter space to get better insights into the stable morphologies of the patterns and their growth dynamics.

Here, we report a detailed study on TDGL model C using linear stability analysis (LSA) and numerical computation. The LSA analysis shows that the modes with a range of wave vectors become unstable depending on the model parameters. In general, the wave vector corresponding to the fastest-growing mode mostly dominates over the other modes, and it determines the characteristic length scale of the induced patterns. We study the variation of this characteristic length scale as a function of various model parameters. It is found that the length scale strongly varies with the model parameters. The numerical studies of the full non-linear equations of the model were performed to obtain various pattern morphologies and investigate their growth dynamics. Various patterns such as ring banded (target), broken ring, and continuous patterns are observed depending on the model parameters. We have established a state diagram displaying the stability regions of these patterns in the model parameter space. It is found that these patterns mostly grow as a circular domain and exhibit either rhythmic or non-rhythmic growth of their radius. In rhythmic growth, the radius of the pattern increases in a step-like fashion with time, giving rise to non-uniform growth dynamics. Though the growth of radius is non-linear at each individual step, it shows, on average, a linear growth law with time. On the other hand, for non-rhythmic growth, the radius of the pattern increases linearly and smoothly with time. In both cases, the radius of the pattern generally increases on average linearly with time. The numerical studies also predict various intermediate patterns and their growth dynamics.

4.2 Theoretical Model

A time-dependent Ginzburg-Landau model C (TDGL) can be defined by expressing the free energy of the system in terms of a conserved and a non-conserved order parameter. For a conserved order parameter, its volume integral over the system remains constant, whereas this integral for the non-conserved order parameter may vary with time. We have developed a TDGL model by writing the Ginzburg-Landau free energy of the system $F(\phi, \psi)$ in terms of a scalar conserved order parameter ϕ and a scalar non-conserved order parameter ψ. The physical realization of two order parameters varies from system to system. The conserved order parameter ϕ may represent the density or the fluctuation of density for a pure system [20–22, 28], the densities in a multi-component system [27, 29] whereas the non-conserved order parameter ψ may relate to the composition in a multi-phase coexisting system [28], ratio of lamella thicknesses for a polymeric system [29], bond order parameter [20–22], and crystal order parameter [27]. In general, the free energy of the system can be written as

$$F(\phi, \psi) = \int dV [f_h(\phi, \psi) + f_{inh}(\phi, \psi)] \ , \tag{4.1}$$

where $f_h(\phi, \psi)$ and $f_{inh}(\phi, \psi)$ are the homogeneous and inhomogeneous parts of the free energy density, respectively. The free energy density can be expanded in terms of the order parameters consistent with symmetries of the disordered state of the system. The homogeneous part of the free energy density can be written as

$$f_h(\phi, \psi) = f(\psi) + f(\phi) + f(\phi, \psi) \tag{4.2}$$

where

$$f(\psi) = W\left(\frac{\alpha}{2}\psi^2 - \frac{\beta}{3}\psi^3 + \frac{\chi}{4}\psi^4\right) \tag{4.3}$$

$$f(\phi) = \frac{A}{2}\phi^2 \tag{4.4}$$

$$f(\phi, \psi) = -\gamma\phi\psi. \tag{4.5}$$

The free energy density $f(\psi)$ given by equation 4.3 depends only on the non-conserved order parameter ψ, and it can describe a phase transition from the $\psi = 0$ state to a ψ non-zero state depending on the model parameters α, β and χ. The non-zero value of the model parameter β gives a first-order transition. The factor W in equation 4.3 is an overall scale factor of the energy density. Equation 4.4 represents the contribution to the free energy density due to the conserved order parameter ϕ. Here, ϕ is assumed to be small and non-critical, and we retain terms up to the quadratic order in ϕ. The parameter A is a positive constant giving rise to the equilibrium value of ϕ equal to zero. The mutual interaction between these two order parameters is given by the free energy density expression 4.5. We consider only the lowest order bi-linear coupling between the order parameters where γ is a coupling constant. The sign of γ determines the nature of the mutual interaction. Here, γ is assumed to be positive, giving rise to the in-phase variation of the two order parameters.

The inhomogeneous part of the free energy density takes into account the long wavelength spatial variation of the order parameters. At a minimal level, this part of the free energy density for our system can be written as

$$f_{inh} = \frac{k_\phi}{2}|\nabla\phi|^2 + \frac{k_\psi}{2}|\nabla\psi|^2 \tag{4.6}$$

where k_ϕ and k_ψ are the material-specific elastic constants. The values of these constants are assumed to be positive to ensure the homogeneity of the ground state of the system.

Using the total free energy of the system, the temporal evolution of these two order parameters is described by the time-dependent Ginzburg-Landau model C. For the conserved order parameter ϕ and non-conserved order parameter ψ, the equations are given by

$$\begin{aligned} \frac{\partial\phi}{\partial t} &= \Gamma_\phi \nabla^2 \frac{\delta F(\phi,\psi)}{\delta\phi} \\ \frac{\partial\psi}{\partial t} &= -\Gamma_\psi \frac{\delta F(\phi,\psi)}{\delta\psi}, \end{aligned} \tag{4.7}$$

where $\delta/\delta\phi$ and $\delta/\delta\psi$ denote the functional derivative with respect to the order parameters ϕ and ψ respectively. The constants Γ_ϕ and Γ_ψ are the phenomenological kinetic coefficients of the system. Using the total free energy of the system discussed above, the dynamical equations of the order parameters can be written as

$$\begin{aligned} \frac{\partial\phi}{\partial t} &= \Gamma_\phi \nabla^2 \big[A\phi - \gamma\psi - k_\phi \nabla^2\phi\big] \\ \frac{\partial\psi}{\partial t} &= -\Gamma_\psi \big[W(\alpha\psi - \beta\psi^2 + \chi\psi^3) - \gamma\phi - k_\psi \nabla^2\psi\big]. \end{aligned} \tag{4.8}$$

The equations 4.8 can be expressed in a dimensionless form by the transformations $x \rightarrow x' = \frac{\sqrt{\epsilon}}{\xi_\phi}x, t \rightarrow t' = \frac{\epsilon\Gamma_\phi A}{\xi_\phi^2}t$, where $\epsilon = \big(\frac{\gamma^2}{WA} - \alpha\big)$ and $\xi_\phi = \sqrt{\frac{k_\phi}{A}}$. For convenience, omitting the prime notation on the transformed spatial and time variables, the dimensionless form of the dynamical equations becomes

$$
\begin{aligned}
\frac{\partial\phi}{\partial t} &= \nabla^2\big[\phi - \frac{\gamma}{A}\psi - \epsilon\nabla^2\phi\big] \\
\frac{\partial\psi}{\partial t} &= -\frac{\xi_\phi^2}{\epsilon\lambda_D^2}\Big[\alpha\psi - \beta\psi^2 + \chi\psi^3 - \frac{\gamma}{W}\phi - \epsilon\frac{\xi_\psi^2}{\xi_\phi^2}\nabla^2\psi\Big]
\end{aligned}
\tag{4.9}
$$

where $\xi_\psi = \sqrt{\frac{k_\psi}{W}}$ and $\lambda_D^2 = \frac{A\Gamma_\phi}{W\Gamma_\psi}$. The equations 4.9 are non-linear coupled partial differential equations, and the analytical solutions of these dynamical equations are not known. We, therefore, performed numerical studies to investigate the growth dynamics of the system governed by these equations. We also performed the linear stability analysis of these equations to study the unstable modes of the system.

4.3 Linear stability analysis

The linear stability analysis is generally performed by giving small perturbations to the system about a fixed point and linearizing the non-linear paritial differential equations. Therefore, we write $\phi(\vec{r},t) = \phi^* + \delta\phi(\vec{r},t)$ and $\psi(\vec{r},t) = \psi^* + \delta\psi(\vec{r},t)$ where (ϕ^*, ψ^*) denotes a fixed point of the system. The equations 4.9 in our model are linearised about the fixed point ($\phi^* = 0$, $\psi^* = 0$). Then, the linear dynamical equations for the small perturbations $\delta\phi(\vec{r},t)$ and $\delta\psi(\vec{r},t)$ are

$$
\begin{aligned}
\frac{\partial\delta\phi}{\partial t} &= \nabla^2\Big[\delta\phi - \frac{\gamma}{A}\delta\psi - \epsilon\nabla^2\delta\phi\Big] \\
\frac{\partial\delta\psi}{\partial t} &= -\frac{\xi_\phi^2}{\epsilon\lambda_D^2}\Big[\alpha\delta\psi - \frac{\gamma}{W}\delta\phi - \epsilon\frac{\xi_\psi^2}{\xi_\phi^2}\nabla^2\delta\psi\Big]\ .
\end{aligned}
\tag{4.10}
$$

Assuming the solution of the above two equations in the form $\delta\phi = \delta\phi_0 e^{\sigma t} e^{i\vec{q}\cdot\vec{r}}$ and

$\delta\psi = \delta\psi_0 e^{\sigma t} e^{i\vec{q}\cdot\vec{r}}$, we obtain

$$\begin{aligned}
\sigma\delta\phi_0 e^{\sigma t} e^{i\vec{q}\cdot\vec{r}} &= \Big[-(q^2+\epsilon q^4)\delta\phi_0 + \frac{\gamma}{A} q^2 \delta\psi_0\Big] e^{\sigma t} e^{i\vec{q}\cdot\vec{r}} \\
\sigma\delta\psi_0 e^{\sigma t} e^{i\vec{q}\cdot\vec{r}} &= -\frac{\xi_\phi^2}{\epsilon\lambda_D^2}\Big[\alpha\delta\psi_0 - \frac{\gamma}{W}\delta\phi_0 + \epsilon\frac{\xi_\psi^2}{\xi_\phi^2} q^2 \delta\psi_0\Big] e^{\sigma t} e^{i\vec{q}\cdot\vec{r}}
\end{aligned}$$

or

$$\begin{aligned}
\sigma\delta\phi_0 &= -(\epsilon q^4 + q^2)\delta\phi_0 + \frac{\gamma}{A} q^2 \delta\psi_0 \\
\sigma\delta\psi_0 &= \frac{\xi_\phi^2}{\epsilon\lambda_D^2}\frac{\gamma}{W}\delta\phi_0 - \frac{\xi_\phi^2}{\epsilon\lambda_D^2}\big[\alpha + \epsilon\frac{\xi_\psi^2}{\xi_\phi^2} q^2\big]\delta\psi_0 .
\end{aligned}$$

These equations can be represented as the eigenvalue equation

$$B \begin{pmatrix} \delta\phi_0 \\ \delta\psi_0 \end{pmatrix} = \sigma \begin{pmatrix} \delta\phi_0 \\ \delta\psi_0 \end{pmatrix},$$

where

$$B = \begin{bmatrix} -(q^2+\epsilon q^4) & \frac{\gamma}{A} q^2 \\ \frac{\gamma\xi_\phi^2}{\epsilon W \lambda_D^2} & -\frac{\xi_\phi^2}{\epsilon\lambda_D^2}\big[\alpha + \epsilon\frac{\xi_\psi^2}{\xi_\phi^2} q^2\big] \end{bmatrix}.$$

The eigenvalues of the matrix B can be determined from the equation $\sigma^2 - \tau\sigma + \Delta = 0$, where $\tau = tr(B)$ and $\Delta = det(B)$. The trace τ and determinant Δ are given by

$$\tau = -(q^2+\epsilon q^4) - \frac{\xi_\phi^2}{\epsilon\lambda_D^2}\big(\alpha + \epsilon\frac{\xi_\psi^2}{\xi_\phi^2} q^2\big) \tag{4.11}$$

$$\Delta = \frac{\xi_\phi^2}{\epsilon\lambda_D^2}\big(q^2+\epsilon q^4\big)\big(\alpha + \epsilon\frac{\xi_\psi^2}{\xi_\phi^2} q^2\big) - \frac{\gamma^2\xi_\phi^2}{\epsilon W A \lambda_D^2} q^2 \ . \tag{4.12}$$

The eigenvalues $\sigma_\pm = \frac{\tau \pm \sqrt{\tau^2 - 4\Delta}}{2}$ can be complex in general. If the real part of any of these eigenvalues is positive, the corresponding mode grows with time ($\sim e^{\sigma t}$), and the fixed point is unstable. On the other hand, the fixed point is stable if the real part of both the eigenvalues is negative.

It is found that in our system τ becomes negative for $\alpha \geq 0$ and hence the real part of σ_- is negative for all values of q. Thus, the modes corresponding to the eigenvalue σ_- are stable. On the other hand, the real part of the eigenvalue σ_+ becomes positive if $\Delta < 0$. Thus the modes corresponding to σ_+ are unstable. It can be shown from the equation 4.12 that Δ becomes negative in the range $0 < q < q_{max}$ where q_{max} can be obtained by solving the equation

$$\epsilon \frac{\xi_\psi^2}{\xi_\phi^2} q^4 + \Big(\alpha + \frac{\xi_\psi^2}{\xi_\phi^2}\Big) q^2 - 1 = 0. \tag{4.13}$$

The expression of q_{max} relevant to our analysis is given by

$$q_{max} = \frac{1}{\sqrt{2\epsilon}} \left[\sqrt{\frac{4\epsilon\xi_\phi^2}{\xi_\psi^2} + \Big(1 + \frac{\alpha\xi_\phi^2}{\xi_\psi^2}\Big)^2} - \Big(1 + \frac{\alpha\xi_\phi^2}{\xi_\psi^2}\Big) \right]^{1/2}. \tag{4.14}$$

In the case of $\alpha < 0$, it can be shown from equation 4.11 that τ is positive for small values of q and becomes negative for large values of q. Hence, the growth rate $\sigma_+ = \tau$ is a positive quantity for $q = 0$, and it becomes zero at $q = q_{max}$. As $\Delta(q_{max}) = 0$, the expression 4.14 of q_{max} is valid for both positive and negative values of α. For both cases, the fastest growing mode $q = q_c$ can be found by maximising σ_+ with respect to q, which will be the most dominant mode in the system.

Figure 4.1 shows the typical variation of the growth rate σ as a function of the wave vector q for different values of the model parameter α. For low values of $\alpha < 0$, the growth rate is maximum at $q_c = 0$ as shown in figure 4.1 (a). Then, q_c becomes non-zero and increases with increasing value of α. Whereas for positive values of α, the wave vector q_c is always a non-zero quantity, and it increases with increasing values of α (see figure 4.1 (b)). The non-zero values of q_c, therefore, determine the periodicity of the spatial patterns formed after the instability. In the following, we consider mostly the positive values of α to ensure the non-zero value of q_c. The positive values of α have also been assumed in other studies accounting for banded spherulitic growth [27, 29].

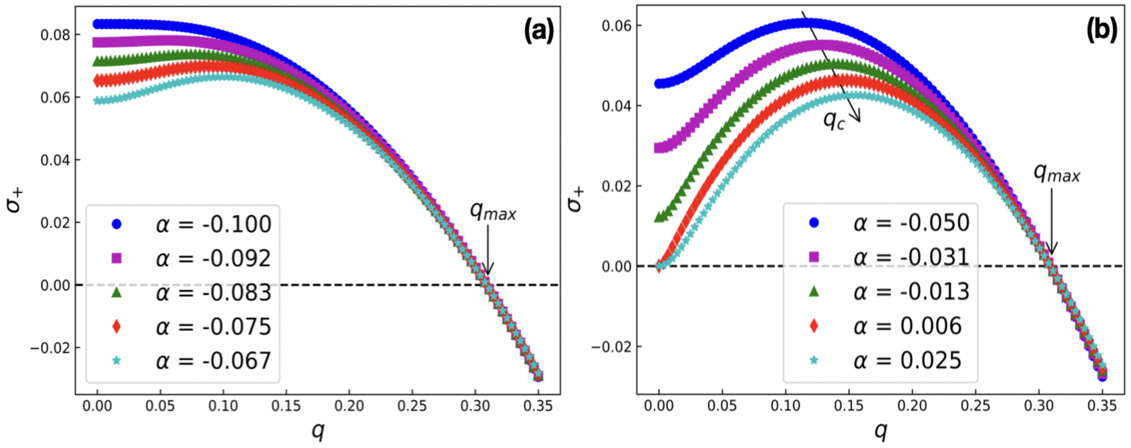

Figure 4.1: The variation of growth rate σ as a function of the wave vector q for different values of α (a) $-0.1 \leq \alpha \leq -0.067$ and (b) $-0.05 \leq \alpha \leq 0.025$. The modes in the wave vector range $0 < q < q_{max}$ have positive values of σ^+ and hence are unstable. The values of the other parameters are $\gamma/A = 0.2236$, $W/A = 0.1$, $\xi_\psi/\xi_\phi = 3.1623$, and $\xi_\phi^2/\lambda_D^2 = 0.5$.

The wavelength corresponding to the fastest growing mode λ in the units of the length ξ_ϕ is given by

$$\lambda = \frac{2\pi}{q_c\sqrt{\epsilon}} \ , \tag{4.15}$$

which can be compared with the experimentally measured periodicity of the patterns [28]. It can be seen from the equation 4.15 that λ diverges at $\epsilon = 0$ corresponding to $\alpha = \gamma^2/WA$. We showed that this divergence of λ is a manifestation of the singularity of the governing TDGL equations [28]. The singularity of the model is associated with the reduction of the number of time-dependent equations, which can be understood by putting $\epsilon = 0$ in the equation 4.9. It can be shown from equations 4.11 and 4.12 that the wave vector q_c depends on the model parameters $\alpha, \xi_\phi/\lambda_D, \xi_\psi/\xi_\phi, \gamma/A$ and W/A and it is independent of β and χ. Therefore, the nature of the phase transition determined by the parameter β does not impact the selection of the wavelength λ. Figure 4.2 presents the variation of λ and its growth rate (i.e., $\sigma = \sigma^+_{max}$) as a function of α. The wavelength λ initially decreases and shows a broad minimum at about $\alpha = 0.1$ and then increases monotonically with increasing values of α. It shows a divergence at higher values of α on approaching $\epsilon = 0$, as pointed out earlier. On the other hand, the growth rate σ decreases monotonically with increasing values of α.

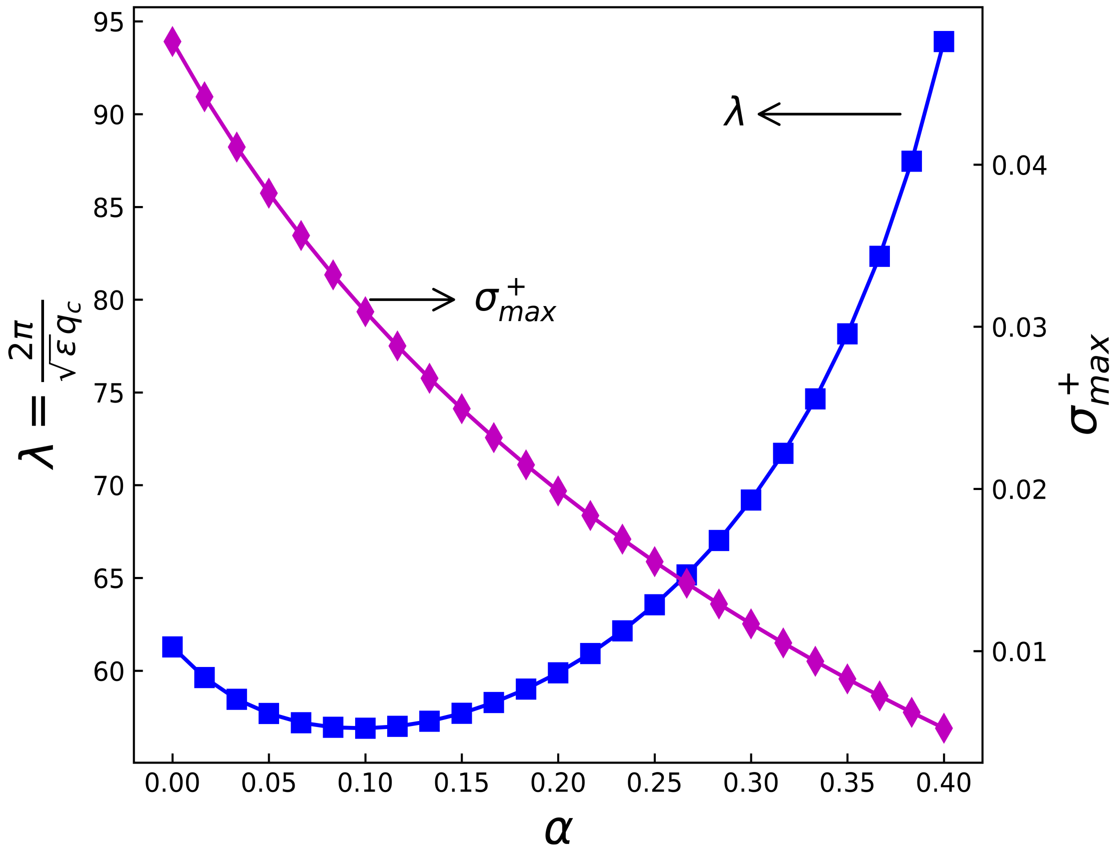

Figure 4.2: The variation of wavelength and growth rate corresponding to the fastest instability mode (q_c) as a function of α. The values of the other parameters are $\gamma/A = 0.2236$, $W/A = 0.1$, $\xi_\psi/\xi_\phi = 3.1623$, $\xi_\phi^2/\lambda_D^2 = 0.5$.

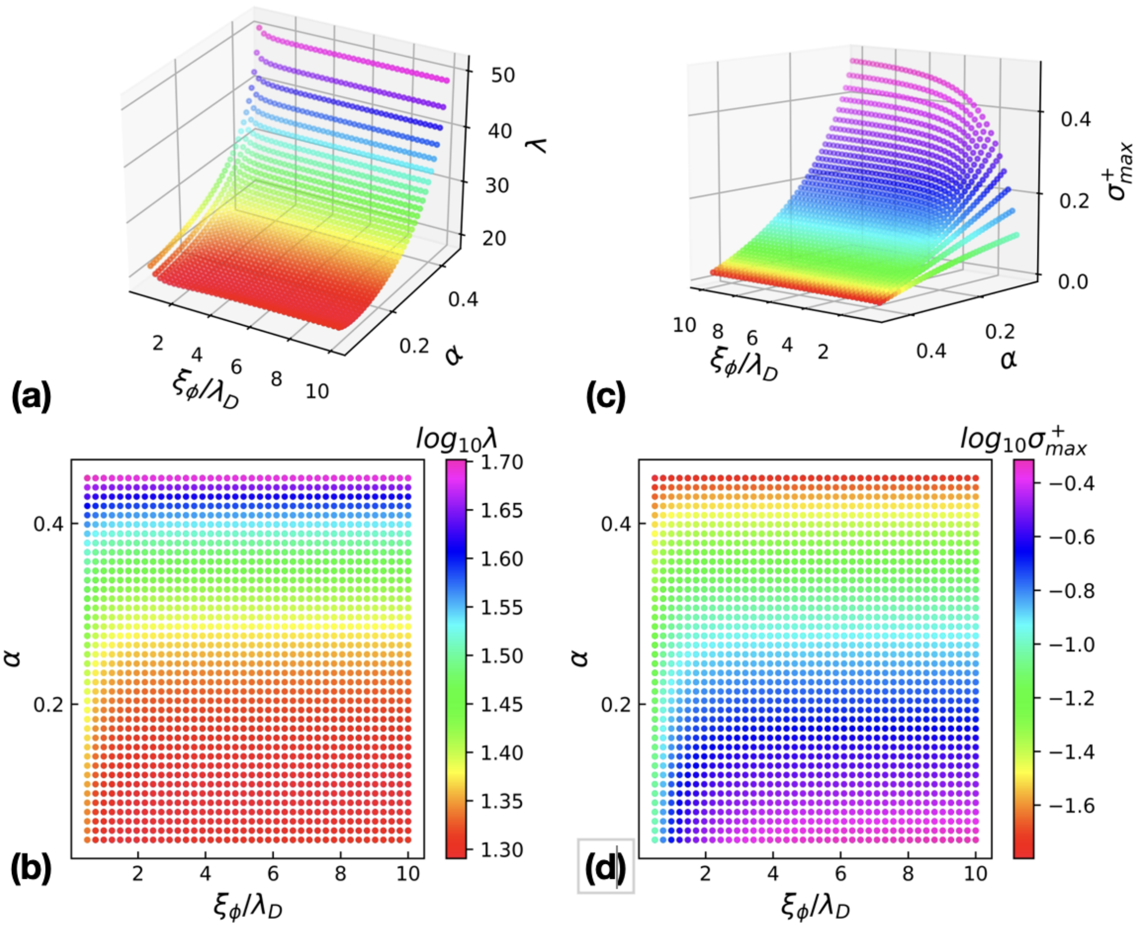

Figure 4.3: Three dimensional (3D) plots (a) and (c) of the length scale λ and its growth rate σ^+_{max}, respectively, as a function of two model parameters α and ξ_ϕ/λ_D. Other model parameters are $\gamma/A = 0.7071$, $W/A = 1.0$, and $\xi_\psi/\xi_\phi = 1.0$. The 2D projections of these 3D plots are (b) and (d), respectively, where the color bars represent the value of λ and σ_{max} in the logarithmic scale.

We now present the variation of the wavelength corresponding to the fastest-growing mode and its growth rate with different model parameters. Figure 4.3 (a) and (c) show the 3D plot of λ and σ^+_{max} as a function of the parameters α and ξ_ϕ/λ_D respectively, whereas figure 4.3 (b) and (d) show the color-coded representations of these variables. As can be seen from figure 4.3 (a), λ diverges with increasing values of α for a given value of ξ_ϕ/λ_D as discussed earlier. This trend remains almost independent of ξ_ϕ/λ_D except for very low values of ξ_ϕ/λ_D where λ slightly increases with decreasing values of ξ_ϕ/λ_D. Similarly, σ_{max} shows corresponding behaviour as shown in figure 4.3 (c). It should be noted that the ξ_ϕ/λ_D is related to the kinetic coefficients $(\Gamma_\phi, \Gamma_\psi)$, which, therefore, weakly control the dynamics of the unstable modes.

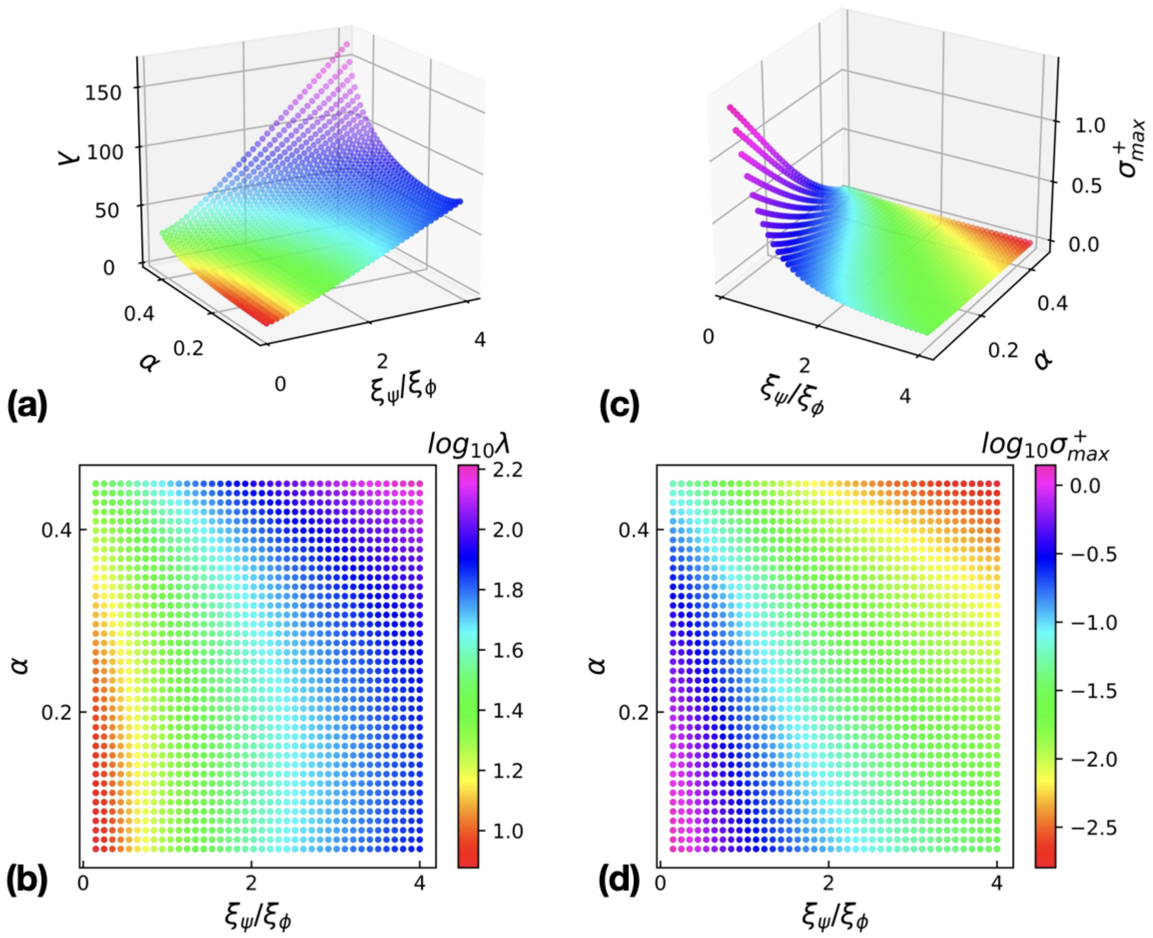

Figure 4.4: Three dimensional (3D) plots (a) and (c) of the length scale λ and its growth rate σ^+_{max}, respectively, as a function of two model parameters α and ξ_ψ/ξ_ϕ. Other model parameters are $\gamma/A = 0.7071$, $W/A = 1.0$ and $\xi^2_\phi/\lambda^2_D = 5.0$. The 2D projections of these 3D plots are (b) and (d), respectively, where the color bars represent the value of λ and σ_{max} in the logarithmic scale.

Figure 4.4 presents the variation of λ and σ^+_{max} as a function of α and ξ_ψ/ξ_ϕ. The variations of λ and σ^{max} with respect to α strongly depend on the chosen values of ξ_ψ/ξ_ϕ. For large values of ξ_ψ/ξ_ϕ, λ varies rapidly with α compared to that for low values of ξ_ψ/ξ_ϕ as shown in figure 4.4 (a). On the other hand, σ^+_{max} shows the opposite trend as shown in figure 4.4 (c). It should be noted that ξ_ψ/ξ_ϕ depends on the ratio of the elastic constants associated with the spatial variation of the order parameters ψ and ϕ, respectively. The increasing λ with the increasing values of ξ_ψ/ξ_ϕ arises due to the higher elastic energy cost associated with the spatial variation of the order parameter ψ.

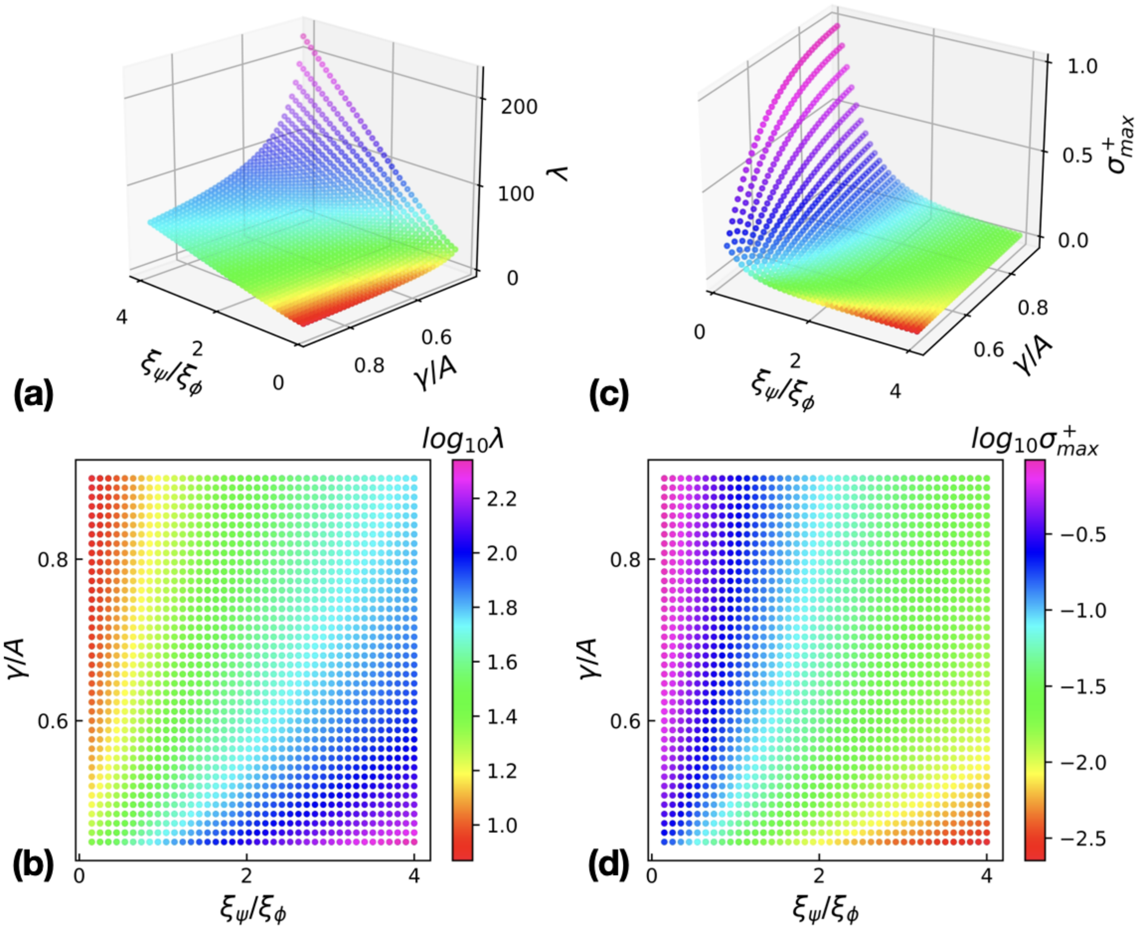

Figure 4.5: Three dimensional (3D) plots (a) and (c) of the length scale λ and its growth rate σ^+_{max}, respectively, as a function of two model parameters γ/A and ξ_ψ/ξ_ϕ. Other model parameters are $\alpha = 0.175$, $W/A = 1.0$ and $\xi_\phi^2/\lambda_D^2 = 5.0$. The 2D projections of these 3D plots are (b) and (d), respectively, where the color bars represent the value of λ and σ_{max} in the logarithmic scale.

Figure 4.5 (a) and (c) present the variation of λ and σ^+_{max} as a function of γ/A and ξ_ψ/ξ_ϕ, respectively whereas figure 4.5 (b) and (d) show the color-coded representations of these variables on the $\gamma/A - \xi_\psi/\xi_\phi$ parameter plane. As can be seen from figure 4.5 (a), λ increases with decreasing values of γ/A for a given value of ξ_ψ/ξ_ϕ. On the other hand, σ^+_{max} shows the opposite trend as shown in figure 4.5 (c). It is found that for large values of ξ_ψ/ξ_ϕ, λ and σ^+_{max} vary rapidly with γ/A compared to those for low values of ξ_ψ/ξ_ϕ.

The linear stability analysis shows that the region of higher (lower) wavelength λ corresponds to the lower (higher) values of growth rate σ^+_{max}. The length scale λ strongly depends on α. Generally, the parameter α is a temperature-dependent quantity, and hence, it can be associated with the supercooling of the system. The effect of α on the pattern formation has been experimentally studied by changing the supercooling of the system[27–29]. On the other hand, the parameters γ/A and ξ_ψ/ξ_ϕ can be tuned easily by changing the concentration of materials in a multi-component system. However, the effect of these two model parameters on pattern formation has not been reported in the literature. We showed theoretically that λ also depends strongly on the model parameters γ/A and ξ_ψ/ξ_ϕ. It should be noted that the linear stability analysis can not provide the full dynamics of the system as it deals with the assumption of small perturbations and linearised equations. Therefore, we solved the full non-linear TDGL equations for different values of these model parameters to study the pattern formation.

4.4 Numerical Studies

For numerical solutions, we introduce an additional auxiliary variable μ and the TDGL equations 4.9 can be written as

$$\frac{\partial \phi}{\partial t} = \nabla^2 \mu \tag{4.16}$$

$$\mu = \phi - \frac{\gamma}{A}\psi - \epsilon \nabla^2 \phi \tag{4.17}$$

$$\frac{\partial \psi}{\partial t} = -\frac{\xi_\phi^2}{\epsilon \lambda_D^2}\Big[\alpha\psi - \beta\psi^2 + \chi\psi^3 - \frac{\gamma}{W}\phi - \epsilon\frac{\xi_\psi^2}{\xi_\phi^2}\nabla^2\psi\Big]. \tag{4.18}$$

These equations were solved numerically in two dimensions with no flux boundary conditions

$$
\begin{aligned}
\vec{\nabla}\phi \cdot \hat{n}|_{\partial\Omega} &= 0 \qquad (4.19)\\
\vec{\nabla}\psi \cdot \hat{n}|_{\partial\Omega} &= 0 \qquad (4.20)\\
\vec{\nabla}\mu \cdot \hat{n}|_{\partial\Omega} &= 0\ , \qquad (4.21)
\end{aligned}
$$

where $\partial\Omega$ represents the boundary. The last boundary condition arises from the conservation law of the order parameter ϕ. The finite difference method for both space and time was used for the discretization of these equations. The Laplace operators were discretized based on second-order central differences. The spatial step size was chosen as $dx = dy = 1.0$. Initially, a single nucleus was put at the center of the square lattice by considering $\psi(\vec{r}) = \exp(-0.1r^2)$ where r is the radial distance of a point from the center and ϕ was taken as zero everywhere. A similar Gaussian profile has also been used in the literature to trigger the nucleation event in the numerical simulation of crystallization [30]. Following earlier studies accounting for banded spherulitic growth [27, 29], we consider $\beta = 1 + \alpha$ where $\alpha > 0$ and $\chi = 1$ in most of the simulations. We have also performed the simulation for $\alpha = -0.1$ and $\beta = 0$ corresponding to a continuous phase transition.

We now present the numerical solutions of the two order parameters ϕ and ψ for different values of the model parameters. Figure 4.6 (a) and (b) show the typical ring banded patterns obtained from numerical simulations for the model parameter $\beta \neq 0$ and $\beta = 0$, respectively. The ring-banded pattern grows from the center with periodic variation of the order parameters ϕ and ψ along the radial directions, forming circular bands. For $\beta \neq 0$, the left and middle panes of figure 4.6 (a) show the two-dimensional variation of ϕ and ψ, respectively, using a color map. In this case, the radius of the ring-banded pattern increases in a step-like fashion with time, giving rise to the non-uniform growth dynamics, as shown in the right pane of figure 4.6(a). Despite the non-linear variation of the radius with time for each individual step, the radius shows, on average, a linear growth law with time. This type of non-linear growth dynamics is known as rhythmic growth. The free energy density also varies rhythmically with time, as shown in the right pane of figure 4.6(a). Similar ring-banded patterns with rhythmic growth have also been found in earlier studies [27, 29].

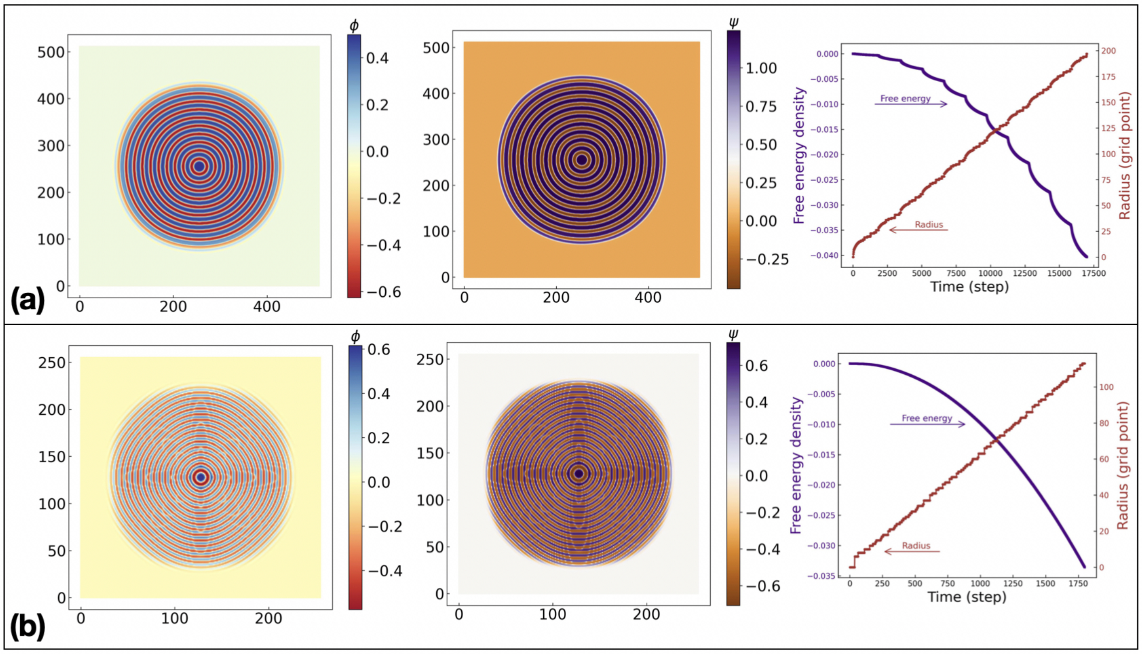

Figure 4.6: The left and middle panes representing the color-coded variation of the order parameters ϕ and ψ for the ring-banded patterns, whereas the right pane indicating the variation of the free energy density and radius of the ring-banded patterns with time. The model parameters used are (a)$\gamma/A = 0.65, \xi_\psi/\xi_\phi = 1.20$, $\alpha = 0.175, \beta = 1 + \alpha, \chi = 1.0, W/A = 1.0, \xi_\phi^2/\lambda_D^2 = 5.0$ and (b)$\gamma/A = 1.0, \xi_\psi/\xi_\phi = 0.3, \alpha = -0.1, \beta = 0, \chi = 1.0, W/A = 2.0, \xi_\phi^2/\lambda_D^2 = 20.0$. The time step is chosen as $dt = 0.01$.

In the case of $\beta = 0$ corresponding to the continuous phase transition, similar ring-banded patterns of the order parameters ϕ and ψ were found as shown in the left and middle panes of figure 4.6 (b) respectively. However, in this case, the system exhibits a noisy linear variation of the radius of the ring-banded pattern with time, and the free energy density also decreases smoothly with time, as shown in the right pane of figure 4.6(b). Therefore, the rhythmic growth of the ring-banded patterns was not found in this case. It should be noted that the coefficient (β) of the cubic term of the order parameter ψ in the free energy density determines the nature of the phase transition. Therefore, the order of the underlying phase transition can affect the growth dynamics and, even though they give rise to apparently similar-looking ring-banded patterns.

The formation of the ring-banded pattern can be understood from the TDGL equations as follows. The ring-banded pattern starts to grow from a seed (where $\psi > 0$) from the center. Subsequently, ψ at the seed increases to minimize the free energy of the system. This increase in ψ at the seed tends to enhance the conserved order parameter ϕ due to their bi-linear coupling. The order parameter ϕ decreases around the seed to obey the conservation rule. A sufficient reduction of ϕ produces a region of lower ψ due to the same bi-linear coupling. In turn, this lower region promotes the building of another region corresponding to higher values of ϕ and ψ. Thus, the growth continues in a repetitive fashion and produces the ring-banded structure.

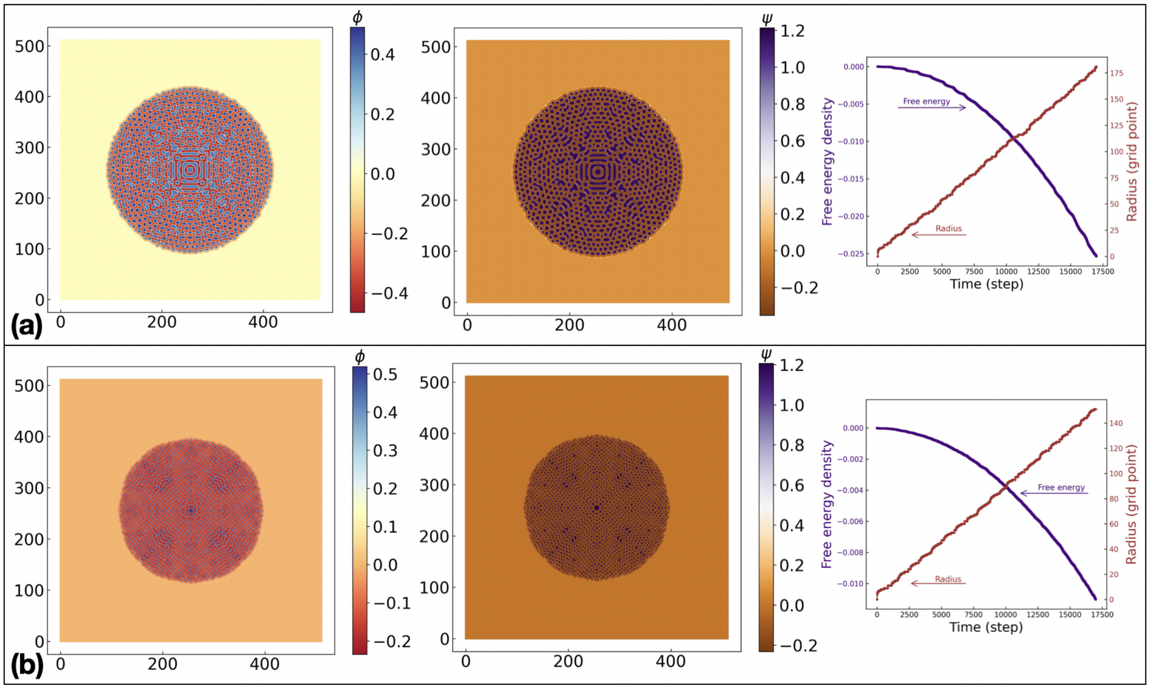

Figure 4.7: The left and middle panes representing the color-coded variation of the order parameters ϕ and ψ for the broken ring patterns, whereas the right pane indicating the variation of the free energy density and radius of the broken ring patterns with time. The model parameters used are (a) $\gamma/A = 0.55, \xi_\psi/\xi_\phi = 0.75$, and (b)$\gamma/A = 0.5, \xi_\psi/\xi_\phi = 0.45$ where $\alpha = 0.175, \beta = 1+\alpha, \chi = 1.0, W/A = 1.0$, and $\xi_\phi^2/\lambda_D^2 = 5.0$. The time step is chosen as $dt = 0.01$.

The ring-banded patterns are not the only patterns found in this system. More complex patterns were found depending on the model parameters. Figure 4.7 shows two such more complex broken ring patterns for certain values of the model parameters. For these values of the model parameters, most of the rings of the patterns break up into small domains, creating large interfacial areas, and hence, the azimuthal symmetry of the ring-banded pattern is lost. We found that the more complex patterns occur close to $\epsilon = 0$, which may be the manifestation of the singularity of the TDGL model [28]. The size of the growth front increases with time in a noisy staircase-type manner where the free energy density can show either a noisy rhythmic or a smooth non-linear relationship with time, as shown in the right panes of figure 4.7. Similar types of broken ring patterns have also been found in polymer blend system [29].

It is found that for some parameter values, the system depicts continuous patterns, as shown in figure 4.8. In the continuous pattern, the initial seed continuously increases its size. A circular interface separates two phases corresponding to $\psi = 0$ and $\psi = 1$. The conserved order parameter ϕ is almost zero everywhere. Both the radius of the domain and the free energy density of the system vary smoothly with time, giving rise to the non-rhythmic growth dynamics as shown in the right pane of figure 4.8. This type of continuous pattern has been found experimentally in a polymer blend system [31].

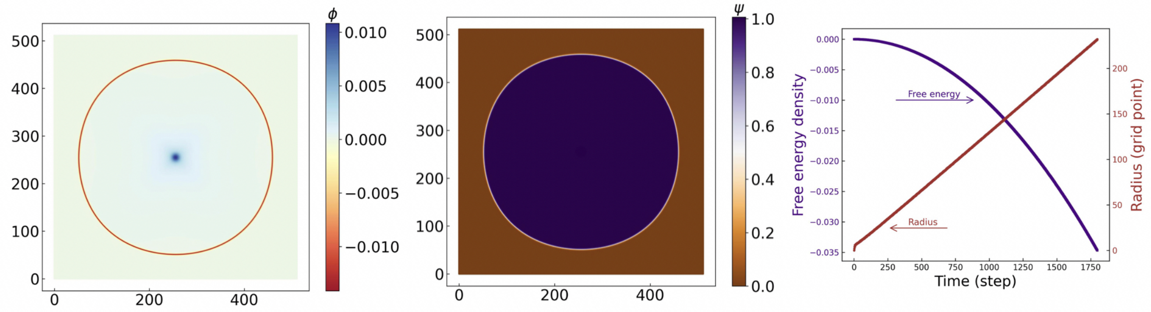

Figure 4.8: The left and middle panes representing the color-coded variation of the order parameters ϕ and ψ for a continuous pattern, whereas the right pane indicating the variation of the free energy density and radius of the continuous pattern with time. The model parameters used are $\gamma/A = 0.50, \xi_\psi/\xi_\phi = 1.80, \alpha = 0.175, \beta = 1+\alpha, \chi = 1.0, W/A = 1.0$, and $\xi_\phi^2/\lambda_D^2 = 5.0$. The time step is chosen as $dt = 0.01$.

It should be noted that the radius of these three types of patterns grows on average linearly with time. Therefore, the free energy density decreases on average quadratically with time as the free energy density is proportional to the area of the patterns. It is well known that the linear growth dynamics and circular growth fronts are the essential properties of spherulitic growth in a quasi-two-dimensional system. So, the ring banded, broken ring, and continuous patterns are often associated with the experimentally observed spherulitic structures [27–29, 31].

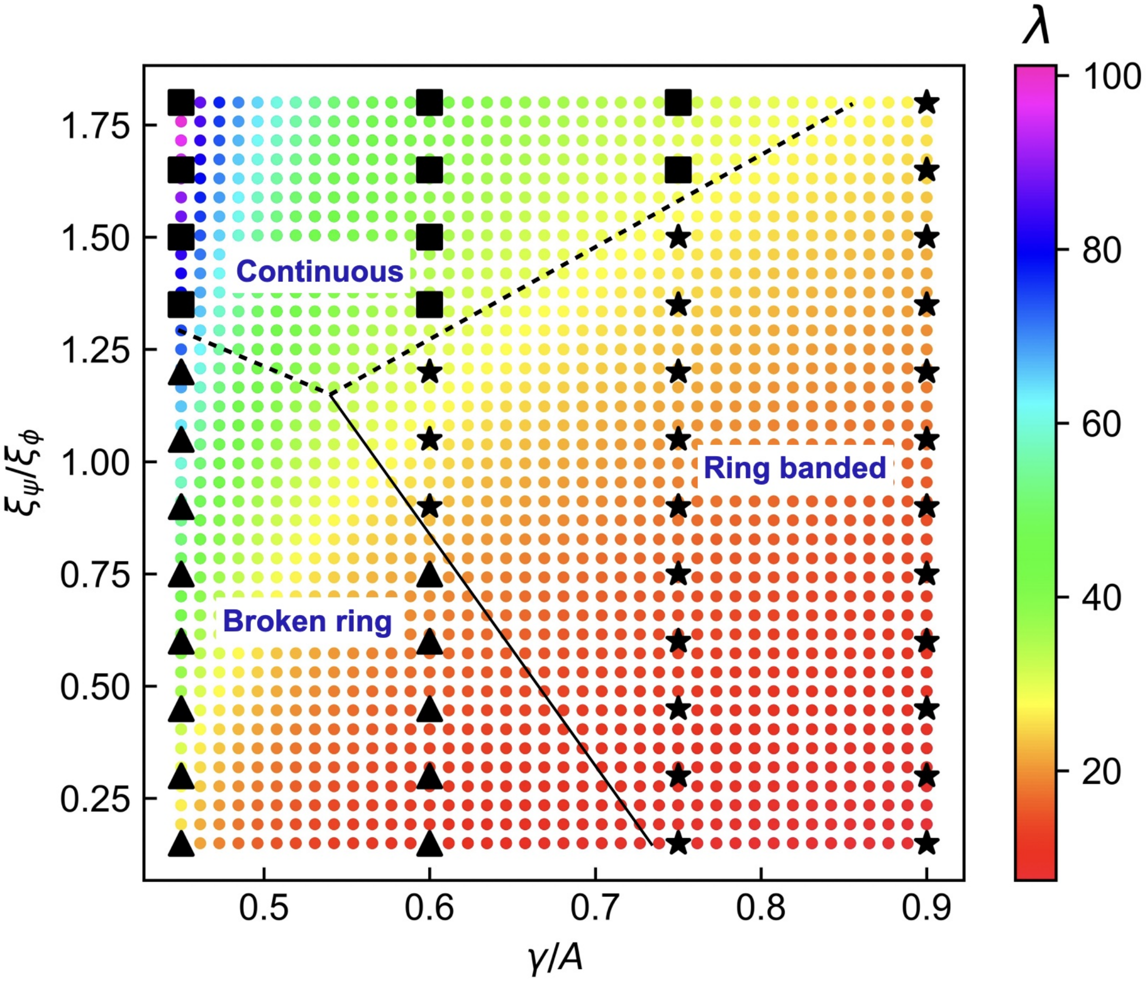

Figure 4.9: The stability diagram in the γ/A - ξ_ψ/ξ_ϕ parameter plane representing the regions of the stability of the different patterns such as ring banded, broken ring and continuous patterns for the model parameters $\alpha = 0.175, \beta = 1 + \alpha, \chi = 1.0, W/A = 1.0$ and $\xi_\phi^2/\lambda_D^2 = 5.0$. The color bar denotes the fastest-growing instability length scale λ obtained from LSA. The dotted and dashed lines are schematically drawn to represent the stability boundaries.

The stability of these patterns in the parameter plane of γ/A and ξ_ψ/ξ_ϕ is shown in figure 4.9. The wavelength λ corresponding to the fastest-growing mode obtained from LSA is also indicated by a color map in this figure. For high values of ξ_ψ/ξ_ϕ, it is found that the circular domain grows continuously without any undulation of the order parameters (see figure 4.8). In this region of the parameter plane, the wavelength λ corresponding to the fastest-growing mode obtained from LSA tends to infinity as expected. The broken ring patterns, as shown in figure 4.7 are observed for low values of both the parameters ξ_ψ/ξ_ϕ and γ/A. The ring-banded patterns are stable for high values of γ/A but for moderate values of ξ_ψ/ξ_ϕ. The values of the wavelength λ corresponding to the broken ring and ring-banded patterns are found to be of the same order, and our LSA does not differentiate these patterns. The stability boundaries of these patterns are schematically indicated by the dashed and a continuous lines in figure 4.9.

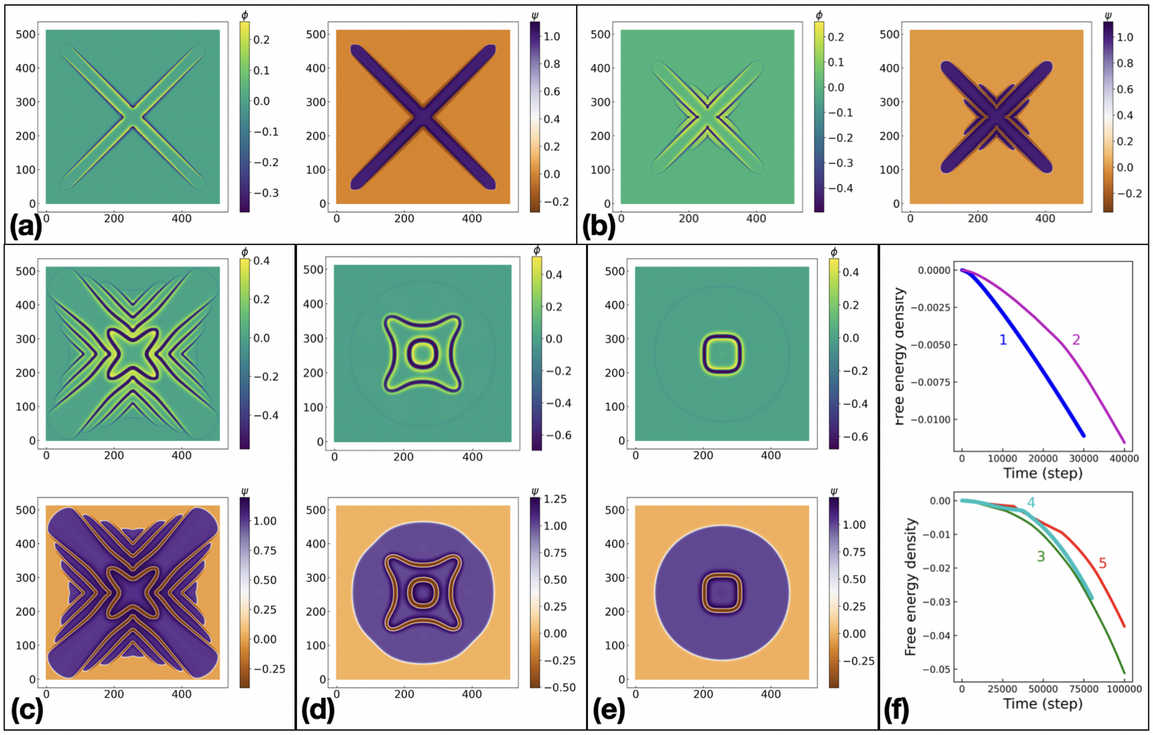

Figure 4.10: The color-coded representation of the order parameters ϕ and ψ for the intermediate patterns. The model parameters used are (a)$\gamma/A = 0.45, \xi_\psi/\xi_\phi = 1.25$,(b) $\gamma/A = 0.5, \xi_\psi/\xi_\phi = 1.15$,(c)$\gamma/A = 0.6, \xi_\psi/\xi_\phi = 1.27$, (d) $\gamma/A = 0.75, \xi_\psi/\xi_\phi = 1.55$, and (e) $\gamma/A = 0.75, \xi_\psi/\xi_\phi = 1.56$ where $\alpha = 0.175, \beta = 1 + \alpha, \chi = 1.0, W/A = 1.0$, and $\xi_\phi^2/\lambda_D^2 = 5.0$. (f) The variation of the free energy density of these intermediate patterns with time. The graphs 1, 2, 3, 4 and 5 correspond to the patterns (a),(b),(c),(d) and (e) respectively. The time step is chosen as $dt = 0.001$.

However, near these stability boundaries, very different intermediate types of patterns are observed as one crosses these boundary lines. For example, figure 4.10 shows some of these intermediate patterns near the dashed line of figure 4.9. Most of these patterns are found to grow with a fourfold symmetry. For the parameter $\gamma/A = 0.45$

and $\xi_\psi/\xi_\phi = 1.25$, a crossed pattern is observed as shown in figure 4.10(a). It is found that the length of the arms of this pattern continues to grow with time, whereas the breadth remains almost constant. The free energy density of the system linearly decreases at long times, as shown by the graph 1 of figure 4.10(f) which implies the linear growth of the arms of the crossed pattern. Remaining close to the dashed line but with slightly higher values of γ/A, the crossed pattern with additional structures is found as shown in figure 4.10(b). In this case, the graph 2 of figure 4.10(f) shows the decrease in the free energy density with time. The change in the slope of the linear variation is associated with the formation of these additional structures. For even higher values of γ/A, we find a complex pattern morphology, as shown in figure 4.10(c). For this pattern, it is found that the free energy density decreases quadratically with time, as can be seen in the graph 3 of figure 4.10(f). For relatively large values of γ/A, the circular domain grows continuously with a central pattern as shown in figure 4.10(d) and (e). It is found that small change in the model parameters leads to noticeable differences in these patterns. For these patterns, the free energy density also decreases quadratically with time, as can be seen in the graphs 4 and 5 of figure 4.10(f). The quadratic decrease in the free energy density can be associated with the quadratic increment of the area of the pattern with time. Therefore, the size of these intermediate patterns grows linearly with time, similar to the spherulitic growth. However, these intermediate patterns have not yet been observed in any experimental system, and it will be interesting to explore these theoretical predictions in future studies.

4.5 Summary

We have studied the pattern formation using a time-dependent Ginzburg-Landau theory consisting of a conserved and a non-conserved order parameters. The linear stability analyses of the model have been performed for different values of the model parameters. It is found that the wavelength corresponding to the faster-growing mode strongly depends on some model parameters. We have also performed numerical computations to find the solutions of the fully non-linear equations. Depending on the values of the model parameters, the simulations exhibit mostly ring-banded, broken-ring, and continuous patterns. The radius of these patterns increases on average linearly with time. But for some parameter values, the radius of the pattern is found to increase in a step-like fashion superposed on the average linear growth. This type of growth dynamics is known as rhythmic growth. We have also constructed a stability diagram of these patterns on a parameter plane of the model. Furthermore, various intermediate patterns are found near the stability boundaries of these patterns.

Bibliography

[1] A. G. Shtukenberg, Y. O. Punin, E. Gunn, and B. Kahr, Chemical Reviews **112**, 1805 (2012), pMID: 22103741, `https://doi.org/10.1021/cr200297f`, URL `https://doi.org/10.1021/cr200297f`.

[2] M. Parsa, S. Harmand, and K. Sefiane, Advances in Colloid and Interface Science **254**, 22 (2018), ISSN 0001-8686, URL `https://www.sciencedirect.com/science/article/pii/S0001868617304517`.

[3] M. J. Aschwanden, F. Scholkmann, W. Béthune, W. Schmutz, V. Abramenko, M. C. M. Cheung, D. Müller, A. Benz, G. Chernov, A. G. Kritsuk, et al., Space Science Reviews **214**, 55 (2018), ISSN 1572-9672, URL `https://doi.org/10.1007/s11214-018-0489-2`.

[4] M. C. Cross and P. C. Hohenberg, Rev. Mod. Phys. **65**, 851 (1993), URL `https://link.aps.org/doi/10.1103/RevModPhys.65.851`.

[5] A. M. Turing, Philosophical Transactions of the Royal Society of London. Series B, Biological Sciences **237**, 37 (1952), `https://royalsocietypublishing.org/doi/pdf/10.1098/rstb.1952.0012`, URL `https://royalsocietypublishing.org/doi/abs/10.1098/rstb.1952.0012`.

[6] L. Gránásy, T. Pusztai, T. Börzsönyi, G. Tóth, G. Tegze, J. Warren, and J. Douglas, Journal of Materials Research **21**, 309–319 (2006).

[7] N. Moelans, B. Blanpain, and P. Wollants, Calphad **32**, 268 (2008), ISSN 0364-5916, URL `https://www.sciencedirect.com/science/article/pii/S0364591607000880`.

[8] H. Emmerich, H. Löwen, R. Wittkowski, T. Gruhn, G. I. Tóth, G. Tegze, and L. Gránásy, Advances in Physics **61**, 665 (2012), `https://doi.org/10.1080/00018732.2012.737555`, URL `https://doi.org/10.1080/00018732.2012.737555`.

[9] R. Kobayashi, Physica D: Nonlinear Phenomena **63**, 410 (1993), ISSN 0167-2789, URL `https://www.sciencedirect.com/science/article/pii/016727899390120P`.

[10] Q. Du, C. Liu, and X. Wang, Journal of Computational Physics **212**, 757 (2006), ISSN 0021-9991, URL `https://www.sciencedirect.com/science/article/pii/S0021999105003566`.

[11] B. Crist and J. M. Schultz, Progress in Polymer Science **56**, 1 (2016), ISSN 0079-6700, URL `https://www.sciencedirect.com/science/article/pii/S0079670015001288`.

[12] B. Lotz and S. Z. Cheng, Polymer **46**, 577 (2005), ISSN 0032-3861, URL `https://www.sciencedirect.com/science/article/pii/S003238610400713X`.

[13] J. L. Hutter and J. Bechhoefer, Journal of Crystal Growth **217**, 332 (2000), ISSN 0022-0248, URL `https://www.sciencedirect.com/science/article/pii/S0022024800004796`.

[14] J. H. Magill, Journal of Materials Science **36**, 3143 (2001), ISSN 1573-4803, URL `https://doi.org/10.1023/A:1017974016928`.

[15] H. D. Keith and F. J. Padden, Journal of Applied Physics **34**, 2409 (1963), `https://doi.org/10.1063/1.1702757`, URL `https://doi.org/10.1063/1.1702757`.

[16] L. Gránásy, T. Pusztai, G. Tegze, J. A. Warren, and J. F. Douglas, Phys. Rev. E **72**, 011605 (2005), URL `https://link.aps.org/doi/10.1103/PhysRevE.72.011605`.

[17] A. Fang and M. Haataja, Phys. Rev. E **92**, 042404 (2015), URL `https://link.aps.org/doi/10.1103/PhysRevE.92.042404`.

[18] P. M. Chaikin and T. C. Lubensky, *Hydrodynamics* (Cambridge University Press, 1995), p. 417–494.

[19] J. W. Cahn and J. E. Hilliard, The Journal of Chemical Physics **28**, 258 (1958), `https://doi.org/10.1063/1.1744102`, URL `https://doi.org/10.1063/1.1744102`.

[20] H. Tanaka, Journal of Physics: Condensed Matter **11**, L159 (1999), URL `https://doi.org/10.1088/0953-8984/11/15/005`.

[21] H. Tanaka, Phys. Rev. E **62**, 6968 (2000), URL `https://link.aps.org/doi/10.1103/PhysRevE.62.6968`.

[22] R. Kurita and H. Tanaka, The Journal of Chemical Physics **126**, 204505

(2007), `https://doi.org/10.1063/1.2735625`, URL `https://doi.org/10.1063/1.2735625`.

[23] A. A. Wheeler, W. J. Boettinger, and G. B. McFadden, Phys. Rev. A **45**, 7424 (1992), URL `https://link.aps.org/doi/10.1103/PhysRevA.45.7424`.

[24] K. R. Elder, F. m. c. Drolet, J. M. Kosterlitz, and M. Grant, Phys. Rev. Lett. **72**, 677 (1994), URL `https://link.aps.org/doi/10.1103/PhysRevLett.72.677`.

[25] D. Zhou, A.-C. Shi, and P. Zhang, The Journal of Chemical Physics **129**, 154901 (2008), `https://doi.org/10.1063/1.2992530`, URL `https://doi.org/10.1063/1.2992530`.

[26] F. G. Segura-Fernández, E. F. Serrato-García, J. E. Flores-Calderón, and O. Guzmán, Frontiers in Physics **9** (2021), ISSN 2296-424X, URL `https://www.frontiersin.org/article/10.3389/fphy.2021.636288`.

[27] T. Kyu, H.-W. Chiu, A. J. Guenthner, Y. Okabe, H. Saito, and T. Inoue, Phys. Rev. Lett. **83**, 2749 (1999), URL `https://link.aps.org/doi/10.1103/PhysRevLett.83.2749`.

[28] S. Ghosh, D. Patra, and A. Roy, Phys. Rev. Materials **6**, 053401 (2022), URL `https://link.aps.org/doi/10.1103/PhysRevMaterials.6.053401`.

[29] H. Xu, H.-W. Chiu, Y. Okabe, and T. Kyu, Phys. Rev. E **74**, 011801 (2006), URL `https://link.aps.org/doi/10.1103/PhysRevE.74.011801`.

[30] D. Wang, T. Shi, J. Chen, L. An, and Y. Jia, The Journal of Chemical Physics **129**, 194903 (2008), `https://doi.org/10.1063/1.2985652`, URL `https://doi.org/10.1063/1.2985652`.

[31] R. Mehta and T. Kyu, Journal of Polymer Science Part B: Polymer Physics **42**, 2892 (2004), `https://onlinelibrary.wiley.com/doi/pdf/10.`

1002/polb.20151, URL `https://onlinelibrary.wiley.com/doi/abs/10.1002/polb.20151`.

Chapter 5

Formation of banded spherulite by rhythmic growth

In the previous chapter, a phase field model with a conserved and a non-conserved order parameters has been discussed. In this model, the dynamics of the order parameters are governed by the time-dependent Ginzburg-Landau model C equations. We have shown that various types of patterns can form depending on the model parameters. We have employed this model to account for the banded spherulitic growth observed experimentally in our laboratory for the liquid crystalline compound 8OCB during its crystallization from the smectic A phase. In this chapter, we show that this model can describe the banded spherulitic growth observed in this system. This is the first report of the rhythmic growth-assisted banded spherulite formation in a small molecular system.

5.1 Introduction

Primarily, during solidification, a solid phase, after nucleation from its melts, starts to grow anisotropically and attains a faceted growth front. This faceted growth front

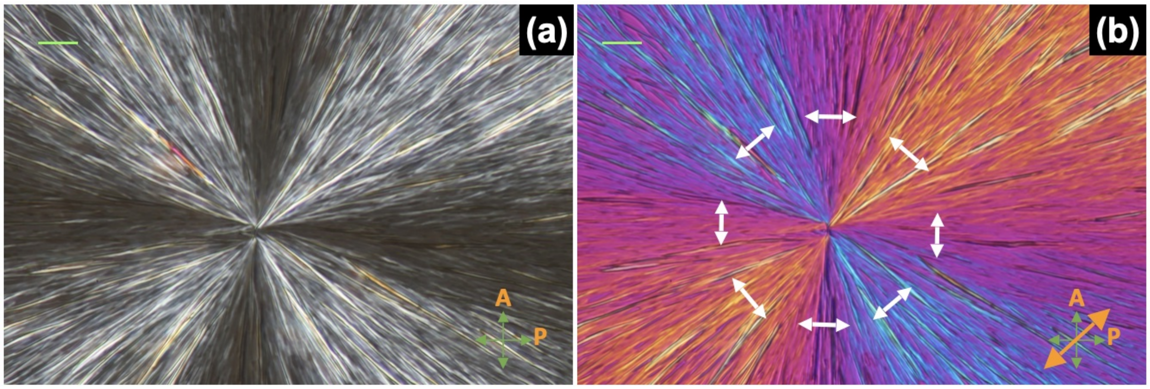

Figure 5.1: The polarised optical microscope (POM) images of a continuous spherulite of 8OCB (a) between crossed polarisers and (b) with a λ-plate inserted in the optical path in addition to the crossed polarisers. The direction of the major refractive index in the sample plane is denoted by white double-headed arrows around the seed. The dark arms of the Maltese cross parallel to the polarisers remain invariant in the rotation of the sample between the crossed polarisers.

results as a consequence of the discrete point symmetry of the underlying crystal structure. In contrast, some materials are found to exhibit a spherical growth front during crystallization. This spherical growth front is thought to arise due to the polycrystalline aggregated structures of the underlying solid phase. These self-assembled polycrystalline structures are called spherulites. Initially, the spherulites were known as "circular crystals" for their circular boundary in quasi-two dimensional geometry, which was renamed later to spherulite [1]. The spherulitic growth has been commonly observed in nature during the solidification of a wide variety of materials such as polymers [2, 3], minerals [4–6], elements [7, 8], metals [9], and salts [10–12]. It is also often found in biological materials like coral skeletons [13], kidney stones [14], proteins [15–17], and urinary sediments [18]. A large number of experimental studies over a century confirm that the spherulitic growth morphology is often associated with the formation of many radially aligned fibrillar crystallites, which exhibit noncrystallographic branching to fill space during the growth [19]. This distinct characteristic of spherulites separates them from the other polycrystalline aggregates. Despite a large number of studies, the detailed theoretical as well as experimental understanding of the mechanism of this abundantly found natural growth phenomenon is still incomplete [9].

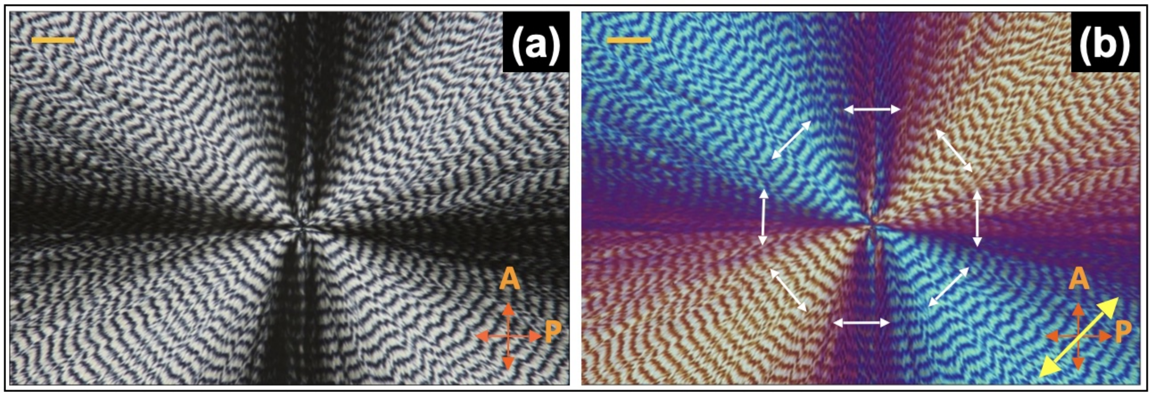

Figure 5.2: The polarised optical microscope (POM) images of a banded spherulite of 8OCB (a) between crossed polarisers and (b) with a λ-plate inserted in the optical path in addition to the crossed polarisers. The direction of the major refractive index in the sample plane is denoted by white double-headed arrows around the seed.

The polarising optical microscopic texture of a spherulite for 8OCB liquid crystal grown between two parallel glass plates is shown in figure 5.1. The texture exhibits a Maltese cross parallel to the crossed polarizers, which indicates the radial alignment of the crystalline fibrils. It has also been observed that the radius of the growing spherulite varies linearly with time.

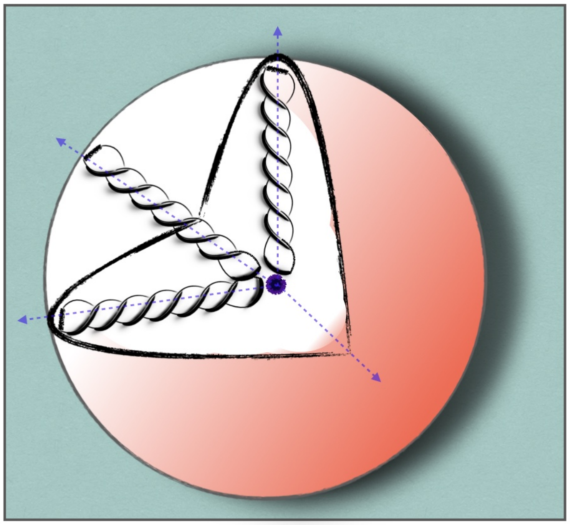

Figure 5.3: Schematic representation of coherent twisting of fibrils in a banded spherulite

In addition to these continuous spherulites, a kind of spherulite known as banded spherulite has also been observed [2, 3, 20–27]. A banded spherulite is accompanied by a spherically symmetric growth front and periodic radial variation of birefringence. This variation of birefringence in quasi-two-dimensional geometry produces concentric interference color bands when viewed through crossed polarizers. Figure 5.2 shows the texture of a banded spherulite for 8OCB liquid crystal between crossed polarizers. Over the past decades, a theoretical model with the coherent periodic twisting of radially aligned fibrillar crystallites has been proposed to account for these banded spherulites [2, 3]. The coherent periodic twisting of radially aligned fibrillar crystallites produces a periodic change of effective birefringence along the radial direction, giving rise to the concentric color bands observed in polarizing optical microscopic textures. Figure 5.3 schematically depicts banded spherulite with coherently twisted fibrillar structures. The twisting of the fibrils can arise due to several causes such as surface stress mismatch [2, 20], iso-chiral screw dislocation [28, 29], auto deformation [9], self-induced concentration or mechanical fields on growth kinetics [30], and topological defects [31]. The organized twisting of the fibrillar crystallites is considered to be a primary mechanism for the formation of the banded spherulites.

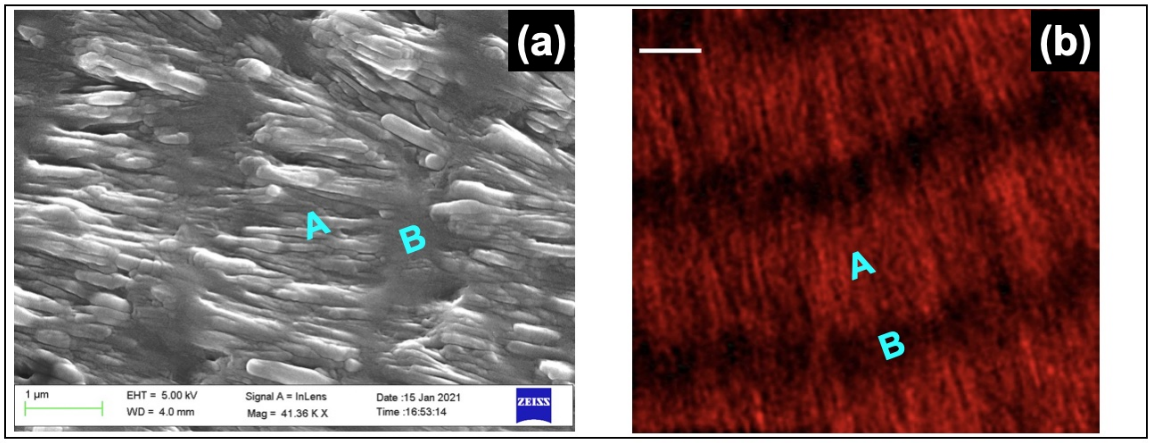

Figure 5.4: (a) The scanning electron microscopic image of a banded spherulitic region showing the presence of alternating fibrous nano-crystallite rich domains and amorphous domains. (b) The fluorescent image of a dye-doped banded spherulitic region. The regions marked "A" and "B" represent the concentric crystallite-rich and crystallite-poor bands, respectively.

Recently, we have reported detailed studies on the banded spherulitic growth of the solid phase for the small molecular rodlike liquid crystalline compound 8OCB [32]. The compound exhibits the banded spherulitic growth during the solidification from its Smectic A phase. The banded spherulitic domains were studied using a variety of experimental techniques such as polarising microscopy, Raman spectroscopy, Xray diffraction analysis, confocal microscopy, dielectric spectroscopy, and scanning electron microscopy (SEM) [32]. These studies reveal that the banded spherulitic domains are composed of two solid phases, namely, the fibrillar nano-crystallites and a solid amorphous phase. The existence of the two phases can be easily seen in the SEM micrograph as shown in figure 5.4. The crystallite-rich and crystallite-poor zones are marked as A and B, respectively, in this figure. The crystallite-rich zone is primarily associated with the higher density of radially aligned fibrillar nano-crystallites, whereas the crystallite-poor zone contains fewer fibrillar nano-crystallites and is mostly filled with the solid amorphous phase. The alternation of these concentric zones along the radial direction of the spherulite produces the radial undulation of the effective birefringence. This periodic variation of effective birefringence gives rise to the concentric interference color bands observed between crossed polarizers. It should be noted that the twisting of the fibrillar nano-crystallites was not observed in this system. Therefore, the coherent twisting model discussed above [2, 3, 9, 20, 28–31] is not suitable for the description of banded spherulite of this achiral liquid crystalline compound.

We, therefore, develop a time-dependent Landau-Ginzburg model C to account for the banded spherulitic growth observed in 8OCB liquid crystal. We have compared the periodicity obtained from the linear stability analysis (LSA) with the experimentally measured band spacing of the banded spherulite for different values of supercooling. The good agreement between the theoretical results and experimental data confirms the general validity of this model. We have also performed numerical studies of the full nonlinear equations to investigate the growth dynamics of the banded spherulite. The simulation results on this system show ring-banded pattern formation with rhythmic growth of the radius as a function of time. The computed band spacing obtained from simulations as a function of supercooling also agrees very well with the experimental findings. Interestingly, it is experimentally observed that the band spacing diverges at a particular supercooling when approaching this value from below. This divergence of band spacing has also been reported for some other materials [2]. However, the previous theoretical models for the banded spherulites did not account for this observation. For the first time, our model correctly captures this observation in both the LSA and simulations.

5.2 Model

We have developed a time-dependent Ginzburg-Landau (TDGL) model C for describing the banded spherulitic growth in the 8OCB liquid crystal. It is experimentally found in our system that the bands in the spherulite arise due to the alternating concentric crystallite-rich and crystallite-poor amorphous zones. Armed with this result, we define a conserved order parameter ϕ and a non-conserved order parameter ψ to describe the banded spherulitic growth using the TDGL model C. The conserved order parameter

$$\phi = \frac{\rho - \rho_0}{\rho_0}$$

describes the local deviation of density in these zones from the average density ρ_0 of the smectic A phase. Clearly, the order parameter ϕ is conserved given by the mathematical expression

$$\int_V \phi(\vec{r}, t) d^3\vec{r} = 0$$

where V denotes the volume of the system. On the other hand, the non-conserved order parameter ψ takes into account the local compositional difference between the nano-crystalline and amorphous solid phases of the system. Therefore, the non-conserved order parameter can be defined as

$$\psi = \frac{\rho_{nc} - \rho_a}{\rho_0}$$

where ρ_{nc}/ρ_0 and ρ_a/ρ_0 are the fractional densities of molecules in the nano crystalline and amorphous solid phase, respectively. The smectic phase with $\psi = 0$ undergoes a first-order transition to the spherulitic domain with $\psi \neq 0$.

The free energy density of the system in its smectic phase can be expressed as

$$f = \frac{A}{2}\phi^2 + \frac{1}{2}k_\phi|\nabla\phi|^2 + W\Big[\frac{\alpha(T)}{2}\psi^2 - \frac{1+\alpha(T)}{3}\psi^3 + \frac{1}{4}\psi^4\Big] + \frac{1}{2}k_\psi|\nabla\psi|^2 - \gamma\phi\psi. \quad (5.1)$$

The first two terms in equation 5.1 represent the free energy density corresponding to the order parameter ϕ. It is assumed that the conserved order parameter ϕ is non-critical across the transition to the spherulitic state, and only the terms up to the quadratic order are retained with the coefficients A and k_ϕ greater than zero.

The third and fourth terms describe the free energy density associated with the order parameter ψ accounting for the first-order phase transition from the smectic phase to the spherulitic state. The last term in equation 5.1 is the lowest order bilinear coupling between these order parameters.

Here, $0 \leq \alpha(T) \leq 1$ is the only temperature-dependent parameter driving this first-order transition. As usual in the Landau theory, the parameter $\alpha(T)$ is assumed to be linearly dependent on temperature as $\alpha = \delta(T - T_c)$. The melting temperature of 8OCB is 327.6 K, and the smectic phase is absolutely stable above this temperature. Hence, we have considered that α takes the maximum value one at this temperature $T_m = 327.6$ K. We have assumed the temperature $T_c = 273.1$ K denoting the lower limit of stability of the smectic phase which is difficult to find experimentally due to the large range of supercooling of the smectic phase. This temperature-dependent parameter becomes

$$\alpha(T) = (T - T_c)/(T_m - T_c)$$

where T_m and T_c are the melting temperature and supercooling limit of the smectic phase, respectively. We define the supercooling from the melting temperature T_m as $\Delta T = T_m - T$.

The free energy density given by equation 5.1 is similar to the free energy density discussed in the previous chapter (equation 4.1) with the model parameters $\beta = 1 + \alpha(T)$ and $\chi = 1$. Using this free energy density expression 5.1, the dimensionless form of the TDGL equations for the system can be written as

$$\frac{\partial \phi}{\partial t} = \nabla^2 \Big[\phi - \frac{\gamma}{A}\psi - \epsilon \nabla^2 \phi \Big] \tag{5.2}$$

$$\epsilon \frac{\partial \psi}{\partial t} = -\frac{\xi_\phi^2}{\lambda_D^2} \Big[\psi(\psi - 1)(\psi - \alpha) - \frac{\gamma}{W}\phi - \epsilon \frac{\xi_\psi^2}{\xi_\phi^2} \nabla^2 \psi \Big] \tag{5.3}$$

where $\epsilon = (\frac{\gamma^2}{WA} - \alpha)$ is a dimensionless parameter. The parameters $\xi_\phi = \sqrt{\frac{k_\phi}{A}}$,

$\xi_\psi = \sqrt{\frac{k_\psi}{W}}$ and $\lambda_D = \sqrt{\frac{A\Gamma_\phi}{\Gamma_\psi W}}$ have the dimension of length, where Γ_ϕ and Γ_ψ are two dynamical coefficients of the system. The detailed derivation of these equations, the linear stability analysis (LSA), and the finite-difference simulation scheme to solve these model equations are described in the previous chapter. Here, we present the results obtained from the equations 5.2 and 5.3 as a function of supercooling of the system and compare them with the experimental findings. A similar type of phase field model has been proposed to qualitatively account for the formation of the banded spherulite in the polymer blends [33, 34]. However, the exploration of these models in different systems and comparing the results with the experimental findings have not been undertaken.

5.3 Results and discussions

The linear stability analysis of the model equations was performed to determine modes which become unstable on increasing the supercooling of the SmA phase. Figure 5.5(a) shows the variation of growth rate σ as a function of the wave vector q for different values of the parameter α obtained from the linear stability analysis. The positive value of σ defines the instability mode with the wave vector q. As can be seen from figure 5.5(a), σ is positive for modes with wave vector q lying between zero and q_{max} and these unstable modes give rise to the banded spherulite in this system. Among these unstable modes, σ has the highest positive value for $q = q_c$ and this unstable mode will be most dominant during the growth of the banded spherulite. Figure 5.5(b) shows the variation of q_{max} and q_c with the parameter α obtained from LSA. Though q_c varies strongly with α, the q_{max} does not vary appreciably with it. The wavelength corresponding to the mode q_c is compared with the experimentally measured band spacing of the banded spherulite observed for our system. Figure 5.5(c) shows the experimentally measured band spacing and the theoretically computed band spacing obtained from the LSA and simulation as a function of supercooling. The theoretical result agrees well with the experimental data confirming the general validity of our model. Our theoretical results show good agreement with the experiments for the following choice of model parameters: $\gamma/A = 0.242$, $W/A = 0.1$, $\xi_\phi = 0.04$ μm, $\xi_\psi = 3.16\xi_\phi$, $\lambda_D = 1.41\xi_\phi$.

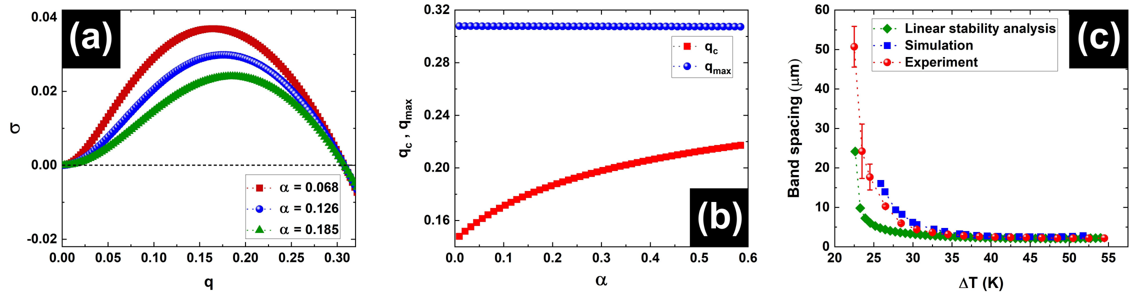

Figure 5.5: Effect of supercooling on banded spherulite. (a) The variation of growth rate σ with the wave vector q for different values of α. The modes in the wave vector range $0 < q < q_{max}$ are unstable. (b) The variation of q_{max} and q_c as a function of α. (c) Comparison between experimental, linear stability analysis and simulation results for the variation of band spacing with supercooling ΔT. The values of the parameters used for the theoretical model are $\gamma/A = 0.242$, $W/A = 0.1$, $\xi_\phi = 0.04$ μm, $\xi_\psi = 3.16\xi_\phi$, $\lambda_D = 1.41\xi_\phi$.

A general analytical method of finding solutions of the coupled nonlinear TDGL equations given by equations 5.2 and 5.3 is not known. These equations were solved numerically under no flux boundary condition using a finite difference method in two dimensions. The numerical solutions of the order parameters ϕ and ψ for a banded spherulite growing from a seed at the centre are shown in figure 5.6a and figure 5.6b, respectively (also see figure 5.7). The formation of the ring-banded structure is clearly observed as found experimentally. Figure 5.6c shows the graphical profiles of the order parameters along a radial direction of the spherulite. The order parameters vary periodically and in phase along the radial direction during the growth of the spherulite. This in-phase variation of the order parameters arises due to their bilinear coupling with $\gamma > 0$ in equation 5.1.

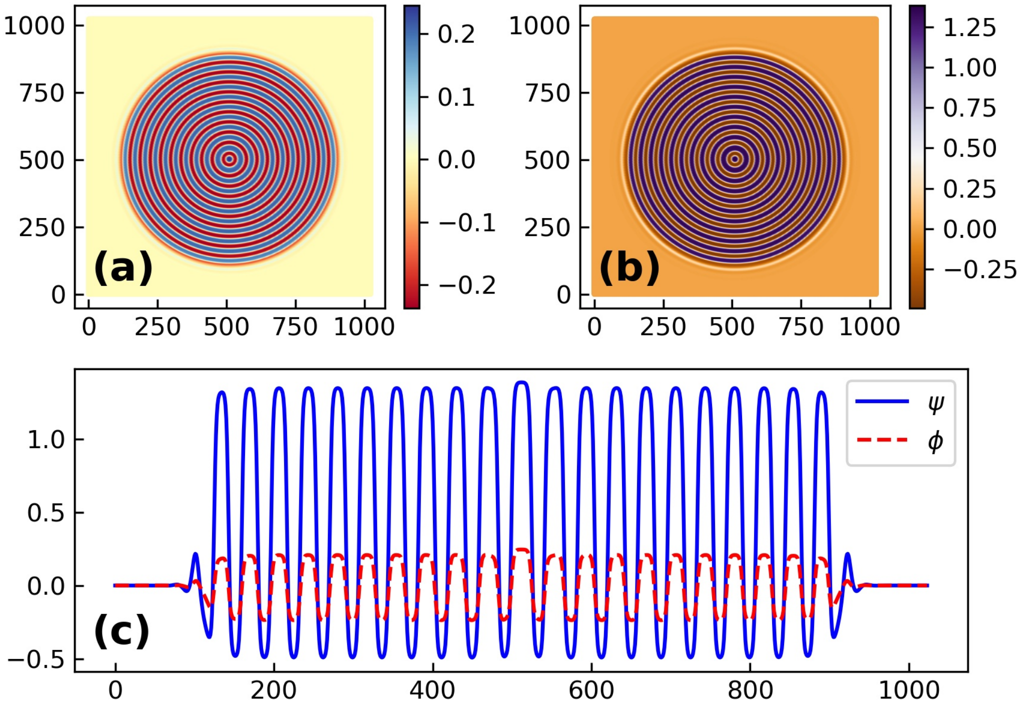

Figure 5.6: Simulated banded spherulite domain. The color-coded representation of the order parameters (a) ϕ and (b) ψ of a banded spherulite obtained from the numerical solution of the TDGL equations at $\Delta \mathrm{T} = 39.5$ K. The model parameters used are $\gamma/A = 0.242$, $W/A = 0.1$, $\zeta_\phi = 0.04$ μm, $\zeta_\psi = 3.16\zeta_\phi$, $\lambda_D = 1.41\zeta_\phi$, time step size $dt = 0.01$ and spatial step size $dx = dy = 1.0$. (c) The graphical profiles of ϕ and ψ along a radial axis of the simulated banded spherulite.

The formation of the banded spherulite can be understood from these numerical studies as follows. The banded spherulite grows from an initial nano-crystallite seed nucleated on sufficient supercooling of the SmA phase. The nano-crystallites have higher density compared to the amorphous state. Thus, the growth of this nano crystallite-rich domain leads to a decrease in density around it due to the depletion of the molecules. When this density decreases sufficiently; it promotes the formation of a crystallite-poor amorphous domain around the initial crystallite-rich domain. The growth of this crystallite-poor band in turn increases the density around its periphery and leads to the nucleation of another nano crystallite-rich band. The growth continues with the formation of alternating crystallite-rich and crystallite-poor bands in a periodic manner along the radial direction of the spherulite, as indicated in figure 5.6.

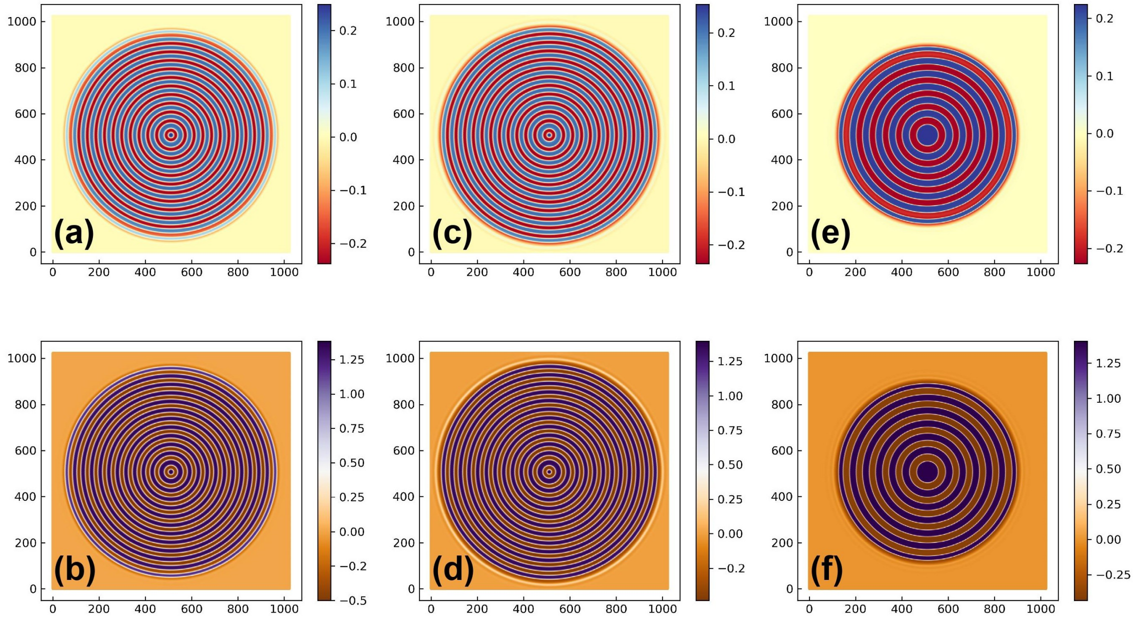

Figure 5.7: Simulated banded spherulite patterns for different values of supercooling. Numerical solutions of ϕ (upper row) and ψ (lower row) for different values of α (or ΔT). (a, b) $\alpha = 0.250$ (ΔT = 40.8 K) at 149999 time steps, (c, d) $\alpha = 0.300$ (ΔT = 38.1 K) at 199999 time steps, (e, f) $\alpha = 0.450$ (ΔT = 29.9 K) at 399999 time steps on a 1024×1024 square lattice.

The radius of the numerically simulated banded spherulite grows with time in a rhythmic fashion. The staircase type growth of dimensionless radius R with dimensionless time is shown in Figure 5.8. Each step represents the duration of a full band growth. Though this growth is nonlinear at each individual step, it shows, on average, a linear growth law with time. The growth velocity of the ring-banded pattern can be found from this linear relationship.

The spacing between two successive bands of the spherulite was also calculated from the numerical results for different values of supercooling ΔT. The numerically computed band spacing as a function of supercooling agrees very well with the experimental data, as shown in figure 5.5c. This figure also shows that the experimentally measured band spacing of the spherulite tends to diverge on approaching $\Delta\text{T} \sim 22.5$ K from above. Below this supercooling, only the formation of non-banded spherulites was observed experimentally. Both the LSA and numerical results account for this divergence of band spacing. This divergence arises from a singularity of the TDGL equations 5.2 and 5.3 with the parameter ϵ being zero. In this case, only the order parameter ϕ controls the dynamics of the system, and ψ is determined by the equation $\psi(\psi-1)(\psi-\alpha) = \frac{\gamma}{W}\phi$.

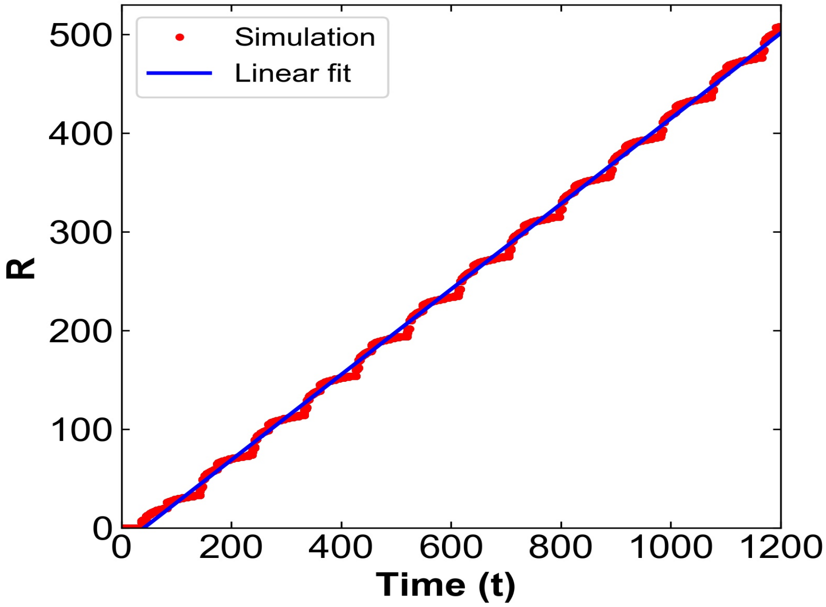

Figure 5.8: Rhythmic variation of banded spherulite radius. Numerically computed variation of radius R of the banded spherulite with time showing its rhythmic growth for $\alpha = 0.15$ ($\Delta\text{T} = 46.3$ K). The blue line shows the average linear growth of the spherulite with time. R and t are dimensionless quantities.

5.4 Summary

We have studied the banded spherulitic growth of the solid phase of a pure liquid crystalline compound from its SmA, deploying a phase-field model using the time-dependent Ginzburg-Landau theory. The model predicts that the banded spherulites are formed due to the rhythmic generation of concentric crystallite-rich and crystallite-poor amorphous zones. The variation of the band spacing as a function of the supercooling of the SmA phase calculated from our theoretical model agrees well with our experimental observations. Also, the model correctly accounts for the divergence of the band spacing experimentally observed in our system. The model predicts the rhythmic growth of the radius of the banded spherulite as a function of time.

Bibliography

[1] D. Brewster, Transactions of the Royal Society of Edinburgh **20**, 607–623 (1853).

[2] B. Crist and J. M. Schultz, Progress in Polymer Science **56**, 1 (2016), ISSN 0079-6700, URL `https://www.sciencedirect.com/science/article/pii/S0079670015001288`.

[3] B. Lotz and S. Z. Cheng, Polymer **46**, 577 (2005), ISSN 0032-3861, URL `https://www.sciencedirect.com/science/article/pii/S003238610400713X`.

[4] G. Lofgren, American Journal of Science **274**, 243 (1974), ISSN 0002-9599, `https://www.ajsonline.org/content/274/3/243.full.pdf`, URL `https://www.ajsonline.org/content/274/3/243`.

[5] R. Coish and L. A. Taylor, Earth and Planetary Science Letters **42**, 389 (1979), ISSN 0012-821X, URL `https://www.sciencedirect.com/science/article/pii/0012821X79900487`.

[6] R. J. Kirkpatrick, American Journal of Science **274**, 215 (1974), ISSN 0002-9599, `https://www.ajsonline.org/content/274/3/215.full.pdf`, URL `https://www.ajsonline.org/content/274/3/215`.

[7] I. Minkoff and W. C. Nixon, Journal of Applied Physics **37**, 4848 (1966), `https://doi.org/10.1063/1.1708149`, URL `https://doi.org/10.1063/1.1708149`.

[8] J. Bisault, G. Ryschenkow, and G. Faivre, Journal of Crystal Growth **110**, 889 (1991), ISSN 0022-0248, URL `https://www.sciencedirect.com/science/article/pii/002202489190647N`.

[9] A. G. Shtukenberg, Y. O. Punin, E. Gunn, and B. Kahr, Chemical Reviews **112**, 1805 (2012), pMID: 22103741, `https://doi.org/10.1021/cr200297f`, URL `https://doi.org/10.1021/cr200297f`.

[10] R. Beck and J.-P. Andreassen, Crystal Growth & Design **10**, 2934 (2010), `https://doi.org/10.1021/cg901460g`, URL `https://doi.org/10.1021/cg901460g`.

[11] Y. Oaki and H. Imai, Journal of the American Chemical Society **126**, 9271 (2004), pMID: 15281817, `https://doi.org/10.1021/ja048661+`, URL `https://doi.org/10.1021/ja048661+`.

[12] A. Thomas, E. Rosseeva, O. Hochrein, W. Carrillo-Cabrera, P. Simon, P. Duchstein, D. Zahn, and R. Kniep, Chemistry – A European Journal **18**, 4000 (2012), `https://chemistry-europe.onlinelibrary.wiley.com/doi/pdf/10.1002/chem.201102228`, URL `https://chemistry-europe.onlinelibrary.wiley.com/doi/abs/10.1002/chem.201102228`.

[13] C.-Y. Sun, M. A. Marcus, M. J. Frazier, A. J. Giuffre, T. Mass, and P. U. P. A. Gilbert, ACS Nano **11**, 6612 (2017), pMID: 28564539, `https://doi.org/10.1021/acsnano.7b00127`, URL `https://doi.org/10.1021/acsnano.7b00127`.

[14] U. Al-Atar, A. A. Bokov, D. Marshall, J. M. H. Teichman, B. D. Gates, Z.-G. Ye, and N. R. Branda, Chemistry of Materials **22**, 1318 (2010), `https://doi.org/10.1021/cm901751g`, URL `https://doi.org/10.1021/cm901751g`.

[15] P. S. Chow, X. Y. Liu, J. Zhang, and R. B. H. Tan, Applied Physics Letters **81**, 1975 (2002), `https://doi.org/10.1063/1.1506208`, URL `https://doi.org/10.1063/1.1506208`.

[16] J. E. Coleman, B. J. Allan, and B. L. Vallee, Science **131**, 350 (1960), `https://www.science.org/doi/pdf/10.1126/science.131.3397.350`, URL `https://www.science.org/doi/abs/10.1126/science.131.3397.350`.

[17] M. R. H. Krebs, C. E. MacPhee, A. F. Miller, I. E. Dunlop, C. M. Dobson, and A. M. Donald, Proceedings of the National Academy of Sciences **101**, 14420 (2004), ISSN 0027-8424, `https://www.pnas.org/content/101/40/14420.full.pdf`, URL `https://www.pnas.org/content/101/40/14420`.

[18] F. Catalina and L. Cifuentes, Science **169**, 183 (1970), `https://www.science.org/doi/pdf/10.1126/science.169.3941.183`, URL `https://www.science.org/doi/abs/10.1126/science.169.3941.183`.

[19] H. D. Keith and F. J. Padden, Journal of Applied Physics **34**, 2409 (1963), `https://doi.org/10.1063/1.1702757`, URL `https://doi.org/10.1063/1.1702757`.

[20] H. Keith and F. Padden, Polymer **25**, 28 (1984), ISSN 0032-3861, URL `https://www.sciencedirect.com/science/article/pii/0032386184902647`.

[21] A. G. Shtukenberg, X. Cui, J. Freudenthal, E. Gunn, E. Camp, and B. Kahr, Journal of the American Chemical Society **134**, 6354 (2012), pMID: 22413815, `https://doi.org/10.1021/ja300257m`, URL `https://doi.org/10.1021/ja300257m`.

[22] W. Pisula, M. Kastler, D. Wasserfallen, T. Pakula, and K. Müllen, Journal of the American Chemical Society **126**, 8074 (2004), pMID: 15225022, `https://doi.org/10.1021/ja048351r`, URL `https://doi.org/10.1021/ja048351r`.

[23] X. Cui, A. L. Rohl, A. Shtukenberg, and B. Kahr, Journal of the American Chemical Society **135**, 3395 (2013), pMID: 23425247, `https://doi.org/10.1021/ja400833r`, URL `https://doi.org/10.1021/ja400833r`.

[24] A. Shtukenberg, J. Freundenthal, E. Gunn, L. Yu, and B. Kahr, Crystal Growth & Design **11**, 4458 (2011), `https://doi.org/10.1021/cg200640g`, URL `https://doi.org/10.1021/cg200640g`.

[25] T.-F. Lin, R.-M. Ho, C.-H. Sung, and C.-S. Hsu, Chemistry of Materials **18**, 5510 (2006), `https://doi.org/10.1021/cm061666g`, URL `https://doi.org/10.1021/cm061666g`.

[26] J. L. Hutter and J. Bechhoefer, Phys. Rev. Lett. **79**, 4022 (1997), URL `https://link.aps.org/doi/10.1103/PhysRevLett.79.4022`.

[27] J. L. Hutter and J. Bechhoefer, Journal of Crystal Growth **217**, 332 (2000), ISSN 0022-0248, URL `https://www.sciencedirect.com/science/article/pii/S0022024800004796`.

[28] A. Toda, T. Arita, and M. Hikosaka, Polymer **42**, 2223 (2001), ISSN 0032-3861, URL `https://www.sciencedirect.com/science/article/pii/S0032386100004468`.

[29] D. Patel and D. Bassett, Polymer **43**, 3795 (2002), ISSN 0032-3861, URL `https://www.sciencedirect.com/science/article/pii/S0032386102001787`.

[30] J. M. Schultz, Polymer **44**, 433 (2003), ISSN 0032-3861, URL `https://www.sciencedirect.com/science/article/pii/S0032386102007243`.

[31] Y. Hatwalne and M. Muthukumar, Phys. Rev. Lett. **105**, 107801 (2010), URL `https://link.aps.org/doi/10.1103/PhysRevLett.105.107801`.

[32] S. Ghosh, D. Patra, and A. Roy, Phys. Rev. Mater. **6**, 053401 (2022), URL `https://link.aps.org/doi/10.1103/PhysRevMaterials.6.053401`.

[33] T. Kyu, H.-W. Chiu, A. J. Guenthner, Y. Okabe, H. Saito, and T. Inoue, Phys. Rev. Lett. **83**, 2749 (1999), URL `https://link.aps.org/doi/10.1103/PhysRevLett.83.2749`.

[34] H. Xu, H.-W. Chiu, Y. Okabe, and T. Kyu, Phys. Rev. E **74**, 011801 (2006), URL `https://link.aps.org/doi/10.1103/PhysRevE.74.011801`.

Chapter 6

Wrinkling of a thin sheet on a nematic substrate

Wrinkling instability commonly occurs in a unidirectionally compressed thin sheet floating on a fluid substrate. Here, we theoretically study the wrinkling instability of a unidirectionally compressed thin sheet floating on a nematic medium. We have minimized the total free energy of the system by assuming a sinusoidal undulation of the compressed thin sheet. The variation of the wave vector of the wrinkling pattern as a function of various model parameters has been explored. The model predicts that the periodicity of the pattern is always larger in the case of nematic substrate compared to its isotropic state. The wrinkling wavelength sensitively varies with the curvature elastic constant and the surface anchoring condition of the nematic. In contrast to the isotropic fluid substrate, it is found that the wrinkling periodicity depends on the amount of compression for the hybrid anchoring condition of the nematic director on the bounding surfaces.

6.1 Introduction

Wrinkling instabilities can occur in various systems [1–4], such as our brains, dry fruit skins, animal skins, flowers, on the crust of the earth, etc. These instabilities are of great importance not only from a fundamental viewpoint but also their technological applications [5–11]. Therefore, a lot of experiments have been carried out to gain better insights into the underlying mechanisms [2, 12–17]. Besides these experiments, a large number of theoretical studies have been performed to explain these instabilities [2, 18–20]. Most of the studies deal with a unidirectionally compressed thin sheet atop an isotropic fluid or elastic substrate [20–23].

An incompressible floating thin sheet atop an isotropic fluid develops wrinkles under unidirectional compression. The wrinkling wavelength (λ) obeys a relation $\lambda \sim (B/\rho g)^{1/4}$ where B, ρ and g are bending modulus of the thin sheet, the density of the isotropic liquid and the acceleration due to gravity, respectively. This wavelength does not depend on external stimuli such as temperature and electric field. Hence, the tunability of the wavelength is limited, and it is of great concern for technological applications. In this context, an anisotropic substrate such as nematic liquid crystal offers a way to couple the effect of these external drives.

In the uniaxial nematic phase, anisotropic rod-like molecules align their long axes on average to a particular direction, but their center of masses remain randomly distributed over space. Hence, the phase is intrinsically a fluid phase due to the absence of positional order [24]. However, the long-range orientational order gives rise to the anisotropic properties of the phase. The orientational order parameter is primarily dictated by the temperature of a system. The average orientation direction of the molecules is called director, which is apolar in nature. It is often denoted by a unit vector $\hat{n}$, and the apolar nature of the director implies $\hat{n} \leftrightarrow -\hat{n}$ symmetry of the nematic phase. The ground state of the nematic phase corresponds to the homogeneous alignment of the director $\hat{n}$ over the space. The deviation from this homogeneous orientation costs energy, but that can be easily induced by applying the electric or magnetic field and anchoring conditions of the director on the bounding surface.

Here, we consider the wrinkling instability of an incompressible thin sheet floating on a nematic liquid crystal when the sheet is subjected to unidirectional compression. The thickness of the sheet is assumed to be much less than its lateral dimensions. We have considered three essential free energies associated with the system, namely the bending energy of the thin sheet the gravitational and distortion energy of the nematic fluid. In the distortion-free energy, strong anchoring conditions of the nematic director field are assumed at the bounding surfaces. We minimize the total free energy of the system by assuming a sinusoidal undulation of the compressed thin sheet. A similar procedure has also been employed in earlier studies dealing with a thin sheet floating on an isotropic fluid substrate [19, 23]. The mode corresponding to the minimum free energy is considered to be the wave vector of the wrinkling pattern. We have determined the variation of the wave vector as a function of model parameters. The periodicity of the pattern in the case of the nematic substrate is always found to be higher than that of the isotropic state of the substrate, and this periodicity does not obey a simple relation in contrast to the system with an isotropic substrate. The periodicity of the pattern sensitively depends on the curvature elastic constants and the surface anchoring conditions of the nematic. It is also found that the wrinkling periodicity depends on the displacement due to the compression for the hybrid anchoring condition of the nematic substrate.

6.2 Free energy of the system

We have analytically derived the expression of three essential free energies associated with the system, namely the bending energy of the thin sheet and the gravitational and distortion energies of the nematic fluid. We present the detailed formalism as follows.

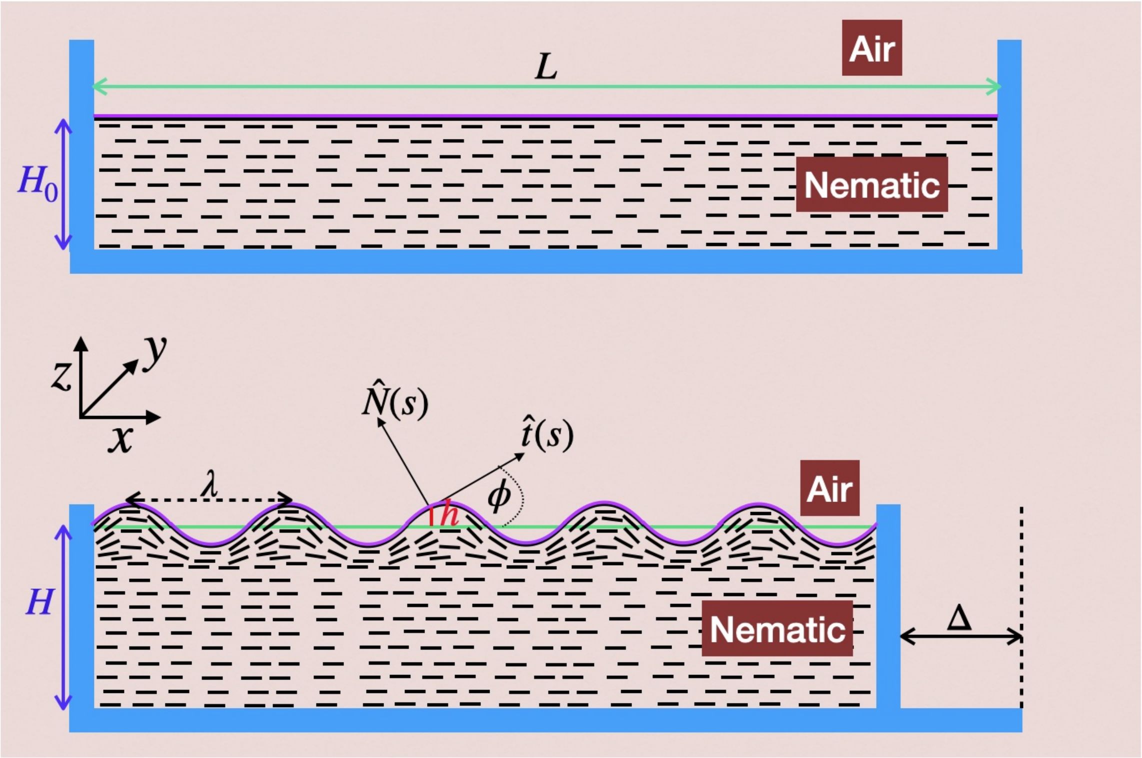

Figure 6.1: Schematic representation of an incompressible thin sheet floating on the nematic substrate. The sheet is subject to a unidirectional compression Δ along the x-axis. The deformation of the thin sheet is confined in the xz plane.

6.2.1 Bending energy of the thin sheet

We consider a thin elastic sheet of length L, thickness d ($L >> d$) and of infinite width floating on a nematic liquid crystal medium as shown in figure 6.1. The elastic constants of the sheet are given as stretching modulus $Y \sim Ed$ and bending modulus $B \sim Ed^3$, where E is Young's modulus. Hence, for the thin sheet, the energy corresponding to the bending mode is much less compared to the energy associated with the stretching mode, making it easier to be bent than to be stretched. Here, we assume the thin sheet to be incompressible in nature and consider only the bending energy associated with it when subjected to a unidirectional compression along the x axis. Due to the compression, the sheet is assumed to deform in the xz plane while remaining uniform along the y axis. The translational invariance along the y axis gives rise to a system that can be treated effectively as two-dimensional. Therefore, the cross-section of the deformed sheet can be expressed as a curve lying in the xz plane, and the height profile $h(s)$ can be parametrized by an arc length s varying from $-L/2$ to $L/2$. Then we can write $dx = ds\sqrt{1-\dot{h}^2}$ where $\dot{h}$ represents the derivative of h with respect to s. An arbitrary point $(x(s), h(s))$ on the curve also satisfies the following equations

$$\begin{aligned} \dot{x} &= \frac{dx}{ds} = \cos\phi(s) = \sqrt{1-\dot{h}^2} \\ \dot{h} &= \frac{dh}{ds} = \sin\phi(s) \\ \ddot{h} &= \cos\phi\frac{d\phi}{ds} = \cos\phi\dot{\phi} = \dot{\phi}\sqrt{1-\dot{h}^2} \end{aligned}$$

where ϕ is the angle made by the local tangent vector $\hat{t}$ with the x axis. The bending energy of the sheet per unit width can be written as $F_B = \frac{B}{2}\int\frac{ds}{R^2}$ where R is the local radius of curvature at the point (x, h). The radius of curvature at a point is given by $R = \frac{1}{|\frac{d\hat{t}}{ds}|} = \frac{ds}{d\phi} = \frac{\sqrt{1-\dot{h}^2}}{\ddot{h}}$. Therefore, the bending energy of the thin sheet per unit length (along the y-axis) can be expressed as

$$F_B = \frac{B}{2}\int_{-\frac{L}{2}}^{\frac{L}{2}} ds \frac{\ddot{h}^2}{1-\dot{h}^2} \tag{6.1}$$

The total displacement Δ due to the compression is given by

$$\Delta = L - \int dx = \int_{-\frac{L}{2}}^{\frac{L}{2}} ds(1 - \sqrt{1 - \dot{h}^2}), \tag{6.2}$$

which expresses the incompressibility constraint of the thin sheet assumed in the model.

6.2.2 Gravitational energy associated with the height modulation

The sheet is initially assumed to be flat at height H_0 from the bottom surface of the nematic medium as shown in figure 6.1. The unidirectional compression of the sheet gives rise to a height modulation of the nematic medium. The height of the medium at an arbitrary point is given by $H + h$ where H is the average height of the nematic medium after the compression and h denotes the modulation of height about H. The conservation of total volume due to the incompressibility of the nematic medium leads to the constraint $H(L - \Delta) = H_0 L$, which implies $\int h(s)ds = 0$. The change in the average height of the liquid medium from the initial height is given by $H - H_0$. The rising of the liquid medium costs the gravitational potential energy. The gravitational potential energy per unit area corresponding to the height increment $H + h - H_0$ of the liquid column can be written as $\int_0^{H+h-H_0} \rho g z dz = \rho g (H + h - H_0)^2/2$, where ρ and g are the density of the liquid medium and the acceleration due to gravity, respectively [25]. Therefore, the gravitational energy cost per unit length due to compression is given by

$$\begin{aligned} F_g &= (\rho g/2) \int_0^{L-\Delta} (H + h - H_0)^2 dx \\ &= \rho g (L - \Delta)(H - H_0)^2/2 + (\rho g/2) \int h^2 dx. \end{aligned}$$

The first part of the above energy expression corresponds to the average height change of the nematic medium due to the compression, and it does not depend on the height profile h of the thin sheet. Hence, it does not contribute to the determination of the height profile h by minimization of the total free energy. Therefore, the gravitational potential energy of the system is considered as

$$F_g = \int_0^{L-\Delta} \frac{\rho g}{2} h^2 dx = \int_{-\frac{L}{2}}^{\frac{L}{2}} ds \frac{\rho g}{2} h^2 \sqrt{1-\dot{h}^2}. \tag{6.3}$$

6.2.3 LC energy

The orientational order parameter of a uniaxial nematic phase can be defined by a symmetric traceless second rank tensor $Q_{\alpha\beta} = S(n_\alpha n_\beta - \delta_{\alpha\beta}/3)$ where $\alpha, \beta = x, y, z$ are indices referring to the laboratory frame and $\delta_{\alpha\beta}$ is the Kronecker delta. The scalar order parameter S represents the degree of orientation of the molecules and generally varies with the temperature. Far from the isotropic to the nematic transition temperature, the order parameter S tends to a saturated value. Hence, it can be considered as constant at these lower temperatures. The uniform orientational order corresponds to the ground state of the system. Therefore, the slow variation of the director $\hat{n}(\vec{r})$ in space costs energy. The energy cost associated with the director modulation can be described by Oseen-Frank free energy

$$F[\hat{n}] = \int \frac{1}{2}\left[K_1(\nabla \cdot \hat{n})^2 + K_2(\hat{n}.\nabla \times \hat{n})^2 + K_3(\hat{n} \times \nabla \times \hat{n})^2\right] d^3x. \tag{6.4}$$

The constants K_1, K_2, and K_3 are known as splay, twist, and bend elastic constants of the nematic medium, respectively [24].

We now derive the expression for the nematic distortion-free energy during the compression of the thin sheet floating on the nematic medium. We choose the boundary conditions for the director $\hat{n}$ underneath the elastic sheet to be either homeotropic

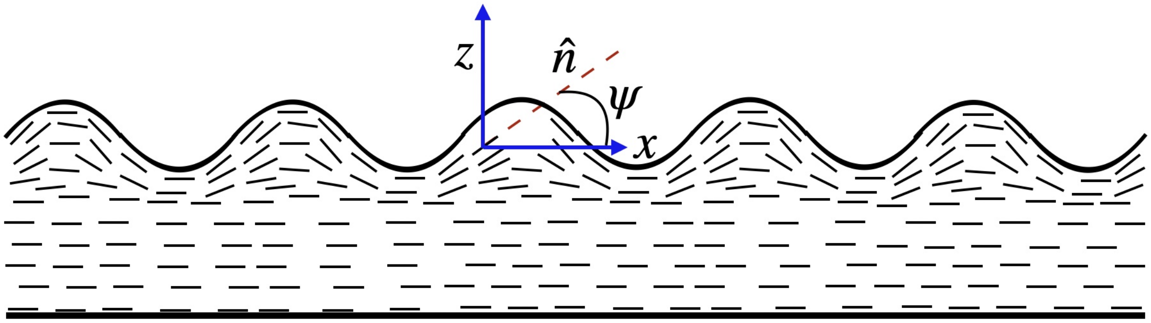

Figure 6.2: Schematic representation of the nematic director field.

(i.e., perpendicular to the sheet) or parallel to the sheet in the xz plane. Similarly, we also assume strong anchoring of the director $\hat{n}$ at the bottom surface of the nematic medium to be planar. In our model, we assume that the director field in the nematic medium remains in the xz plane only. In this case, the director $\hat{n} = (\cos\psi, 0, \sin\psi)$ where ψ is the angle between the director $\hat{n}$ and the x axis. Assuming one constant approximation ($K_1 = K_2 = K_3 = K$), the elastic deformation free energy per unit length can be written as

$$F_{LC}[\psi] = \int\int \frac{K}{2}\left|\nabla\psi\right|^2 dxdz. \tag{6.5}$$

The minimization of the above free energy functional provides the Laplace equation

$$\nabla^2\psi = \partial_x^2\psi + \partial_z^2\psi = 0. \tag{6.6}$$

The solutions of this equation determine the minimum energy configuration of the director field for given boundary conditions. The general solution of the equation 6.6 can be written as

$$\psi(x,z) \quad = \quad (A\cos mx + B\sin mx)(Ce^{mz} + De^{-mz}) \tag{6.7}$$

where A, B, C, D are dimensionless constants and the constant m has the dimension of length^{-1}.

For homogeneous planar alignment of the director at the bottom surface of the nematic medium, i.e., $\psi = 0$ at $z = -H$, the solution in equation 6.7 can be written in the form

$$\psi(x,z) = (A\cos mx + B\sin mx)(e^{mz} - e^{-m(z+2H)}), \tag{6.8}$$

where A and B are arbitrary constants. Now consider planar or tangential anchoring of the director on the surface of the thin sheet at the top of the nematic medium. The height profile of this top surface is given by $z = h(x)$, where we have assumed translational invariance along the y axis. The unit normal and tangent vectors to the curve $z = h(x)$ at the point (x,h) are given by $\hat{N} = \frac{1}{\sqrt{1+h'^2}}(-h',0,1)$ and $\hat{t} = \frac{1}{\sqrt{1+h'^2}}(1,0,h')$ respectively, where the prime denotes the derivative with respect to x, i.e., $h' \equiv \frac{dh}{dx}$. Then, for the planar boundary condition of the director $\hat{n}$ on the thin sheet, we have $\psi = tan^{-1}h'$ at $z = h$. Using this boundary condition in equation 6.8, the final solution for the angle ψ can be written as

$$\psi(x,z) = \frac{e^{mz} - e^{-m(z+2H)}}{e^{mh} - e^{-m(h+2H)}}\tan^{-1}h' \tag{6.9}$$

The solution in equation 6.9 corresponds to the planar anchoring condition at both the boundary surfaces (i.e., planar anchoring condition). Similarly, for planar anchoring at the bottom surface and homeotropic anchoring at the top surface (i.e., hybrid anchoring condition), the solution becomes

$$\psi(x,z) = \frac{e^{mz} - e^{-m(z+2H)}}{e^{mh} - e^{-m(h+2H)}}\left(\frac{\pi}{2} + \tan^{-1}h'\right) \tag{6.10}$$

Therefore, the solution of ψ varies with the anchoring conditions at the upper and bottom surfaces. For both these boundary conditions, the solution of ψ can also be written in a single expression as

$$\psi(x,z) = \frac{e^{mz} - e^{-m(z+2H)}}{e^{mh} - e^{-m(h+2H)}}\left(\psi_1 + \tan^{-1} h'\right) \tag{6.11}$$

where the ψ_1 takes values 0 and $\pi/2$ for the planar and hybrid boundary conditions, respectively. To get an effective free energy that depends only on the height profile h, we integrate the nematic elastic distortion free energy from the bottom surface to the top of the nematic medium using the solution of ψ satisfying appropriate boundary conditions. Integrating the equation 6.5 over z, the nematic elastic distortion free energy per unit length is

$$F_{LC}[\psi] = \frac{K}{2}\int dx \int_{-H}^{h} \left[(\partial_x\psi)^2 + (\partial_z\psi)^2\right] dz \tag{6.12}$$

Using the solution of ψ in equation 6.11, one can find

$$\begin{aligned}
\partial_x\psi &= \frac{e^{mz} - e^{-m(z+2H)}}{e^{mh} - e^{-m(h+2H)}}\left[\frac{h''}{1+h'^2} - mh'\frac{\exp^{mh} + \exp^{-m(h+2H)}}{e^{mh} - e^{-m(h+2H)}}(\psi_1 + \tan^{-1} h')\right] \\
\partial_z\psi &= m\frac{e^{mz} + e^{-m(z+2H)}}{e^{mh} - e^{-m(h+2H)}}(\psi_1 + \tan^{-1} h').
\end{aligned}$$

By plugging the expressions for $\partial_x\psi$ and $\partial_z\psi$ in equation 6.12 and integrating over z, the final free energy functional in terms of height profile h can be written as

$$F_{LC}[h] = \int dx f_{LC}(h, h', h'') \tag{6.13}$$

where

$$
\begin{aligned}
f_{LC}(h,h',h'') = \frac{K}{2\big(e^{mh}-e^{-m(h+2H)}\big)^2} \times \Bigg[\Big(&\frac{e^{2mh}-e^{-2m(h+2H)}}{2m} - 2(h+H)e^{-2mH}\Big)\Big\{ \\
&\frac{h''}{1+h'^2} - mh'\frac{e^{mh}+e^{-m(h+2H)}}{e^{mh}-e^{-m(h+2H)}}(\psi_1+\tan^{-1}h')\Big\}^2 + m^2(\psi_1+\tan^{-1}h')^2\Big(\\
&\frac{e^{2mh}-e^{-2m(h+2H)}}{2m} + 2(h+H)e^{-2mH}\Big)\Bigg] \qquad (6.14)
\end{aligned}
$$

For large depth $H \to \infty$, the free energy density $f_{LC}(h,h',h'')$ in equation 6.14 becomes

$$
f_{LC} = \frac{K}{4m}\left[\left(\frac{h''}{1+h'^2}\right)^2 - 2m\frac{h'h''}{1+h'^2}(\psi_1+\tan^{-1}h') + m^2(1+h'^2)(\psi_1+\tan^{-1}h')^2\right]. \qquad (6.15)
$$

Expressing the derivatives h' and h'' in terms of the derivatives with respect to the arc length s, one can write

$$
\begin{aligned}
h' &= \frac{dh}{dx} = \frac{ds}{dx}\frac{dh}{ds} = \frac{1}{\sqrt{1-\dot{h}^2}}\frac{dh}{ds} = \frac{\dot{h}}{\sqrt{1-\dot{h}^2}} \\
h'' &= \frac{\ddot{h}}{(1-\dot{h}^2)^2}
\end{aligned}
$$

where $\dot{h}$ denotes the derivative with respect to s i.e. $\dot{h} \equiv \frac{dh}{ds}$. Substituting h' and h'' in equation 6.13, the free energy functional per unit length can be written as

$$
\begin{aligned}
F_{LC} = \frac{K}{4m}\int_{-\frac{L}{2}}^{\frac{L}{2}} ds\Bigg[&\frac{\ddot{h}^2}{(1-\dot{h}^2)^{\frac{3}{2}}} - 2m\frac{\ddot{h}\dot{h}}{1-\dot{h}^2}(\psi_1+\tan^{-1}\frac{\dot{h}}{\sqrt{1-\dot{h}^2}}) \\
&+ \frac{m^2}{\sqrt{1-\dot{h}^2}}\left(\psi_1+\tan^{-1}\frac{\dot{h}}{\sqrt{1-\dot{h}^2}}\right)^2\Bigg]. \qquad (6.16)
\end{aligned}
$$

6.2.4 Total Energy

The total free energy of the system per unit length is the sum of all three energies $F = F_B + F_g + F_{LC}$. The model can give rise to multiple length scales of the system depending on the competition between any two energies. The elastic free energy F_{LC} is found to be low in our system compared to F_B and F_g. Therefore, we chose the length $\lambda_0 = (\frac{B}{\rho g})^{\frac{1}{4}}$ as the length scale in our model, which can be obtained by comparing F_B and F_g. Rescaling the free energy in terms of the bending modulus B and measuring all the lengths in the unit of λ_0, the dimensionless form of the total free energy functional can be written as

$$\begin{aligned}\tilde{F} = \int_{-\frac{L}{2}}^{\frac{L}{2}} ds \Bigg[& \frac{1}{2}\frac{\ddot{h}^2}{1-\dot{h}^2} + \frac{1}{2}h^2\sqrt{1-\dot{h}^2} + \frac{\tilde{K}}{4\tilde{m}}\Bigg\{ \frac{\ddot{h}^2}{(1-\dot{h}^2)^{\frac{3}{2}}} \\ & - 2\tilde{m}\frac{\ddot{h}\dot{h}}{1-\dot{h}^2}(\psi_1 + \tan^{-1}\frac{\dot{h}}{\sqrt{1-\dot{h}^2}}) + \frac{\tilde{m}^2}{\sqrt{1-\dot{h}^2}}\left(\psi_1 + \tan^{-1}\frac{\dot{h}}{\sqrt{1-\dot{h}^2}}\right)^2 \Bigg\}\Bigg] ,\end{aligned} \tag{6.17}$$

and the dimensionless form of the incompressibility constraint of the thin sheet becomes

$$\Delta = \int_{-\frac{L}{2}}^{\frac{L}{2}} ds(1 - \sqrt{1-\dot{h}^2}) , \tag{6.18}$$

where $\tilde{K} = \frac{K\lambda_0}{B}$ and $\tilde{m} = m\lambda_0$.

6.3 Energy minimization

The optimal shape $h(s)$ of the thin sheet can be determined by minimizing the dimensionless energy with the incompressibility constraint of the thin sheet given by the equations 6.17 and 6.18, respectively. The energy expression contains highly nonlinear terms, and finding the analytical solution of optimal $h(s)$ is a formidable task. Hence, we minimize this energy by assuming the ansatz $h(s) = A\cos qs$. A similar procedure has also been employed in earlier studies dealing with a thin sheet floating on an isotropic fluid substrate [19, 23]. In our model, the bending energy of the thin sheet is the most dominant term. Hence, the modulation wavelength of the thin sheet determines the periodicity in the director distortion in the underlying nematic medium. Therefore, we assume $\tilde{m} = q$ in our model. Such an assumption has also been used in earlier studies investigating grooved surface-induced alignment of the nematic liquid crystals [24, 26–29]. The total energy being an extensive quantity, we define $\tilde{F} = L\varepsilon(\delta)$ following the earlier study [23] where $\varepsilon(\delta)$ is the intensive quantity and $\delta = \Delta/L$. Retaining the terms up to the fourth order in the amplitude A, the constraint equation 6.18 can be written as

$$\delta = \frac{A^2 q^2}{4} + \frac{3A^4 q^4}{64}. \tag{6.19}$$

The energy expression for the planar anchoring condition can be written as

$$\varepsilon = \frac{A^2}{4}(q^4 + \tilde{K}q^3 + 1) + \frac{A^4 q^2}{32}(2q^4 + 4\tilde{K}q^3 - 1), \tag{6.20}$$

whereas for the hybrid anchoring condition, it can be expressed as

$$\varepsilon = \frac{\pi^2 q\tilde{K}}{16} + \frac{A^2}{4}\big[q^4 + \tilde{K}q^3(1 + \frac{\pi^2}{16}) + 1\big] + \frac{A^4 q^2}{32}\big[2q^4 + 4\tilde{K}q^3(4 + \frac{9\pi^2}{32}) - 1\big]. \tag{6.21}$$

Solving the quadratic equation 6.19 for A^2, one can write

$$A^2 = \frac{8\sqrt{1+3\delta} - 8}{3q^2} \cong \frac{8(1 + \frac{3\delta}{2} - \frac{9\delta^2}{8}) - 8}{3q^2} = \frac{4\delta - 3\delta^2}{q^2}. \tag{6.22}$$

Substituting the expression for A^2 from the equation 6.22 in the free energy expressions 6.20 and 6.21, and retaining the terms up to the second order in δ, we obtain the final energy expressions. The free energy expression for the planar anchoring condition can be written as

$$\varepsilon = (q^2 + \tilde{K}q + \frac{1}{q^2})\delta + (q^2 + 5\tilde{K}q - \frac{5}{q^2})\frac{\delta^2}{4}. \tag{6.23}$$

The free energy expression for the hybrid anchoring condition is

$$\varepsilon = \frac{\pi^2 q\tilde{K}}{16} + \big[q^2 + \tilde{K}(1 + \frac{\pi^2}{16})q + \frac{1}{q^2}\big]\delta + \big[q^2 + \tilde{K}q(5 + \frac{3\pi^2}{8}) - \frac{5}{q^2}\big]\frac{\delta^2}{4}. \tag{6.24}$$

For the isotropic fluid medium, $\tilde{K}$ is zero, and the anchoring conditions lose physical meaning. Hence, the energy density ε for the isotropic liquid medium can obtained by putting $\tilde{K} = 0$ in both the expressions 6.23 and 6.24, which agrees with the earlier theoretical study [23]. We numerically minimize these energy expressions with respect to q to obtain the optimal wavelength of the wrinkling patterns.

6.4 Results and Discussions

The variation of the energy density ε as a function of the wave vector q is shown in figure 6.3 for both planar and hybrid anchoring conditions. The energy decreases sharply for low values of q, showing an asymmetric minimum at $q = q_c$ and again increases for higher values of q. The q_c determines the wavelength of the wrinkling instability. It is found that the energy densities given by these equations 6.23 and 6.24 do not vary significantly on neglecting the quadratic term in δ in our model. It can be seen from figure 6.3 that the two curves of the energy, including linear and quadratic terms in δ, only differ slightly for higher values of q. Henceforth, for simplicity, we neglect the quadratic term in δ in the energy expressions.

For the isotropic medium, one can easily find that the wrinkling pattern has minimum energy for $q_c = 1$, which is independent of compression δ. But, the amplitude depends on δ as $A \sim 2\sqrt{\delta}/q_c$. The wavelength of the wrinkling pattern can be ob-

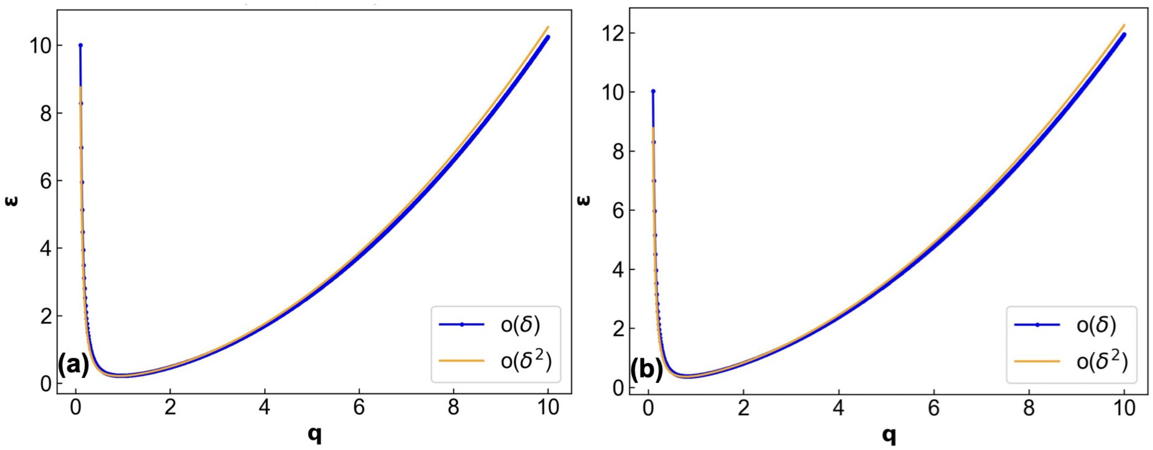

Figure 6.3: The variation of the energy density ε as a function of the wave vector q for (a) the planar anchoring condition and (b) hybrid anchoring condition where $\tilde{K} = 0.25$ and $\delta = 0.1$.

tained from q_c as $\lambda = 2\pi\left(\frac{B}{\rho g}\right)^{\frac{1}{4}}$ which has been experimentally validated in earlier study [12].

For the planar anchoring condition of the nematic medium, the variation of q_c with $\tilde{K}$ is shown in figure 6.4. The q_c decreases non-linearly with the increasing values of $\tilde{K}$. This can be understood from the fact that the large wavelength undulation of the thin sheet reduces the elastic distortion energy of the nematic medium. It is interesting to note that q_c in the nematic medium is always less than one which corresponds to the isotropic medium. In other words, the wavelength of the wrinkling pattern corresponding to the planar anchoring condition of the nematic medium is higher compared to that of the isotropic liquid medium. It should be noted that q_c for the planar anchoring condition does not depend on δ up to linear order in δ in equation 6.23. This is similar to that of the isotropic medium.

For the hybrid anchoring condition of the nematic director at the bounding surfaces, the model predicts different properties compared to the planar anchoring condition. In this hybrid anchoring condition, q_c depends on both $\tilde{K}$ and δ, unlike both the cases of isotropic medium and nematic medium with the planar alignment. This difference can be understood from the minimization of the energy density in equa-

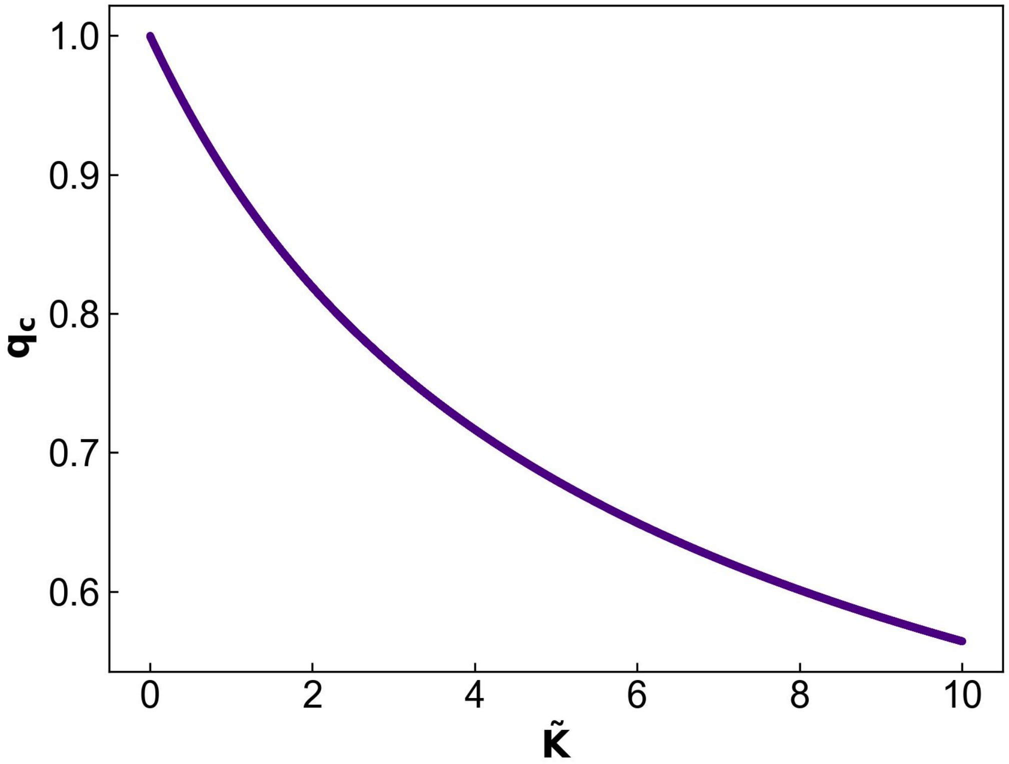

Figure 6.4: The variation of the optimal wave vector q_c as a function of the effective elastic constant $\tilde{K}$ for the planar anchoring conditions of the nematic director field.

tion 6.24 with respect to the wave vector q. Figure 6.5(a) represents the variation of q_c with $\tilde{K}$ for different fixed values of δ. The q_c decreases non-linearly with the increasing values of $\tilde{K}$, which can be explained by the lower energy cost associated with the distortion of the nematic director over the large wavelength modulation. Figure 6.5(b) represents the variation of q_c as a function of δ for different fixed values of $\tilde{K}$. For a fixed value of $\tilde{K}$, q_c increases with the increasing values of δ. Large compression can give rise to the high amplitude undulation of the thin shit, which is favored by both the nematic elastic energy and bending energy, but not favored by the gravitational energy contribution. The competing effect of these energies determines q_c as a function of δ. Similar to the planar anchoring condition, q_c is always less than one for the hybrid anchoring condition of the nematic director. Thus, the wavelength

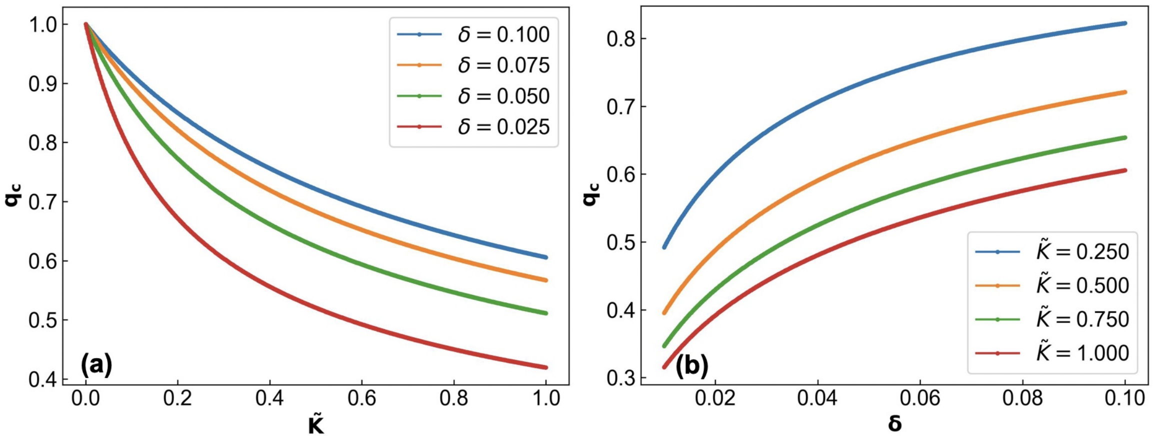

Figure 6.5: Representing the results for the hybrid anchoring condition of the nematic director field. (a) The variation of the optimal wave vector q_c as a function of the effective elastic constant $\tilde{K}$ for different values of δ. (b) The variation of q_c as a function of δ for different values of $\tilde{K}$.

of the undulation in the case of a nematic medium is always higher than that of the isotropic medium.

Therefore, the wavelength of the wrinkling patterns strongly depends on the elastic distortion energy of the nematic director. It is well known that the electric field couples with the nematic director and tends to align the director field. Hence, the application of the electric field can tune the wavelength of the wrinkling patterns. Moreover, the nematic elastic constant $(\tilde{K})$ depends on the scalar orientational order parameter S, which varies with the temperature. Therefore, the temperature can also tune the wavelength of the wrinkling patterns.

The above theoretical findings suggest that nematic elastic deformations can have important effects on wrinkling instability. Experimental studies of wrinkling instability using polystyrene thin sheets have been reported earlier for the isotropic fluid substrate. The thickness of the polystyrene sheet used in such experiments was about $50 - 100\ nm$. We now explore the conditions under which the nematic distortion can have significant effects on wrinkling instability in these types of experimental systems. It can be seen from figure 6.5 that the nematic effect can be easily observed for values of $\tilde{K}$ greater than about 0.2 where the effective elastic constant $\tilde{K} = \frac{K\lambda_0}{B}$. The density and curvature elastic constant of a nematic medium are $\rho \sim 1000\ Kg/m^3$ and $K \sim 10^{-11}\ N$, respectively. The Young modulus of polystyrene material lies in the range $E \sim 1.9 - 2.9\ GPa$, and the bending modulus of a thin sheet of thickness t is given by $B \sim Et^3$. The length scale $\lambda_0 = (\frac{B}{\rho g})^{\frac{1}{4}}$ where $g \sim 10\ m/s^{-2}$ is the acceleration due to gravity. Using these values of parameters, we find that the thickness of the polystyrene sheet should be lower than 20 nm to observe the significant effects of the nematic medium on the wrinkling pattern. It should be noted that the thickness of the polystyrene sheet should be much lower than that used in previous experiments for isotropic substrates. However, a system with the lower Young modulus of the thin sheet or a nematic substrate with a higher curvature elastic constant can also be a good model system to validate our theoretical predictions. It is known that the nematic elastic constant K shows diverging behavior on approaching the nematic-smectic A transition temperature. Therefore, the experimental studies near the nematic-smectic A transition temperature can be performed to validate our theoretical findings.

6.5 Summary

We have theoretically studied the wrinkling instability in a unidirectionally compressed thin sheet floating on a nematic liquid crystal medium. The variation of the wave vector of the wrinkling pattern as a function of various model parameters has been studied. The periodicity of the pattern is always found to be larger in the case of nematic substrate compared to its isotropic state. This arises due to the excess energy cost associated with the distortion of the nematic director during wrinkling. It is found that the periodicity of the pattern sensitively depends on the curvature elastic constant and the surface anchoring conditions of the nematic. Interestingly, the model also predicts that the wrinkling periodicity depends on the amount of compression for the hybrid anchoring condition of the nematic director on the bounding surfaces.

Bibliography

[1] J. Genzer and J. Groenewold, Soft Matter **2**, 310 (2006), URL `http://dx.doi.org/10.1039/B516741H`.

[2] E. Cerda and L. Mahadevan, Phys. Rev. Lett. **90**, 074302 (2003), URL `https://link.aps.org/doi/10.1103/PhysRevLett.90.074302`.

[3] B. Li, Y.-P. Cao, X.-Q. Feng, and H. Gao, Soft Matter **8**, 5728 (2012), URL `http://dx.doi.org/10.1039/C2SM00011C`.

[4] Y. Tan, B. Hu, J. Song, Z. Chu, and W. Wu, Nano-Micro Letters **12**, 101 (2020), URL `https://doi.org/10.1007/s40820-020-00436-y`.

[5] C. M. Stafford, C. Harrison, K. L. Beers, A. Karim, E. J. Amis, M. R. VanLandingham, H.-C. Kim, W. Volksen, R. D. Miller, and E. E. Simonyi, Nature Materials **3**, 545 (2004), URL `https://doi.org/10.1038/nmat1175`.

[6] D.-Y. Khang, H. Jiang, Y. Huang, and J. A. Rogers, Science **311**, 208 (2006), `https://www.science.org/doi/pdf/10.1126/science.1121401`, URL `https://www.science.org/doi/abs/10.1126/science.1121401`.

[7] C. M. Stafford, B. D. Vogt, C. Harrison, D. Julthongpiput, and R. Huang, Macromolecules **39**, 5095 (2006), `https://doi.org/10.1021/ma060790i`, URL `https://doi.org/10.1021/ma060790i`.

[8] J. Y. Chung, A. J. Nolte, and C. M. Stafford, Advanced Materials **23**, 349 (2011), `https://onlinelibrary.wiley.com/doi/pdf/10.`

1002/adma.201001759, URL `https://onlinelibrary.wiley.com/doi/abs/10.1002/adma.201001759`.

[9] W. Li, J. Liu, L. Chen, W. Wei, K. Qian, Y. Liu, and J. Leng, Small **18**, 2105958 (2022), `https://onlinelibrary.wiley.com/doi/pdf/10.1002/smll.202105958`, URL `https://onlinelibrary.wiley.com/doi/abs/10.1002/smll.202105958`.

[10] T. Ohzono and H. Monobe, Journal of Colloid and Interface Science **368**, 1 (2012), ISSN 0021-9797, URL `https://www.sciencedirect.com/science/article/pii/S0021979711014524`.

[11] P. Rofouie, D. Pasini, and A. D. Rey, The Journal of Chemical Physics **143**, 114701 (2015), ISSN 0021-9606, `https://pubs.aip.org/aip/jcp/article-pdf/doi/10.1063/1.4929337/15504354/114701_1_online.pdf`, URL `https://doi.org/10.1063/1.4929337`.

[12] L. Pocivavsek, R. Dellsy, A. Kern, S. Johnson, B. Lin, K. Y. C. Lee, and E. Cerda, Science **320**, 912 (2008), `https://www.science.org/doi/pdf/10.1126/science.1154069`, URL `https://www.science.org/doi/abs/10.1126/science.1154069`.

[13] J. Huang, M. Juszkiewicz, W. H. de Jeu, E. Cerda, T. Emrick, N. Menon, and T. P. Russell, Science **317**, 650 (2007), `https://www.science.org/doi/pdf/10.1126/science.1144616`, URL `https://www.science.org/doi/abs/10.1126/science.1144616`.

[14] F. Brau, H. Vandeparre, A. Sabbah, C. Poulard, A. Boudaoud, and P. Damman, Nature Physics **7**, 56 (2011), URL `https://doi.org/10.1038/nphys1806`.

[15] J. Huang, B. Davidovitch, C. D. Santangelo, T. P. Russell, and N. Menon,

Phys. Rev. Lett. **105**, 038302 (2010), URL `https://link.aps.org/doi/10.1103/PhysRevLett.105.038302`.

[16] G. Boedec and J. Deschamps, International Journal of Solids and Structures **233**, 111214 (2021), ISSN 0020-7683, URL `https://www.sciencedirect.com/science/article/pii/S0020768321003048`.

[17] D. Vella, P. Aussillous, and L. Mahadevan, Europhysics Letters **68**, 212 (2004), URL `https://dx.doi.org/10.1209/epl/i2004-10202-x`.

[18] E. Cerda, K. Ravi-Chandar, and L. Mahadevan, Nature **419**, 579 (2002), URL `https://doi.org/10.1038/419579b`.

[19] Q. Zhang and T. A. Witten, Phys. Rev. E **76**, 041608 (2007), URL `https://link.aps.org/doi/10.1103/PhysRevE.76.041608`.

[20] F. Brau, P. Damman, H. Diamant, and T. A. Witten, Soft Matter **9**, 8177 (2013), URL `http://dx.doi.org/10.1039/C3SM50655J`.

[21] Y. Ebata, A. B. Croll, and A. J. Crosby, Soft Matter **8**, 9086 (2012), URL `http://dx.doi.org/10.1039/C2SM25859E`.

[22] O. Oshri, F. Brau, and H. Diamant, Phys. Rev. E **91**, 052408 (2015), URL `https://link.aps.org/doi/10.1103/PhysRevE.91.052408`.

[23] H. Diamant and T. A. Witten, arXiv:1009.2487 (2018), `https://arxiv.org/pdf/1009.2487.pdf`, URL `https://arxiv.org/abs/1009.2487`.

[24] P. G. de Gennes and J. Prost, *The Physics of Liquid Crystals* (Clarendon Press, Oxford, 1995).

[25] C. Extrand, Journal of Colloid and Interface Science **450**, 135 (2015), ISSN 0021-9797, URL `https://www.sciencedirect.com/science/article/pii/S0021979715002581`.

[26] D. W. Berreman, Phys. Rev. Lett. **28**, 1683 (1972), URL `https://link.aps.org/doi/10.1103/PhysRevLett.28.1683`.

[27] S. Faetti, Phys. Rev. A **36**, 408 (1987), URL `https://link.aps.org/doi/10.1103/PhysRevA.36.408`.

[28] J.-i. Fukuda, M. Yoneya, and H. Yokoyama, Phys. Rev. Lett. **98**, 187803 (2007), URL `https://link.aps.org/doi/10.1103/PhysRevLett.98.187803`.

[29] G. Barbero, A. S. Gliozzi, M. Scalerandi, and L. R. Evangelista, Phys. Rev. E **77**, 051703 (2008), URL `https://link.aps.org/doi/10.1103/PhysRevE.77.051703`.

Chapter 7

Conclusions and future research directions

This thesis includes theoretical and computational studies toward the understanding of self-assembled structures and their properties exhibited by liquid crystalline systems. In this chapter, we summarize the main findings of this thesis and discuss the directions for future investigations.

In **Chapter two**, we have studied the effects of excluded volume interaction on the spontaneous chiral symmetry breaking observed in the tilted smectic phases of the achiral bent-core molecules. We have numerically computed excluded volume between two rigid bent-core molecules in a layer using two types of model structures of the molecules, namely the hard-spherocylinder model and the bead model. The excluded volume interactions for both models of the bent-core molecules account for the chiral symmetry breaking in their tilted smectic phase. It is found that the excluded volume interaction can give rise to C_1, C_2, and C_S point symmetries of a tilted polar smectic layer depending on the molecular model. Based on the excluded volume results, we have also constructed a coupled XY-Ising model to describe the phase behavior of a layer consisting of bent-core molecules. The Monte Carlo simulations performed

on this system account for the experimentally observed chiral symmetry breaking induced by both the temperature as well as the electric field.
At present, the simulations for our coupled XY-Ising model were performed on a single layer of the smectic phase and hence, deals only with intralayer interactions among the particles. In the actual three-dimensional smectic phase, the interlayer interactions also play significant roles in the phase behavior and can lead to rich varieties of self-assembled structures. As future research, it is worthwhile to perform the Monte-Carlo simulations using our coupled XY-Ising model for a three-dimensional smectic phase.

In **Chapter three**, we have developed a Landau theory accounting for the SmA → de Vries SmA → SmC phase sequence observed in our sample consisting of bent-core hockey stick-shaped molecules. The theoretical model describes a weakly first-order phase transition from the SmA phase to the de Vries SmA phase and a second-order phase transition from the de Vries SmA phase to the SmC phase, as observed in our experimental studies. The temperature variation of the layer compression obtained from the theoretical model is compared with the experimental data and agrees reasonably well with the experimental observations. We have also constructed a phase diagram showing the stability regions of these phases on a parameter plane of the model.
The theory presented in this thesis does not deal with any terms involving the polar or chiral order of the system. However, the bent-core molecules are known to exhibit polar as well as chiral order in some of their tilted smectic phases. Therefore, the extension of the theory to include the polar and chiral order parameters can be a future research project.

In **Chapter four**, we have described a coupled phase-field model comprised of a conserved and a nonconserved order parameter. The dynamics of the order parameters are governed by the time-dependent Ginzburg-Landau model C equations. We have performed the linear stability analysis of the equations to find the fastest-growing instability mode for various values of the model parameters. By employing the finite difference method, we have also computed the numerical solutions of the nonlinear differential equations of the model. The numerical solutions exhibit various patterns, such as continuous, ring-banded, and broken ring patterns, depending on the model parameters. In **Chapter five**, we have employed this model to account for the banded spherulitic growth observed in our experimental studies on a pure liquid crystalline compound. The variation of the experimentally observed band spacing as a function of supercooling agrees well with the theoretical predictions. It is found that the radius of the simulated banded spherulitic domain increases in a step-like fashion with time, giving rise to the rhythmic growth dynamics.

Our current model describes the rhythmic growth-assisted formation of banded spherulites. However, some other systems, especially polymers, are known to form banded spherulites without showing the rhythmic growth of the radius with time. The experimental evidence suggests that the banded spherulites for these systems are formed due to the coherent twisting of radially aligned fibrils. It would be interesting to incorporate the twisting of the fibrils in our model.

In **Chapter six**, we have constructed a theory describing the wrinkling instability of a thin elastic sheet floating atop a nematic medium and compressed unidirectionally. The minimization of the effective one-dimensional free energy of the system gives rise to the favored wrinkling wavelength of the sheet. The wrinkling wavelength strongly depends on the surface anchoring conditions of the nematic director and the elastic constant of the medium. It is also found that the wavelength is always found to be larger in the nematic phase of the substrate than that of its isotropic phase. The experimental verification of the theoretical predictions would be an interesting project for future research. It is well known that the applied electric field easily tunes the orientation of the nematic director. Therefore, the effect of the applied field on wrinkling can also be worthwhile theoretical as well as experimental projects for future research.